論文 / 著書情報
Article / Book Information

題目(和文)	
Title(English)	Effect of catalyst preparation method of silver and manganese oxides on titanium dioxide on the decomposition of benzene using non-thermal plasma catalysis
著者(和文)	PANGILINAN CDC
Author(English)	Christian David Cruz Pangilinan
出典(和文)	学位:博士（工学）, 学位授与機関:東京工業大学, 報告番号:甲第9983号, 授与年月日:2015年9月25日, 学位の種別:課程博士, 審査員:日野出　洋文,中崎　清彦,小松　隆之,関口　秀俊,森　伸介
Citation(English)	Degree:, Conferring organization: Tokyo Institute of Technology, Report number:甲第9983号, Conferred date:2015/9/25, Degree Type:Course doctor, Examiner:,,,,
学位種別(和文)	博士論文
Type(English)	Doctoral Thesis

Effect of catalyst preparation method of silver and manganese oxides on titanium dioxide on the decomposition of benzene using non-thermal plasma catalysis

A dissertation submitted to
TOKYO INSTITUTE OF TECHNOLOGY
for the degree of

DOCTOR OF ENGINEERING

by
CHRISTIAN DAVID C. PANGILINAN

Department of International Development Engineering
Graduate School of Science and Engineering

August 2015

Name: Christian David Cruz Pangilinan

Supervisor: Prof. Hirofumi Hinode

Department: International Development Engineering

Thesis title: Effect of catalyst preparation method of silver and manganese oxides on titanium dioxide on the decomposition of benzene using non-thermal plasma catalysis

Publications in peer-reviewed journals:

[1] Pangilinan, C.D.C., Kurniawan, W., Salim, C., Hinode, H. *Effect of Ag/TiO_2 catalyst preparation on gas-phase benzene decomposition using non-thermal plasma driven catalysis under oxygen plasma*. Reaction Kinetics, Mechanisms and Catalysis, 2015, DOI: 10.1007/s11144-015-0920-6

[2] Pangilinan, C.D.C., Kurniawan, W., Hinode, H. *Effect of MnOx/TiO_2 oxidation state on ozone concentration in a non-thermal plasma driven catalysis reactor*. Ozone: Science and Engineering (Submitted, under review)

Publications and presentations in international conferences:

[1] Effect of catalyst preparation method on the gas-phase benzene decomposition by non-thermal plasma driven catalysis under air plasma, 9th International Symposium on Non-Thermal/Thermal Plasma Pollution Control Technology & Sustainable Energy, 16-20 June 2014, Dalian, China

[2] Effect of catalyst preparation method on the decomposition of benzene using Ag/TiO_2 packed non-thermal plasma driven catalysis reactor, 6th AUN/SEED-Net Regional Conference on Chemical Engineering, 2-3 December 2013, Manila, Philippines

[3] Plasma driven catalysis with Ag/TiO_2 for the decomposition of gas-phase benzene, Asia-Oceanic Top University League on Engineering Students Conference, 24-25 November 2012

[4] Decomposition of gas-phase benzene using Ag/TiO_2 packed non-thermal plasma reactor, 19th Regional Symposium on Chemical Engineering, 7-8 November 2012, Bali, Indonesia

Table of Contents

List of Figures

List of Tables

Chapter 1

INTRODUCTION

1.1 Background

1.1.1 Volatile organic compounds

Raising environmental awareness and promoting environmental protection is an issue of growing concern as our world is becoming more and more polluted. Industrialization has led to the emission of various substances in our atmosphere that pose significant threat to both human and ecological life. Governments throughout the world are passing legislations in order to reduce and limit these emissions and protect the environment such as the Kyoto Protocol in 1997 and the Protocol of Gothenburg in 1999.

One major group of these pollutants are volatile organic compounds (VOCs) and are defined as easily gasified organic compounds because of their high volatility and they are easily released into the earth's atmosphere. Sources include both mobile and stationary sources such as industrial, commercial and agricultural processes. Most industries are major contributors of VOC emissions as these chemicals are included as raw materials in various chemical processes [1-5].

The major sources of VOC emissions are from organic solvents used in the oil and chemical industries, combustion sources, and motor vehicles. Minor sources include metal industries, food and drink manufacturing, waste disposal and plastic industries. The major use of solvents is in the formation of industrial coating materials such as paints, inks and adhesives. The evaporation of these solvents after their application is an essential aspect of their application and also the source of release of these pollutants to the environment. In countries where crude oil production is a major industry, the flaring and venting of gases from production facilities also is a major source of emission for VOCs. Emission from vehicles are primarily due to incomplete fuel combustion (exhaustive emission) and the losses of fuel prior to combustion (evaporative emission) [3].

Depending on their structure and concentration, VOCs together with nitrogen oxides and sulfur containing compounds react in a series of complex chemical reactions once released in the troposphere. These lead to the formation of secondary pollutants such as photochemical smog, secondary aerosol, suspended particulate matter, tropospheric ozone, acid deposition, and formation of organosulfuric compounds. Prolonged exposure to these chemicals are detrimental to human health and to the environment. Effects to human health range from causing odor nuisances to having mutagenic and carcinogenic effects [1-5].

1.1.2 Abatement techniques

Techniques for VOC abatement and its reduction can be achieved by four distinct approaches either by itself or in combination of (1) resource management, (2) product reformulation, (3) process modification and (4) end-of-pipe technologies. Resource management involves the improvement in the management and control of the processes to minimize emissions and wastage. Product reformulation involves the reduction or elimination in the use of organic solvents in the products such as coatings used in the process like in the use of high solid-low solvent ratio coatings, water-based coatings, radiation-cured coatings and powder coatings. Process modification involves reducing emissions from a process by improving or making modifications to the equipments used. And finally, end-of-pipe technologies which involves the treatment of emissions from processes by specialized technologies which either destroy or capture the emissions[3]. Industries should be fully aware of these approaches and utilize them in their processes. However, due to either lax emissions standards or poor implementation of emission standards, these are often overlooked.

In an attempt to minimize VOC emissions thus reducing the need for further treatment, process and equipment modification has been looked into. These pertain to the modification of the process equipment, raw material or the manufacturing process itself. These are usually the most efficient and effective means to reduce VOC emissions, however, there are cases wherein it is not possible to modify or change the process thus its applicability are limited.

With stringent control limits being established, most industries focus on treatment methods in order to reduce their emissions, specifically, for industries that has long since started its operations. Conventional methods for end-of-pipe technologies for VOCs can be classified into either recovery or destruction of the pollutant. Recovery technologies include absorption, adsorption, condensation and separation while destruction technologies involve thermal and catalytic oxidation, bio-filtration and using a reverse flow reactor. The problem with these technologies are that most of them are only cost-effective and suitable for mid-to-high VOC concentrations and destruction of the pollutant are usually energy intensive[5]. This is a major problem specifically for small to medium scale industries as they cannot afford to utilize such technologies.

For the purpose of this study, benzene was chosen as a representative VOC due to its wide use in many industrial processes primarily as a raw material, additive in gasoline and as a solvent. Industrial process, existence in gasoline, and its use in the production of ethylbenzene and styrene are major emission sources into waste streams and to the atmosphere. Exposure to benzene can cause drowsiness, dizziness, confusion and unconsciousness. Long-term exposure to can lead to adverse effects such as anemia, leukemia, blood diseases, and cancer[6]. Also, compared to other aromatic compounds, benzene has low reactivity. The reaction rate coefficients of aromatic compounds to OH radicals (in $\times 10^{-12}$ cm^3 $molecule^{-1}s^{-1}$) are in the following order: benzene (1.2) < toluene (5.96) <

ethylbenzene (7.1) < *o*-xylene (13.7) < *p*-xylene (14.3) < *m*-xylene (23.6) at 298 K[7]. Thus, if benzene could be decomposed, then it would be possible to decompose other aromatics as well.

1.1.3 Non-thermal plasma catalysis

Plasma is an ionized gas that can be generated by a number of sources like combustion, flames, electrically heated furnaces and electric discharges (corona, spark, glow, arc, microwave discharge, plasma jets and audio frequency plasma) and shocks (electrically, magnetically and chemically driven). Depending on the energy level, temperature and electronic density, plasma state is usually classified as either high temperature (thermal) plasma or cold (nonthermal or non-equilibrium) plasma[8-10].

Cold plasma or non-thermal plasma (NTP) has promising applications due to its low power requirement and its capacity to induce physical and chemical reactions within gases at low temperatures. The electrons in NTP can reach temperatures ranging from 10,000K to 100,000K while the gas temperature can remain as low as room temperature. It is the mixture of high temperature electrons, highly excited atoms and molecules, ions, radicals and photons that are generated in plasma that is of interest in VOC abatement [8-10].

Combination of non-thermal plasma with catalysis provides the advantages of high selectivity from catalysis and the fast ignition and response from plasma. It has been experimentally demonstrated that plasma catalysis could enhance the energy efficiency and improve CO_2 selectivity showing promising potential in air pollution control and abatement [4,8]. Detailed explanation on the theory and use of non-thermal plasma catalysis will be further discussed in the succeeding chapter.

1.2 Research objectives

Non-thermal plasma catalysis has been researched as an alternative technology and has shown great potential in the treatment of volatile organic compounds. Researches present the synergistic effect between non-thermal plasma and catalysis in the decomposition of VOCs, however, the interaction between plasma and catalysis is still uncertain. This study aims to investigate and evaluate the performance of differently prepared silver and manganese oxides on titanium dioxide on the decomposition of benzene in a non-thermal plasma catalysis system. Specifically, this study aims to:

- Investigate the effect of preparation methods on catalyst structural and chemical properties
- Observe the influence of reactor parameters on ozone and nitrogen oxides generation in a dielectric barrier discharge reactor

- Examine the catalytic activity of the prepared catalysts in limiting ozone and nitrogen oxides generation within the dielectric barrier discharge reactor
- Determine the effectiveness of the prepared catalysts in the decomposition of benzene in a non-thermal plasma driven catalysis system

1.3 Significance of the study

The main advantage of non-thermal plasma catalysis systems is their relatively low energy consumption and ability to treat pollutants at low operating temperatures. However, the interactive mechanisms between plasma and catalysis are still uncertain. The findings of this research could provide information on the influence of catalyst properties on the characteristics of plasma discharge and the active species that are generated; and evaluation of catalyst properties in comprehensively considering their capacities for catalytic activity and selectivity in a non-thermal plasma catalysis system.

1.4 Structure of the thesis

To realize the objectives of this research, this thesis is structured as presented and Fig. 1.1 and a brief summary of its contents is as follows:

- **Chapter 1** contains an overall introduction to the work, presenting the research background and the objectives of the study.
- **Chapter 2** presents the theoretical framework and review of related literature pertinent to this research in order to contextualize the discussions that follows in the succeeding experimental chapters. It contains an introduction to plasma, its applications, types and means of plasma generation and in the application of plasma in non-thermal plasma catalysis.
- **Chapter 3** discusses about the catalysts used in this study; its preparation methods and its characterization results.
- **Chapter 4** discusses the characterization of the dielectric barrier discharge reactor, in particular, the effect of reactor length, TiO_2 catalyst loading and reactor configuration on its discharge characteristics.
- **Chapter 5** discusses the effect of the prepared catalysts presented in chapter 3 in the effluent and discharge characteristics of the dielectric barrier discharge reactor, specifically looking into effluent concentrations of ozone and nitrogen oxides.
- Extending from the results obtained from chapters 3, 4, and 5, **Chapter 6** discusses the application of the prepared catalysts in the non-thermal plasma catalytic decomposition of

benzene considering over-all benzene conversion, carbon balance, CO_2 yield, and by-product formation.

- Finally, **Chapter 7** consolidates and summarizes the conclusions obtained from the investigations from chapters 3 to 6 and presents recommendations for future work in line with this research.

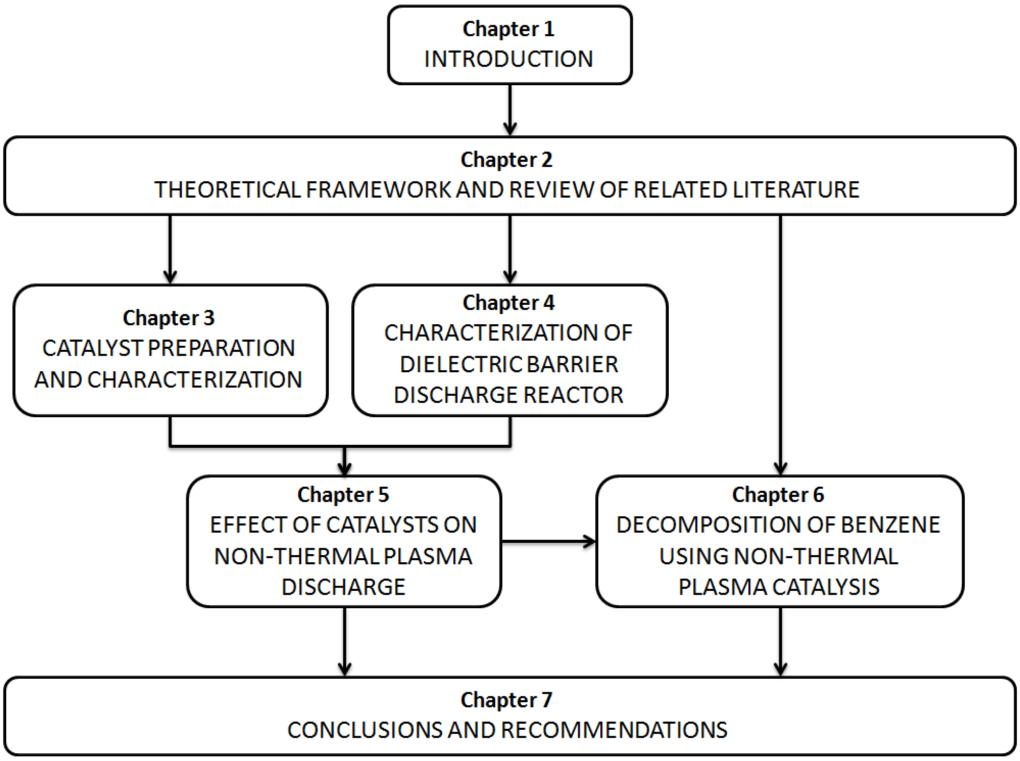

Figure 1.1. Concept map of the thesis structure

Chapter References

[1] **Chen, H.L., Lee, H.M., Chen, S.H., Chang, M.B., Yu, S.J., Li, S.N.** *Removal of volatile organic compounds by single-stage and two-stage plasma catalysis systems: A review of the performance enhancement mechanisms, current status, and suitable applications.* Environmental Science Technology 43 (2009) 2216-2227.

[2] **Dewulf, J., Van Durme, J., Leys, C., Van Langenhove, H.** *Combining non-thermal plasma with heterogeneous catalysis in was gas treatment: A review.* Applied Catalysis B: Environmental 78 (2007) 324-333.

[3] **Passant, N.R.** *Source inventories and control strategies for VOCs.* Retrieved from http://pubs.rsc.org, doi: 10.1039/9781847552310, published October 31, 2007.

[4] **Whitehead, J.C.** *Plasma catalysis: A solution for environmental problems*. Pure Applied Chemistry 82 (2010) 1329-1336.

[5] **Atkinson, R., Arey, J.** *Gas-phase tropospheric chemistry of biogenic volatile organic compounds: A review.* Atmospheric Environment 37 Supplement No. 2 (2003) S197-S219.

[6] TOXNET Hazardous Substances Data Bank. United States National Library of Medicine. Retrieved from http://toxnet.nlm.nih.gov, accessed October 23, 2014.

[7] **Atkinson, R., Baulch, D.L., Cox, R.A., Hampson Jr., R.F., Kerr, J.A., Rossi, M.J., Troe, J.** *Evaluated kinetic and photochemical data for atmospheric chemistry, organic species: Supplement VII.* Journal of Physical Chemistry Reference Data 26 (1997) 1329.

[8] **Vandernbroucke, A.M., Morent, R., De Geyter, N., Leys, C.** *Non-thermal plasmas for non-catalytic and catalytic VOC abatement.* Journal of Hazardous Materials 195 (2011) 30-45.

[9] **Chikorov, A., Gutsol, A., Fridman, A.** *Atmospheric pressure plasma of dielectric barrier discharges.* Pure Applied Chemistry 77 (2005) 487-495.

[10] **Petipas, G., Rollier, J.D., Darmon, A., Gonzales-Aguilar, J., Metkemeijer, R., Fulcheri, L.** *A comparative study of non-thermal plasma assisted reforming technologies.* International Journal of Hydrogen Energy 32 (2007) 2848-2867.

Chapter 2

THEORETICAL FRAMEWORK AND REVIEW OF RELATED LITERATURE

2.1 Non-thermal plasma catalysis

Nonthermal plasma (NTP), such as dielectric barrier discharge (DBD), glow discharge, corona discharge, surface discharge and packed-bed plasma reactor, features the option of generating of plasma at room temperature at atmospheric pressure with no warm-up time required. The glow discharge is a low-pressure discharge (less than 10 mbar) which usually operates between flat electrodes. Electrons and excited neutral atoms and molecules in a glow discharge are highly energetic thus producing the glow. However, this is not suitable for chemical synthesis due to its low pressure operation. The corona discharge is an inhomogeneous discharge and can be initiated at atmospheric pressure using inhomogeneous electrode geometries like a pointed wire electrode with a plate electrode. It is the small radius of curvature at the top of the wire electrode that results in a high electric field required for ionizing neutral molecules. A dielectric barrier discharge or silent discharge combines the large volume excitation of the glow discharge with the atmospheric pressure characteristics of the corona discharge. A dielectric layer covers at least one electrode and the entire electrode area will be effective for discharge reactions. Once the discharge starts, the charge accumulates on the dielectric to form an opposite electric field and interrupts the current flow in a few nanoseconds to generate microdischarges[1-3]. For this study, dielectric barrier discharge reactor was utilized.

2.2 Reactor configurations

Researchers have investigated a variety of NTP reactors for environmental purposes. The classification of these reactors are rather complex and depends on its characteristics such as the type of discharge (dielectric barrier, corona, surface, packed ferro-electric discharge, ...), type of power supply (AC, DC, pulse, microwave, RF, ...) and its other characteristics (electrode configuration, voltage level, polarity, gas composition, ...)[4]. Figure 2.1 shows some various NTP reactor configurations.

The same goes for a non-thermal plasma catalysis system. According to the location of the catalysts, a non-thermal plasma catalysis system can be configured either as single-stage or a two-stage configuration. Several different terminologies have been proposed to represent single-stage plasma catalysis system – plasma-driven catalysis, in-plasma catalysis reactor, combined plasma catalysis, in-plasma catalysis; as well as for a two-stage plasma catalysis system – plasma assisted catalysis, post-plasma catalysis reactor, plasma-enhanced catalysis and post-plasma catalysis[5]. For consistency, a single-stage configuration will be referred to as a plasma driven catalysis (PDC) system while a two-stage configuration will be referred to as a plasma assisted catalysis (PAC) system. Figure 2.2 presents the different combinations for plasma catalysis systems. In PDC, the catalysts are directly placed in the plasma discharge region, and in PAC, the catalysts are located downstream the plasma region. The catalysts can be introduced in the form of pellets, powder, foam, honeycomb monolith, coating, or the electrodes itself.

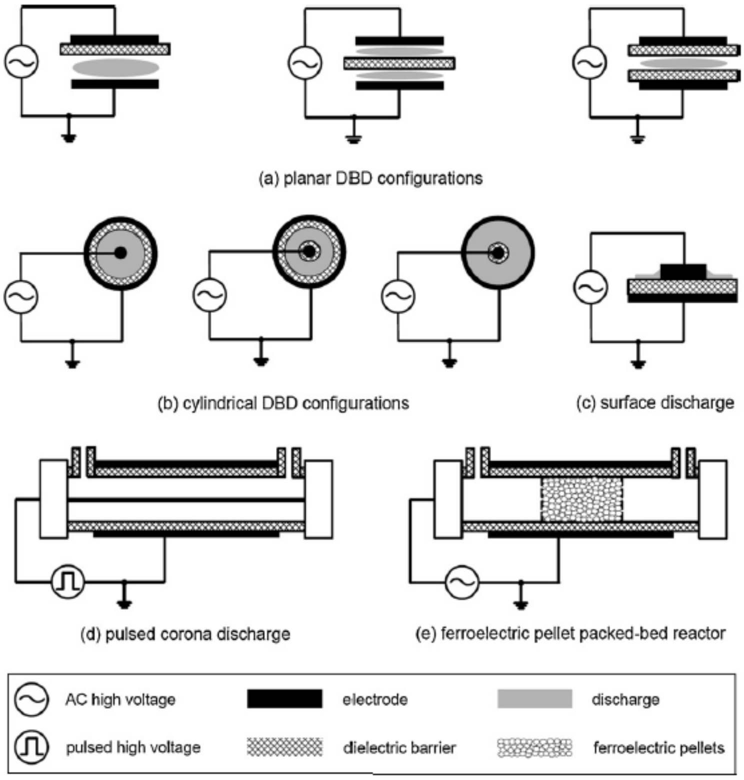

Figure 2.1. NTP reactor configurations[4]

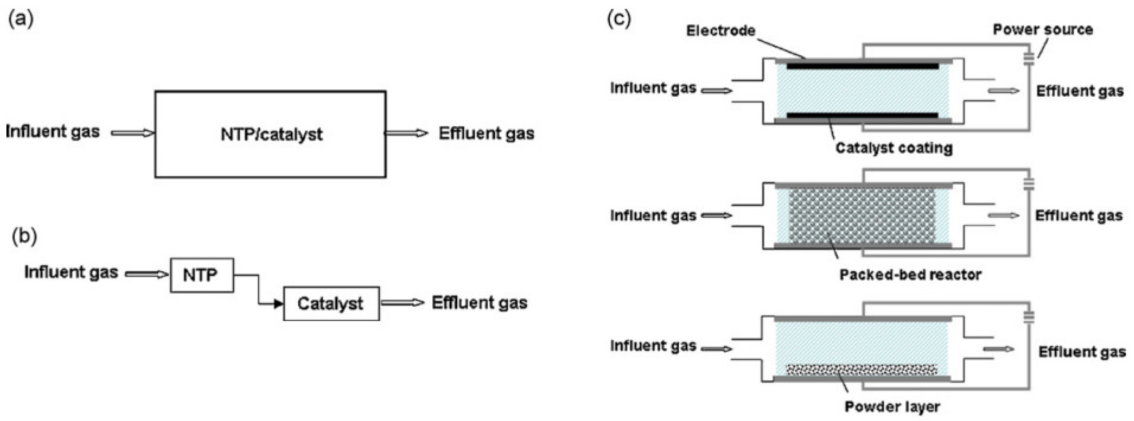

Figure 2.2. Non-thermal plasma catalysis reactor configurations (a) PDC, (b) PAC, (c) catalyst insertion method[5]

2.3 Mechanisms and performance of dielectric barrier discharge

A DBD consists of two electrodes with a dielectric in between. When the applied voltage reaches the breakdown value, microdischarges and streamers occur. The term "microdischarge" refers to a bright, thin plasma filament that is observed in DBDs. Microdischarges are based on the initial avalanche-to-streamer transition followed by streamer formation. This process takes about 10 ns in a typical DBD which only accelerates the electrons (Fig. 2.3) and does not raise the bulk gas temperature. Electron avalanche is a process in which free electrons are accelerated by an electric field, ionizing atoms by collision which further accelerates other electrons in a successive cycle. Electrons travel from the cathode to the electrode which then builds up and get absorbed followed by a cathode directed streamer. This process is then repeated in successive cycles [2].

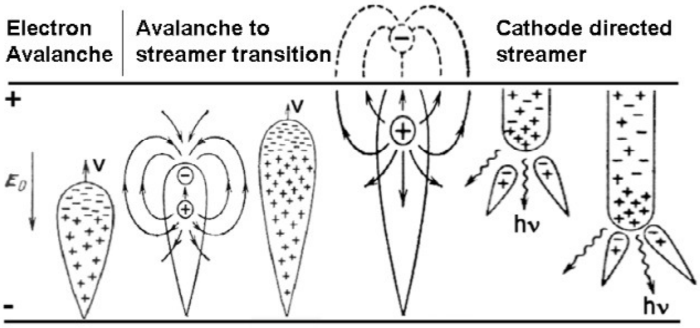

Figure 2.3. Mechanism of an electron avalanche[2]

Ozone generation efficiency is often used as a good indicator in DBD reactor performance. Ozone is formed due to the reaction of excited molecules in the plasma with oxygen gas. Generally, the higher the oxygen output at a specific energy input would yield a better performing DBD reactor. However, the mechanisms of ozone formation involve more than 50 chemical reactions and at least 10 species[6]. In addition to the chemistry involved, physical parameters such as gas composition, temperature, pressure, gas residence time, applied voltage, applied frequency, deposited power, dielectric material and reactor geometry all affect ozone synthesis. These parameters can be subsequently grouped into three categories namely reactor design, electrical and gas parameters.

M. B. Chang (1997)[7] studied the effect of increasing applied voltage, residence time and type of gas stream (oxygen and air) used on the synthesis of ozone using a DBD reactor. Their results showed that ozone concentration increased with increasing applied voltage and residence time regardless of the gas stream used. However, when dry air is used, less ozone was produced as compared to using pure oxygen gas stream. This was attributed to the competing reactions of the plasma with both oxygen to produce ozone and with nitrogen gas producing NOx.

V. I. Gibalov (2006)[8] studied the different types of barrier discharge arrangements and its design for ozone generation. Results showed that the efficiency of ozone synthesis and ozone saturation level depend on the features of the barrier discharge specifically on its design. Experiments showed that the lower value for the discharge gap, the gap between the dielectric and the electrode, the higher the amount of ozone is produced. The same also goes for the thickness of the dielectric. Plasma was produced as soon as the discharge breakdown value was reached and this value was dependent on the thickness of the medium being broken down. In the case of a dielectric barrier discharge configuration, this relates to thickness of the dielectric and the gap between the electrodes.

2.4 Mechanisms involved in non-thermal plasma catalysis

In non-thermal plasma catalysis, more so in a plasma driven catalysis system, the mechanisms are rather complex because plasma and catalysis acts simultaneously and interact with each other. Van Durme, et al. (2007)[5], presented a comprehensive flow diagram of the different mechanisms involved (Fig. 2.4).

Gaseous pollutant removal can be made possible with plasma, single-stage and two-stage plasma catalysis configuration. From the plasma source, generation of accelerated energetic electrons are due to bulk gas molecule collisions present. Excitation of gas molecules can generate photons for photo-activation of catalyst, dissociation and ionization to generate both short-lived (i.g. atomic oxygen, superoxide species, hydroxyl radicals, …) and long-lived (e.g. ozone, hydrogen peroxide, NOx, …) reactive plasma species and vibration can initiate thermal activation of the catalyst.

In a single-stage plasma catalysis configuration, the introduction of catalysts in the discharge region may affect the type of discharge and may induce a shift in the distribution of the accelerated electrons. Simultaneously, effect on plasma by the catalysts and effect on catalysis by the plasma are present which makes it difficult to identify a specific mechanism for the reaction and decomposition of target compounds.

In a two-stage plasma catalysis configuration, only the long-lived species are involved in the reaction and decomposition of the pollutant. A two-stage configuration can be done pre- and post-plasma but since the long-lived species are necessary to activate the catalyst, a two-stage configuration can be synonymously taken as post-plasma configuration when plasma catalysis is concerned.

Since the plasma discharge region and the catalyst bed are separated, only the long-lived plasma species reach the catalyst. The short-lived species would have vanished due to their high reactivity and short-life. The main role of plasma in a two-stage configuration is changing the gas composition fed into the catalyst reactor. Plasma could enrich the gas stream with chemically reactive species, pre-convert the pollutants into easier treatable substances for catalysis to oxidize/reduce the pollutant.

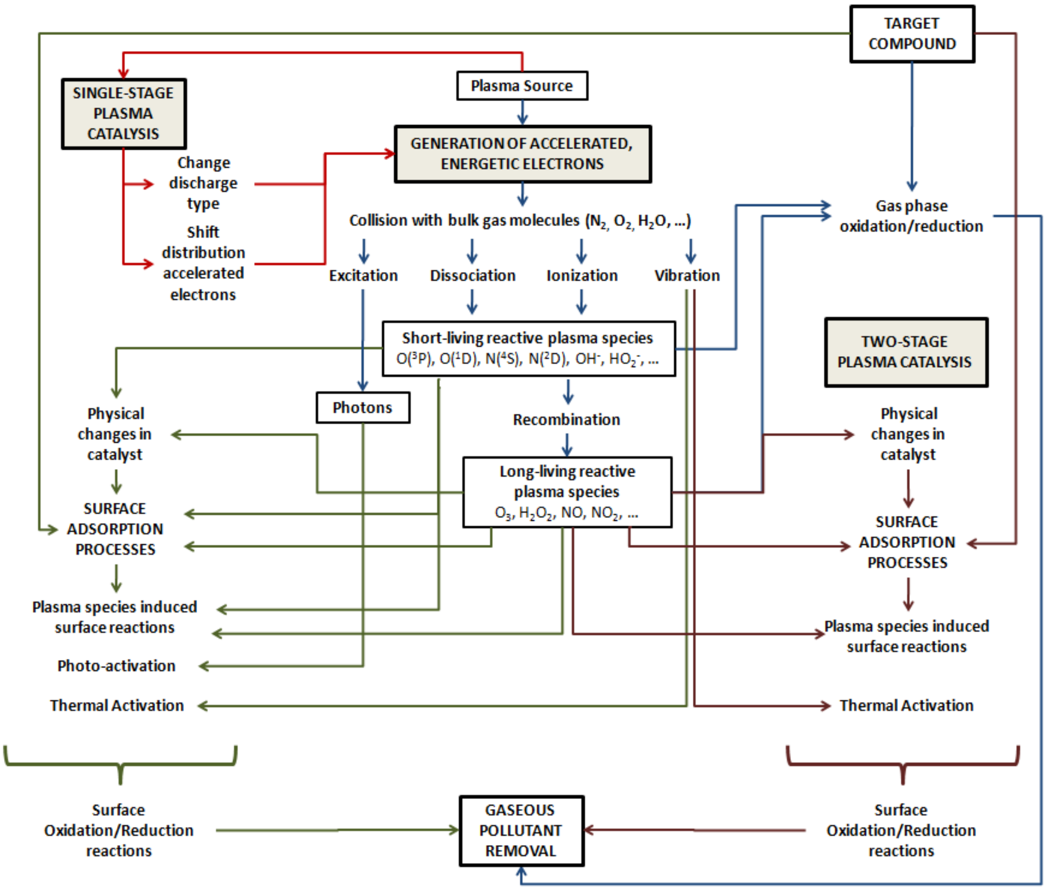

Figure 2.4. Mechanisms of non-thermal plasma catalysis[5]

2.5 Mechanism enhancements in plasma driven catalysis

As mentioned before, in a PDC system, the mechanisms are complicated not only since both plasma and catalysis takes place but also these two have an effect on each other. Two main concerns are present on the treatment of pollutants: (1) effect on plasma by the catalyst and (2) effect on catalysis by the plasma. Chang, et al. (2009), gave a rather good explanation on these performance enhancements. A summary is presented in Fig. 2.5.

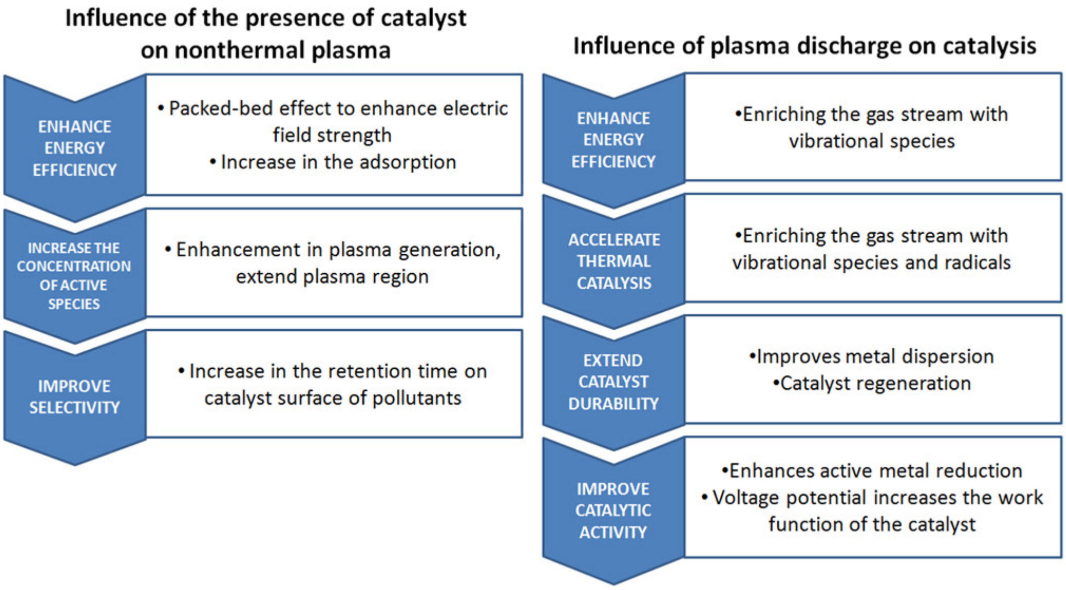

Figure 2.5. Effects on the performance of PDC[9]

2.5.1 *Influence of the presence of catalyst on non-thermal plasma*

Packed bed effect. Placing catalysts inside the discharge region can induce a packed-bed effect where there will be an increase in average electric field due to short distance of contact points in which, energy tends to be consumed by electron-impact dissociation and ionization.

Enhanced plasma generation. The packing helps expand the discharge region because the streamers or micro-discharges are apt to propagate along the solid surface – as the plasma region expands, the concentration of active species would increase due to the higher collision probability between electrons and gas molecules leading to the acceleration of plasma chemistry reactions.

Adsorption of pollutant on catalyst surface. If the catalyst has a significant adsorptive capacity, prolonging the pollutant retention time and increasing the pollutant concentration on the catalyst surface would improve the removal efficiency and selectivity due to higher collision probability. This could also enhance the energy efficiency for pollutant abatement because the fraction of electrons or radicals reacting with the pollutant molecules would be higher as the initial pollutant concentration increases.

2.5.2 *Influence of plasma discharge on catalysis*

Change of the status of the gaseous reactants. A portion of the reactants would be transformed into chemically active species including excited species, radicals and ions – higher internal energy, maybe higher activity for catalytic reactions

Influence of plasma discharge on catalyst properties. Plasma discharge occurring on the catalyst surface can reduce the metal particle size and improve the reduction of the metal precursors impregnated on the catalyst support which could result in higher metal dispersion and reactivity. Increasing metal dispersion can reduce coke deposition and formation which allowing longer catalyst activity and durability.

Change in the work function of the catalyst. When a voltage is applied to the electrodes in a plasma reactor to generate a plasma discharge, this also causes a voltage potential across the catalysts. This change in the work function of the catalyst is called the non-faradaic electrochemical modification of catalytic activity (NEMCA Effect) brought about by the applied voltage across the catalysts. This can be viewed as a special kind of catalytic promotion which changes the specific adsorption capacity of the catalyst as adsorbed ions also participate in the conductive property of the catalyst[10,11].

2.6 Electrical considerations

The dielectric barrier discharge usually operates in the filamentary mode. If the local electric field strength in the discharge gap reaches ignition level, the breakdown starts followed by the development of filaments or microdischarges. A one-sided DBD configuration and its equivalent circuit is presented in Fig. 2.6. For this representation, the capacitance of the dielectric is given as C_d and the gap capacitance as C_g which can be considered as two capacitors connected in series. Since the value of the capacitance of the dielectric is constant, we can take the total capacitance, C, of the reactor as a function of the capacitance of the gap (Eq. 2.1).

$$C = \frac{C_d C_g}{C_d + C_g} = \frac{C_g}{1 + C_g / C_d} = \frac{C_g}{1 + d/(\varepsilon_r g)} = \frac{C_g}{k} \qquad \text{(Eq. 2.1)}$$

Evaluating the electrical parameters involved in a DBD reactor requires a simple circuit (Fig. 2.7) involving a capacitor and a resistor of known values connected in series with the DBD reactor. The DBD reactor is denoted as C and an alternating voltage, U, is fed to the reactor. To measure the current $I(t)$ and the voltage-charge, V-Q, characteristics, a resistor or a capacitor connected in series with the reactor can be used alternatively and the voltage across these loads can be measured by an oscilloscope. However, since a low-current high-voltage source is often used to generate plasma, a high voltage probe is required so as to not to damage the connected oscilloscope.

The discharge power is usually analyzed by the V-Q Lissajous figure method which shows a plot of the instantaneous voltage applied versus the charge accumulated and dissipated per voltage cycle. An example of an idealized V-Q diagram is presented in Fig. 2.8. From this figure, the minimum external voltage U_{min} (at which ignition occurs), the electric energy consumed per voltage cycle E_{el} and the electric power P_{el} can be estimated by the following relations presented below (Eqs. 2.2 to 2.5). The discharge voltage U_D is close to the measured voltage U_{min} can also be calculated. Also, an estimation of the spatially and temporally averaged reduced electric field strength $\langle E/p \rangle$ can be computed as well.

$$E_{el} = \oint U(t)\,dQ = C_{meas}\oint U(t)\,dU_{meas} \equiv \text{Area of } (Q-U) \text{ diagram} \qquad \text{(Eq. 2.2)}$$

$$P_{el} = \frac{1}{T}E_{el} = fE_{el} \qquad \text{(Eq. 2.3)}$$

$$U_D = U_{\min}\frac{1}{1+C_g/C_d} \qquad \text{(Eq. 2.4)}$$

$$\langle E/p \rangle = U_D/(gp) \qquad \text{(Eq. 2.5)}$$

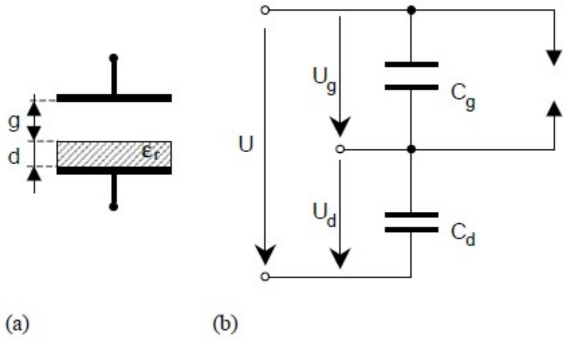

(a) (b)

Figure 2.6. Simplified circuit of a DBD reactor [3]

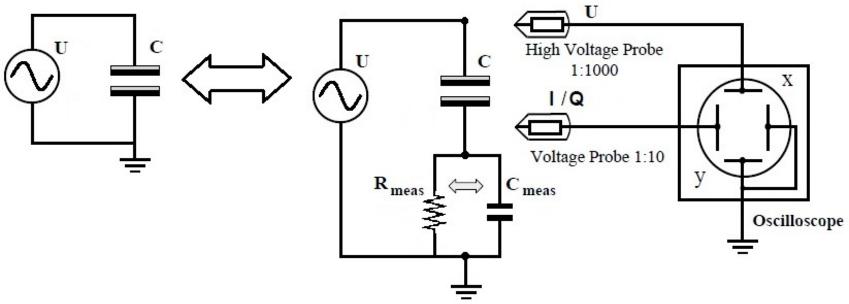

Figure 2.7. Nonthermal plasma reactor electric circuitry[3]

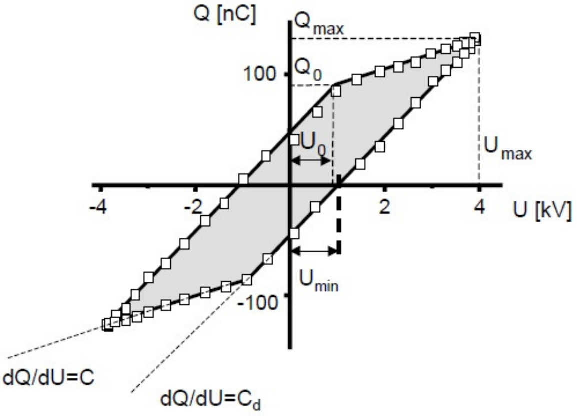

Figure 2.8. Ideal *V-Q* Lissajous diagram[3]

2.7 Choice of catalyst

Similar to heterogeneous catalysis, the catalysts can be introduced in the non-thermal plasma catalysis system in different ways: in form of pellets, foam, honeycomb monolith, as a layer, or a coating on the reactor wall, or the electrodes. Initially, porous adsorbents were used to increase the retention time of VOC molecules and increase the probability of surface reactions with active chemical species produced by the plasma. They were coated or impregnated with noble metals and metal oxides to provide further catalytic activity with the adsorbents functioning as the support material. Semi-conductors and photocatalysts were also used, particularly a lot of researches have used TiO_2 due to its capability to generate electron-hole pairs which can induce oxidation reactions[4].

Different kinds of metals, its oxides and supports have been used as catalysts in plasma catalysis system. Several reviews have been made plasma catalysis systems[4,5,9] and gives an overview of recently published papers involved in plasma catalysis which covers the target pollutant, catalyst used, reactor configuration and its removal efficiency. Regardless of the metal loaded on the support material, TiO_2 performs better than other support materials like γ-Al_2O_3 and zeolites[12,13]. With regards to the loaded metal, performance depends on and amount and type of the loaded metal.

Titanium dioxide, TiO_2, is a very well-known and well-research material due to the stability of its chemical structure, physical and chemical properties. TiO_2 is a material used in various products such as paint pigments, lotions, electrochemical electrodes, capacitors and solar cells. In the past few decades, due to its photocatalytic properties, TiO_2 has been researched extensively for environmental purposes specifically on the treatment of gas and liquid pollutants. During the generation of plasma, photons are created due to the excitation of molecules present in the gas stream. It has become of interest that these photons might lead to the photo-activation of TiO_2 and aid in further treatment of the pollutants[14,15].

As nonthermal plasma driven catalysis systems are mainly concerned with gas-phase and surface-phase reactions, different preparation methods were researched in order to have better active metal dispersion on the catalyst surface. As a benchmark, the conventional impregnation method will be compared with deposition-precipitation methods.

2.8 VOC decomposition in plasma driven catalysis systems

Kim, et al., (2008)[12] as well as a lot of other researchers reported the synergetic effect in plasma-catalyst decomposition of VOCs even at low temperatures where thermal catalysis does not occur. Although the detailed mechanism is still unclear, this is explained by the involvement of the catalyst surface activated by the plasma.

Several hypotheses have been proposed for the possible mechanism in plasma catalysis systems which include ozone, UV, local heating, changes in the work function of the catalyst, activation of lattice oxygen, plasma-induced adsorption/desorption, generation of electron-hole pairs and their subsequent chemical reactions, direct interaction of gas-phase radicals with the catalyst surface and the adsorbed molecules, etc. (Fig. 2.9). An interesting concern here is the plasma-induced adsorption/desorption and decomposition of adsorbed molecules the can clean the active sites of the catalysts[12]. This in effect, leads to the high performance of the catalyst and improve its catalytic activity.

In terms of chemical and catalytic reactions, it is proposed that these reactions occur via two models: (1) Langmuir-Hinshelwood model and the (2) Eley-Rideal model (Fig. 2.9). In the Langmuir-Hinshelwood model, both the reactants need to be adsorbed on the surface, followed by migration to the active site to induce chemical reactions. In the Eley-Rideal model however, only on reactant is adsorbed on the surface and the other exists in the gas-phase.

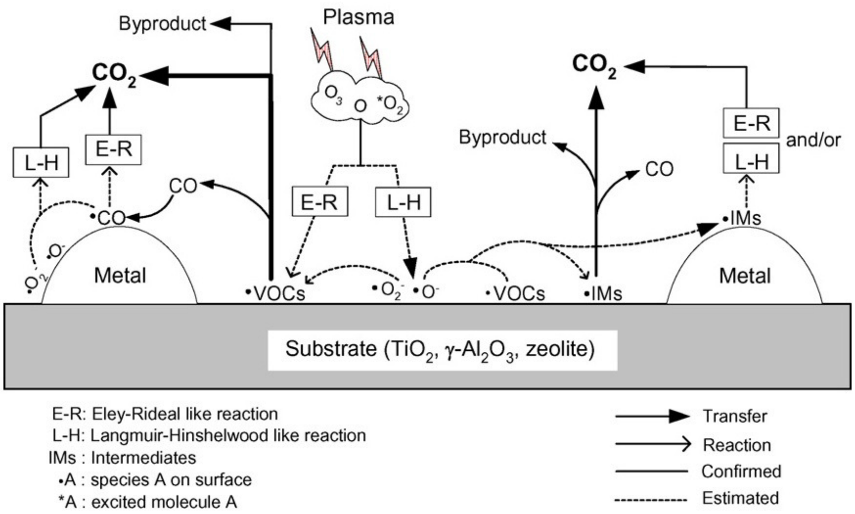

Figure 2.9. Plausible mechanism for plasma catalytic reactions[12]

Chapter References

[1] **Whitehead, J. C.** *Plasma catalysis: A solution for environmental problems.* Pure Applied Chemistry, 82, 6, (2010) 1329-1336

[2] **Chirokov, A., Gutsol, A., Fridman, A.** *Atmospheric pressure plasma of dielectric barrier discharges.* Pure Applied Chemistry, Vol. 77, No.2 (2005) 487-495

[3] **Wagner, H.E., Brandendurg, R., Kozlov, K.V., Sonnenfeld, A., Michel, P., Behnke, J.F.** *The barrier discharge: basic properties and applications to surface treatment.* Vacuum 71 (2003) 417-436

[4] **Vandernbroucke, A. M., Morent, R., De Geyter, N., Leys, C.** *Non-thermal plasmas for non-catalytic and catalytic VOC abatement.* Journal of Hazardous Materials 195 (2011) 30-54

[5] **Dewulf, J., Van Durme, J., Leys, C., Van Langenhove, H.** *Combining non-thermal plasma with heterogeneous catalysis in waste gas treatment: a review.* Applied Catalysis B: Environmental, 78 (2007) 324-333.

[6] **Lee, H.M., Chang, M.B., Wei, T.C.** *Kinetic modelling of ozone generation via dielectric barrier discharges.* Ozone: Science and Engineering 26 (2004) 551-562

[7] **Chang, M.B., Wu, S.J.** *Experimental study on ozone synthesis via dielectric barrier discharges.* Ozone Science & Engineering, 19 (1997) 241-254

[8] **Gibalov, V.I., Pietsch, G.J.** *On the performance of ozone generators working with dielectric barrier discharges.* Ozone: Science and Engineering 28 (2006) 119-124

[9] **Chen, H. L., Lee, H. M., Chen, S. H., Chang, M. B., Yu, S. J., Li, S. N.** *Removal of volatile organic compounds by single-stage and two-stage plasma catalysis systems: A review of the performance enhancement mechanisms, current status, and suitable applications.* Environmental Science Technology, 43 (2009) 2216-2227

[10] **Leiva, E.P.M., Sanchez, C.G.** *NEMCA effect: why are the work function changes of the gas exposed catalyst-electrode surface one-to-one related to the changes in the catalyst working electrode potential?* Journal of Solid State Electrochemistry 7 (2003) 588-592

[11] **Vayenas, C.G., Bebelis, S., Yentekakis, V., Tsiakaras, P., Karasali, H.** *Non-faradic electrochemical modification of catalytic activity. Reversible promotion of platinum metal catalysts.* Platinum Metals Review 34 (1990) 122-130

[12] **Kim, H.H. Ogata, A., Futamura, S.** *Oxygen partial pressure-dependent behavior of various catalysts for the total oxidation of VOCs using cycled system of adsorption and oxygen plasma.* Applied Catalysis B: Environmental 79 (2008) 356-367

[13] **Kim, H.H., Lee, Y.H, Ogata, A., Futamura, S.** *Plasma-driven catalyst processing packed with photocatalyst for gas-phase benzene decomposition.* Catalyst Communications, 4 (2003) 347-351

[14] **Henderson, M. A.** *A surface science perspective on TiO2 photocatalysis.* Surface Science Reports 66 (2011) 185-297

[15] **Ohtani, B.** *Photocatalysis A to Z- What we know and what we do not know in a scientific sense.* Journal of Photochemistry and Photobiology C: Photochemistry Reviews 11 (2010) 157-178

[16] **Sandoval, A., Aguilar, A., Louis C., Traverse, A., Zanella, R.** *Bimetallic Au-Ag/TiO2 catalyst prepared by deposition-precipitation: High activity and stability in CO oxidation.* Journal of Catalysis 281 (2011) 40-49

[17] **Zanella, R., Delannoy, L., Louis, C.** *Mechanism of gold precursors onto TiO2 during the preparation oby cation adsorption and deposition-precipitation with NaOH and urea.* Applied Catalysis A: General 291 (2005) 62-72

[18] **You, X., Chen, F., Zhang, J. Anpo, M.** *A novel deposition precipitation method for preparation of Ag-loaded titanium dioxide.* Catalysis Letters, Vol. 102, Nos. 3-4 (2005)

[19] **Zhang, J., Xiao, L., Cong, Ye.** *Preparation and Characterization of multi-functional titanium dioxide photocatalysts.* Topics in Catalysis Vol. 47, Nos. 3-4 (2008) 122-130

Chapter 3

CATALYST PREPARATION AND CHARACTERIZATION

The different properties and characteristics of catalysts highly depend on their preparation method and greatly affects its performance when used in any catalytic process. This chapter discusses the different preparation methods used to prepare Ag/TiO_2, Mn/TiO_2, and $Ag\text{-}Mn/TiO_2$ catalysts as well as its characterization results.

3.1 Catalyst preparation

One benefit of working with non-thermal plasma catalysis is that it can be operated at room temperature. In this regard, catalyst preparation, specifically by impregnation method, is no longer limited by preparing catalysts at high temperatures to be able to work within the operating temperature of the decomposition process as in thermal catalysis. In this study, catalysts were specifically prepared to have various metal oxidation states so as to compare its efficiency in a non-thermal plasma catalysis system.

Addition of metal on the titanium dioxide support catalyst were done either by impregnation method or by deposition-precipitation method with varying metal loading of 1%, 3% and 5% by weight. The base catalyst used was anatase type TiO_2 pellets obtained commercially from Sakai Chemical Industry Co., Ltd., Japan (CS-300S-12). Manufacturer specifications indicate diameters of 1 mm to 2 mm with an average diameter of 1.6 mm, mechanical strength of 0.5 kg/piece, density of 0.9 kg/L, BET surface area of 74 m^2/g and pore volume of 0.4 mL/g. The pellets were sieved using 1.0, 1.4, 1.7, and 2.0 aperture sieves and pellets collected between 1.4 and 1.7 sieves were used as the base catalysts. All other chemicals used for catalyst preparation were used without further purification. A list of all chemicals used for catalyst preparation are listed in Table 3.1. The metal precursors used for Ag/TiO_2 catalysts are silver nitrate and silver chloride; for Mn/TiO_2 catalysts, manganese nitrate hexahydrate; and for $Ag\text{-}Mn/TiO_2$ catalysts are silver nitrate and manganese nitrate hexahydrate. A schematic diagram showing the summary of the preparation procedures is presented in Figure 3.1.

3.1.1 Impregnation method

In the impregnation method (IP), the metal precursor used were silver nitrate and manganese nitrate hexahydrate. The metal precursor was first dissolved in deionized water and appropriate volumes were then added to a beaker containing the base TiO_2. The mixture was aged for 24 hours under room temperature before drying in a convection oven at 100^oC. The impregnated catalysts were then analyzed by a Rigaku Thermoplus TG8120 thermogravimetric-differential thermal analyzer to determine its thermogravimetric behavior. Based from the results, Ag/TiO_2 catalysts were calcined at 500°C under air flow; Mn/TiO_2 catalysts were calcined at 350°C and 600°C under air flow, and at 800°C under nitrogen flow; and Ag-Mn/TiO_2 catalysts at 350°C under air flow. Calcination of the catalysts were done for 4 hours. Impregnated catalysts were labelled as either IP*x* for Ag/TiO_2 and Ag-Mn/TiO_2 catalysts, or IP*x*T*y* for the Mn/TiO_2 catalysts where *x* represents the metal loading amount and *y* represents the calcination temperature.

Table 3.1. List of chemicals used for catalyst preparation

Item	Specifications
Titanium dioxide (TiO_2)	Anatase pellets, Sakai Chemical Ind. Co. Ltd.
Silver nitrate ($AgNO_3$)	99.8%, Wako Ltd.
Silver chloride (AgCl)	99.9%, Sigma Aldrich
Manganese nitrate ($Mn(NO_3)_2{\cdot}6H_2O$)	98%, Wako Ltd.
Sodium Hydroxide (NaOH)	1.0 N, Fluka
Ammonia (NH_3)	28% - 30%, Kanto Chemical Co., Ltd.
Hydrogen Peroxide (H_2O_2)	30%, Wako Ltd.

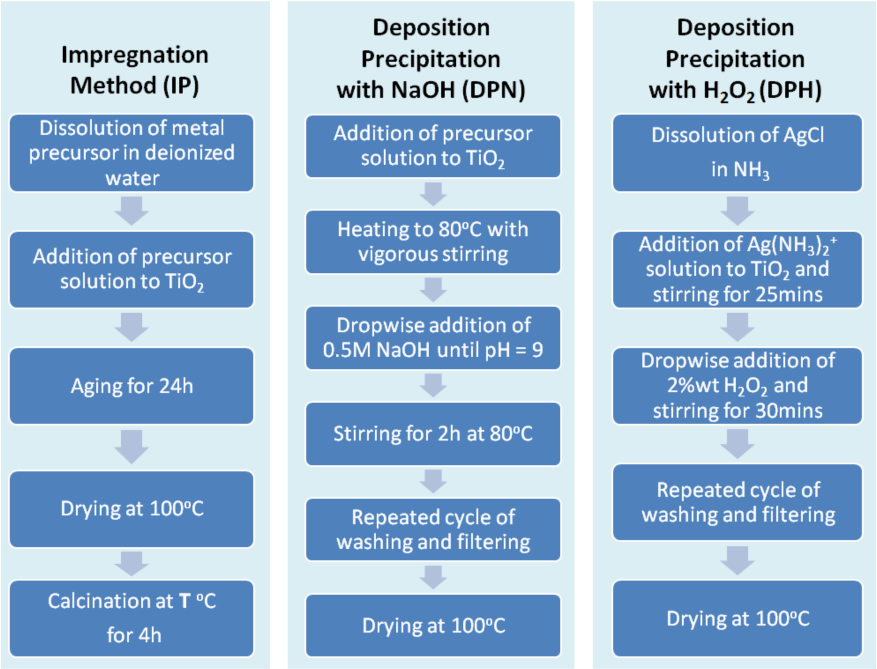

Figure 3.1. Summary of catalyst preparation methods:
IP and DPN for Ag/TiO_2, Mn/TiO_2 and Ag-Mn/TiO_2; and DPH for Ag/TiO_2 catalysts

3.1.2 Deposition-precipitation method with sodium hydroxide

Similarly for the deposition-precipitation method with sodium hydroxide (DPN), silver nitrate and manganese nitrate hexahydrate were used as the metal precursors. The metal precursor was first dissolved in deionized water and appropriate volumes were then added to a beaker containing the base TiO_2. The mixture was heated to 80°C before adding 0.5 M NaOH dropwise until a pH of 9 was reached. The mixture was continuously stirred and maintained at 80°C for 2 hours after which, the catalysts underwent a repeated cycle of washing and filtering with deionized water until the filtrate tested a neutral pH. The catalysts were then dried in a convection oven at 100°C.

The slow addition of sodium hydroxide to the mixture at an elevated temperature (80°C) facilitated the precipitation of the metal on the TiO_2 surface. For Ag/TiO_2 catalysts, addition of NaOH to $AgNO_3$ promoted the precipitation of Ag_2O on the catalyst surface (Eq. 3.1)[1,2]. In the case of Mn/TiO_2 catalysts, this will produce manganese hydroxides with different oxidations states and aging of the precipitates will lead to the formation of either Mn_3O_4 or MnO_2 (Eqs. 3.2-6)[3]. Catalysts prepared by this method were labelled as DPN*x* catalysts where *x* represents the metal loading amount.

$$2AgNO_3 + 2NaOH \rightarrow Ag_2O \downarrow + 2NaNO_3 + H_2O \qquad \text{(Eq. 3.1)}$$

$$Mn^{2+} + 2OH^- \rightleftarrows Mn(OH)_2 \qquad \text{(Eq. 3.2)}$$

$$4Mn(OH)_2 + O_2 + 2H_2O \rightarrow 4Mn(OH)_3 \qquad \text{(Eq. 3.3)}$$

$$2Mn(OH)_2 + O_2 + 2H_2O \rightarrow 2Mn(OH)_4 \qquad \text{(Eq. 3.4)}$$

$$Mn(OH)_2 + 2Mn(OH)_3 \rightarrow Mn_3O_4 + 4H_2O \qquad \text{(Eq. 3.5)}$$

$$Mn(NO_3)_2 + 2NaOH + O_2 \rightarrow MnO_2 + 2NaNO_3 + H_2O \qquad \text{(Eq. 3.6)}$$

3.1.3 Deposition-precipitation method with hydrogen peroxide

To compare the effect of the metal precursor, Ag/TiO_2 catalysts were also prepared using the deposition precipitation method with hydrogen peroxide (DPH) and silver chloride as the metal precursor. Silver chloride was first dissolved in ammonia to form diammineargentate complex ion solution and this solution was added to a beaker containing the base TiO_2. The mixture was stirred for 25 min and 2% by weight hydrogen peroxide solution was added dropwise to promote the precipitation of Ag metal on the TiO_2 surface (Eq. 3.7)[4,5]. The mixture was continuously stirred for 30 min before repeatedly undergoing filtering and washing until the filtrate showed a neutral pH and then dried in an oven at 100°C. Catalysts prepared by this method were labelled as DPH*x* catalysts where *x* represents the metal loading amount.

$$2\left[Ag(NH_3)_2\right]^+ + H_2O_2 + 2OH^- \rightarrow 2Ag \downarrow + O_2 + 4NH_3 + 2H_2O \qquad \text{(Eq. 3.7)}$$

3.2 Catalyst characterization

The structural and chemical properties of the prepared catalysts were characterized by thermogravimetric and different thermal analysis (TG-DTA), X-ray powder diffraction analysis (XRD), nitrogen adsorption Brunauer-Emmett-Teller method (BET), X-ray photoelectron spectroscopy (XPS), and scanning electron microscopy - energy dispersive X-ray spectroscopy (SEM-EDS).

Investigation of the thermal behavior of the catalysts by TG-DTA were primarily performed to determine the calcination temperature to be used in the impregnation method. Thermogravimetric analysis provided information on the phase transitions (i.e. vaporization and desorption of moisture and volatiles) as well as solid-gas reactions (i.e. oxidation-reduction reactions) with increase in temperature. By plotting the weight profile of the catalyst against temperature, the temperatures at which phase transitions and solid-gas reactions occurred were determined.

Catalyst crystal structure and size were analyzed by XRD and its specific surface area by BET method. Confirmation of the presence of the metal, its chemical binding energy and oxidation state were analyzed by XPS fitted with a monochromated Al Kα source at 1486.6 eV. The anode was operated at 300 W and the analyzer at a constant pass energy of 23.5 eV with a resolution of 0.025 eV. The binding energy shifts due to surface charging were corrected using the C 1s level at 284.8 eV from adventitious carbon. The XPS peaks were resolved assuming Lorentzian-Gaussian line profiles and a Shirley function was applied for background correction. And lastly, surface morphology and metal distribution were analyzed by SEM-EDS. A list of the instruments used are presented in Table 3.2.

Table 3.2. List of equipment used for catalyst characterization

Item	Equipment Specifications	Purpose/Analysis
TG-DTA	Rigaku Thermoplus TG8120	Thermogravimetric analysis
XRD	Rigaku X-ray Diffractometer	Crystal structure and size
N_2 adsorption	Autosorb-1, Quantachrome Instruments; Belsorp-Max, BEL Japan	Specific surface area
XPS	ULVAC-PHI 1600	Metal binding energy and oxidation state
SEM	JEOL JSM-5310LV, Keyence VE-8800	Surface morphology
SEM-EDS	JEOL JSM-5310LV, JEOL JCM-6000	Metal distribution

3.2.1 Ag/TiO_2

The thermogravimetric behavior of the impregnated Ag/TiO_2 catalyst is presented in Figure 3.2. The minima points in the DTG curve represents at which temperature the phase transitions and oxidation-reduction reactions occurred. Initial weight loss starting from about 50°C is attributed to the evaporation of adsorbed water and succeeding weight loss steps are attributed to the decomposition of silver nitrate into silver oxide and finally into silver metal. Stern[6] in his review paper has indicated that the decomposition of silver nitrate into silver metal starts as early as 120°C. In Figure 3.2, differential weight loss at around 500°C became relatively stable and this was chosen as the calcination temperature for Ag/TiO_2 catalysts.

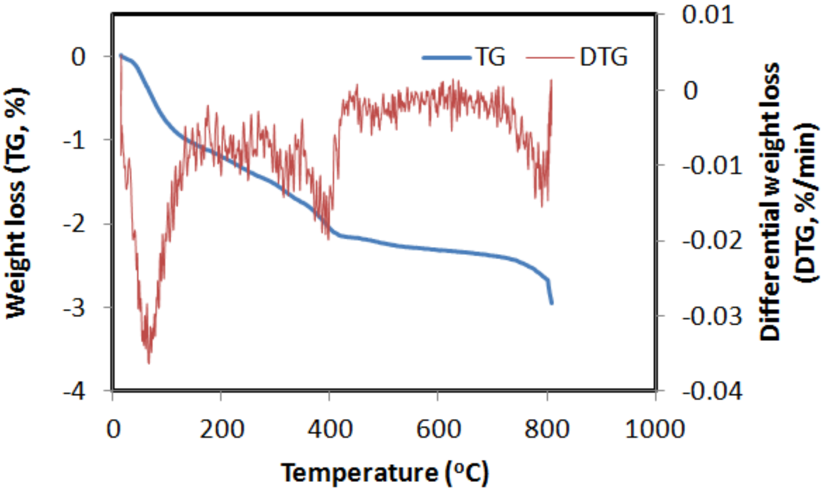

Figure 3.2. Thermogravimetric behavior of impregnated Ag/TiO_2 catalysts under air flow

Bulk crystal structure and size were determined by XRD and the diffractograms for 5% Ag/TiO_2 catalysts prepared by IP, DPN, and DPH method are presented in Figure 3.3. All prepared catalysts retained its anatase (PDF# 21-1272) crystal structure, however, silver or any of its oxides were not seen in the XRD diffractograms probably due to the small amount loaded on TiO_2. Catalyst crystal size and specific surface area are summarized in Table 3.3. Anatase crystal size for all catalysts were between 20 nm to 22 nm similar to the base TiO_2.

The specific surface area based from the characterization results of N_2 adsorption using BET method showed that with increasing Ag loading, the specific surface area decreased which was prominently observed in the IP catalysts. Base TiO_2 had a specific surface area of 64.95 m^2/g but was reduced to 49.00 m^2/g in the IP5 catalyst while DPN and DPH catalysts showed insignificant change in the specific surface area. This was mainly due to the calcination at 500°C in the preparation of the IP catalysts. Although there was no significant change in the degree of crystallinity of the catalysts as presented in their crystal size, it is assumed that the silver loaded on the IP catalysts agglomerated on the catalyst surface as well as within its pores which reduced its specific surface area.

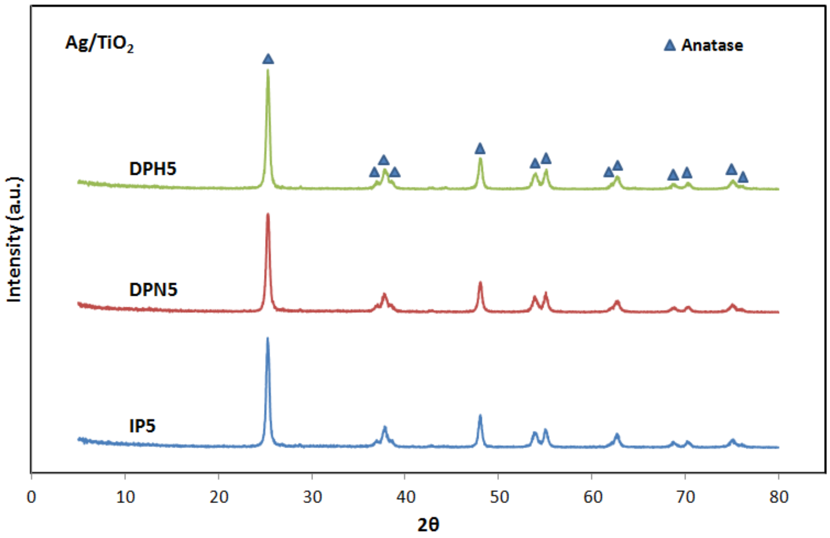

Figure 3.3. XRD diffractograms of 5%Ag/TiO$_2$ prepared by IP, DPN and DPH method

Table 3.3. Summary of catalyst structural properties for TiO$_2$ and prepared Ag/TiO$_2$ catalysts

Catalyst	Crystal size, nm	Specific surface area, m^2/g
TiO$_2$	20	64.95
IP1	20	61.64
IP3	22	53.54
IP5	22	49.00
DPN1	21	64.73
DPN3	21	64.60
DPN5	20	63.28
DPH1	21	65.54
DPH3	22	65.14
DPH5	21	64.94

The chemical binding energy and the chemical state of the catalysts were investigated by XPS. Depending on the preparation method, various oxidation states of silver was expected to be produced. The Ti 2p, Ag 3d, and C 1s core level XPS high-resolution spectra were recorded for TiO$_2$ and the prepared Ag/TiO$_2$ catalysts. The spectra were decomposed assuming Lorentzian-Gaussian line profiles with a Shirley function for background correction and binding energy shifts were adjusted using the C 1s level at 284.8 eV from adventitious carbon. Resolution of the Ti 2p spectrum and Ag 3d spectrum were fitted to conform with the differences in binding energies (BEs) of their respective spin-orbit pairs, 5.7 eV for titanium oxide and 6.0 eV for silver oxide.

Figure 3.4 shows the narrow scans of the Ti 2p and Ag 3d peaks for the different catalysts. The peak for the Ti $2p_{3/2}$ state for TiO_2 catalyst was narrow and sharp with slight asymmetry and has a binding energy of 458.2 eV with a full width at half maximum (FWHM) of 1.13 and was attributed to the tetravalent Ti^{4+} state. As silver was incorporated in the catalysts, the Ti 2p peaks became broader for IP and DPN catalysts but retained a similar value for the DPH catalyst. Curve-fitting analysis of the Ti $2p_{3/2}$ peaks for the different catalysts revealed two peaks for the DPN catalyst at 458.2 eV and at 457.4 eV, which corresponds to the tetravalent Ti^{4+} state and trivalent Ti^{3+} states of Ti, respectively[7,8]. Although the FWHM of the Ti $2p_{3/2}$ of the IP catalyst increased to 1.55, curve-fitting analysis did not show the Ti^{4+} and Ti^{3+} states of Ti.

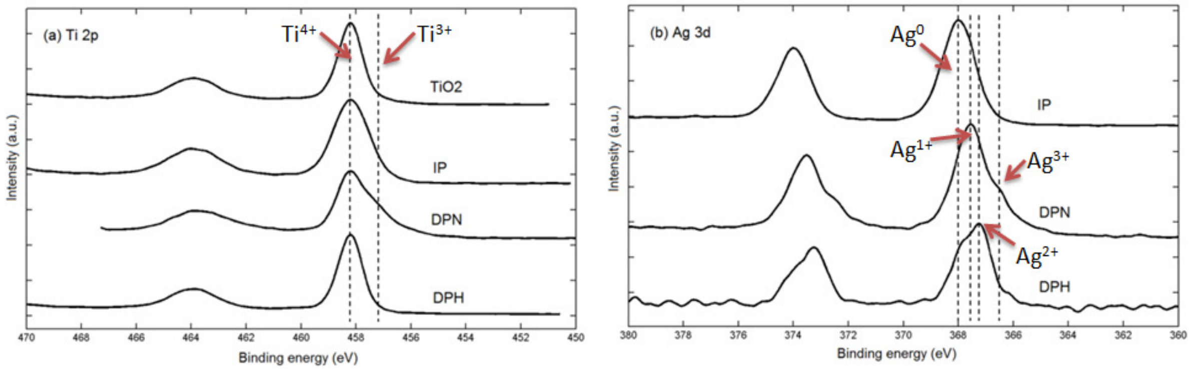

Figure 3.4. XPS high-resolution spectra of (a) Ti 2p and (b) Ag 3d peak profiles for TiO_2 and Ag/TiO_2 catalysts

The binding energy of the Ag 3d peaks exhibit a negative shift as oxidation state is increased and these shifts are in the range of a few tenths of an eV[9]. Resolution of the Ag 3d spectra showed peaks at 368.0 eV for Ag^0, 367.6 eV for Ag^+, 367.3 eV for Ag^{2+} and 366.5 eV for Ag^{3+}. These results match well with previous studies found in literature[9-11]. The Ag $3d_{5/2}$ XPS signal found at 366.5 eV can be attributed to a chemical state of Ag^{3+}, which was first found in doped TiO_2, and this could explain the presence of Ti^{3+} in this sample. Previous works also reported the existence of Ag^{3+} in the form of Ag_2O_3, which could easily decompose into Ag_2O at room temperature in air[11]. Since the peak for Ag^{3+} was found for the DPN catalyst even after long storage period, this indicates that Ag in this catalyst exist as both surface Ag oxide (Ag_2O_3) and substitutional Ag formed by the substitution of Ti sites by Ag atoms in the crystalline lattice.

From these results, it can be inferred that IP catalyst is composed of metallic Ag while DPN catalyst was composed mainly of Ag_2O and a small fraction of Ag_2O_3, and finally for DPH catalyst, mainly composed of AgO and a small fraction of metallic Ag. Table 3.4 shows the Ti $2p_{3/2}$ and Ag $3d_{5/2}$ peak positions for the different chemical species, FWHM and content fractions for the catalysts.

Table 3.4. Chemical binding energy properties of TiO_2 and Ag/TiO_2 catalysts determined by XPS

Catalyst	Chemical Species	Position (eV)	FWHM (eV)	Fraction	Chemical Species	Position (eV)	FWHM (eV)	Fraction
TiO_2	Ti^{4+}	458.2	1.13	1.0				
Ag/TiO_2 (IP)	Ti^{4+}	458.2	1.55	1.0	Ag^0	368.0	1.43	1.0
Ag/TiO_2 (DPN)	Ti^{3+} Ti^{4+}	457.4 458.2	1.65 1.10	0.54 0.46	Ag^{1+} Ag^{3+}	367.6 366.5	1.16 0.60	0.78 0.22
Ag/TiO_2 (DPH)	Ti^{4+}	458.2	1.05	1.0	Ag^0 Ag^{2+}	368.0 367.3	0.84 1.09	0.24 0.76

Surface morphologies and active metal dispersion on the catalyst surface were analyzed by SEM-EDS. Figure 3.5 shows the SEM images of the prepared Ag/TiO_2 catalysts by IP, DPN, and DPH methods and its corresponding metal distribution in Figure 3.6. The SEM images showed that in IP catalysts, small aggregate structures were formed due to calcination of the catalysts which were not present in either the DPN or the DPH catalysts. Elemental mapping of these catalysts showed that with increasing Ag loading, Ag density and dispersion on the catalyst surface also increased, with DPN and DPH catalysts had higher metal surface density than IP catalysts even with the same metal loading amount. This was expected as DPN and DPH catalyst had Ag directly precipitated on the TiO_2 surface as compared to IP catalysts where the long aging time of 24 hours allowed the silver to enter into the pores of TiO_2 by capillary forces, thus having lower surface metal concentration.

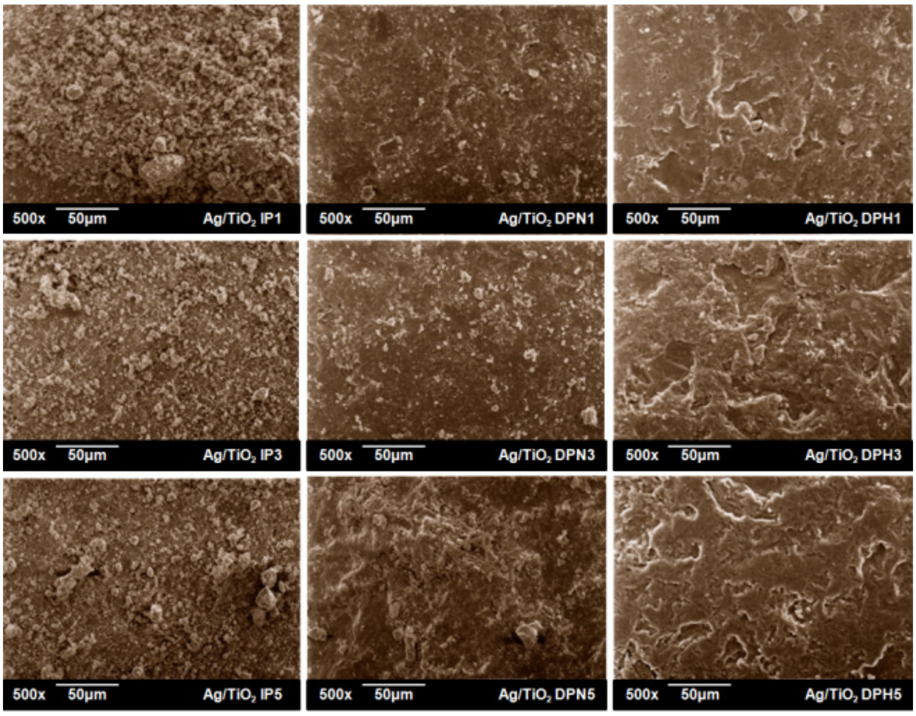

Figure 3.5. SEM images of the prepared Ag/TiO$_2$ catalysts

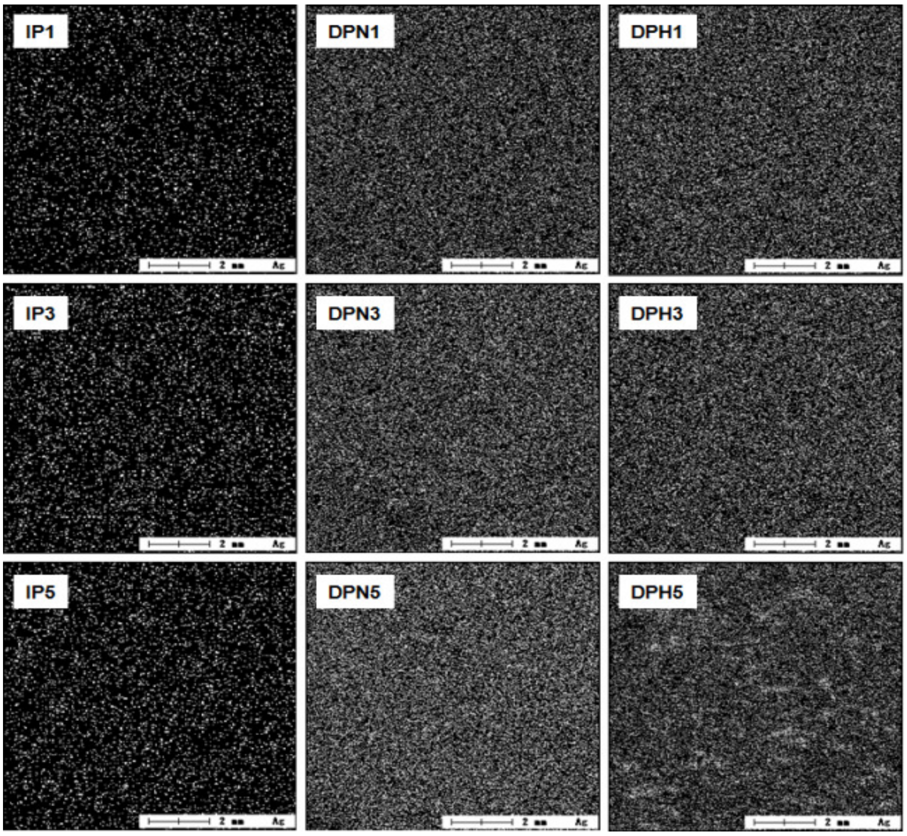

Figure 3.6. SEM-EDS digital mapping of Ag on the prepared Ag/TiO$_2$ catalysts

3.2.2 Mn/TiO$_2$

The thermogravimetric behavior of the impregnated Mn/TiO$_2$ under air and nitrogen atmosphere was analyzed by TG-DTA and is presented in Figure 3.7. Similar to the impregnated Ag/TiO$_2$ catalyst, the minima points in the DTG curve indicate the temperature values at phase transitions and oxidation-reduction reactions occurred. Based from temperature programmed reduction studies found in literature[12], manganese oxides reduce in the following sequence when heated: $Mn(OH)_x > MnO_2 > Mn_2O_3 > Mn_3O_4 > MnO$. From the DTG curve, initial weight loss was attributed to the evaporation of adsorbed water which starts at around 50°C followed by the phase transitions of manganese oxides. Since the precursor used was manganese nitrate hexahydrate, the formation of manganese hydroxide from hydrolysis with water was produced. The second peak present at around 210°C was attributed to the reduction of manganese hydroxide to manganese (IV) oxide, followed by the reductions to manganese (III) oxide, manganese (II,III) oxide, and to manganese (II) oxide. Based from the DTG curve, these reduction reactions occur at temperatures of 315°C, 585°C, 780°C and 900°C.

The thermogravimetric behavior under nitrogen atmosphere was also investigated and the phase transitions occurred at lower temperatures of 210°C, 295°C, 500°C, and 760°C due to low oxygen conditions which favors reduction reactions thermodynamically. From these results, calcination temperatures of 350°C and 600°C under air atmosphere and 800°C under nitrogen atmosphere were selected.

To understand the structural properties, the catalysts were analyzed by XRD and BET method. The bulk crystal structure and size were determined by XRD and the diffractograms for 5% Mn/TiO$_2$ catalysts prepared by IP and DPN methods are presented in Figure 3.8. All prepared catalysts retained its TiO$_2$ anatase crystal structure except for IP catalysts calcined at T = 800°C (IPT800) where TiO$_2$ rutile phase (PDF# 21-1276) was also observed. Aside from the TiO$_2$ crystal structure, peaks pertaining to Mn$_2$O$_3$ in IPT600 (PDF# 41-1442), MnTiO$_3$ in IPT800 (PDF# 29-0902), and Mn$_3$O$_4$ in DPN (PDF# 24-0734) were observed in relatively smaller peak intensities. Although MnO$_2$ was expected to be formed in IPT350, the peaks pertaining to MnO$_2$ were not found in the XRD diffractogram.

For IPT800 catalysts, the high calcination temperature and low oxygen conditions lead to the formation of MnTiO$_3$ under the following reactions indicated below[13]. Since MnO$_2$ and Mn$_3$O$_4$ are expected to be formed at temperatures below 800°C, these equations are all probable reaction pathways for the formation of MnTiO$_3$. Furthermore, since the calcination was done under nitrogen atmosphere, this favored the formation of MnTiO$_3$ thermodynamically.

$$2MnO_2 + 2TiO_2 \rightarrow 2MnTiO_3 + O_2 \qquad \text{(Eq. 3.8)}$$

$$2Mn_3O_4 + 6TiO_2 \rightarrow 6MnTiO_3 + O_2 \qquad \text{(Eq. 3.9)}$$

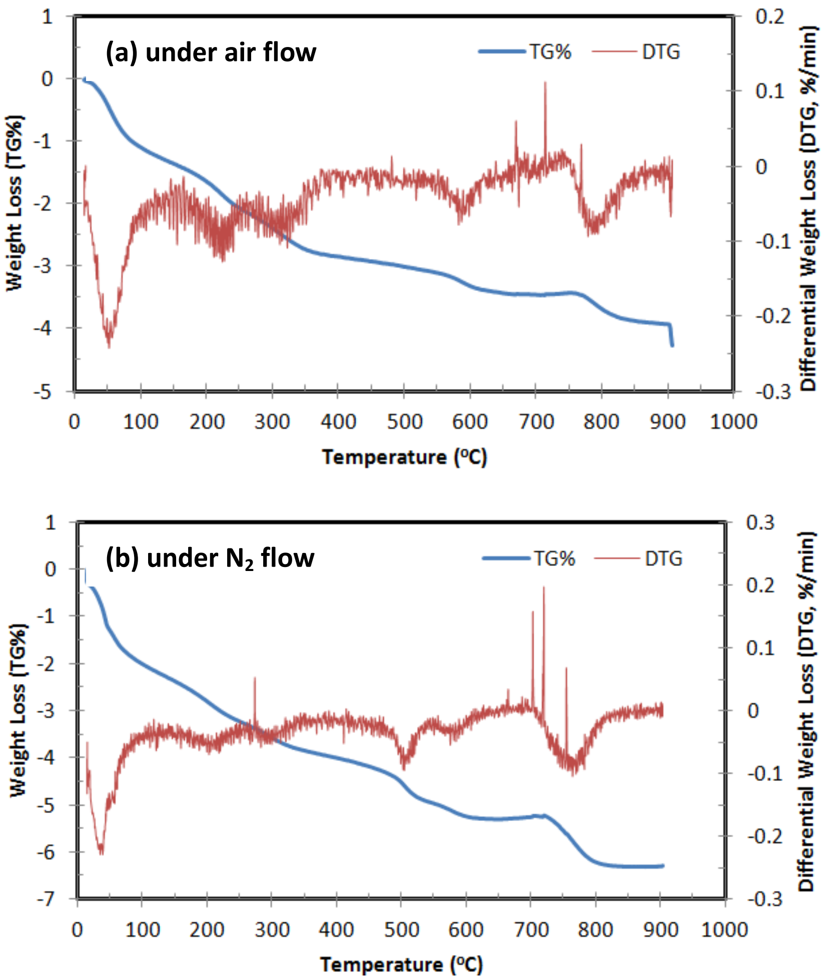

Figure 3.7. Thermogravimetric behavior of impregnated Mn/TiO_2 catalysts under (a) air flow and (b) N_2 flow

For the IPT800 catalysts, with increasing Mn loading, the intensity of the rutile peak also increased (Fig. 3.9). Spurr-Myers equation (Eq. 3.10)[14] was used to determine the anatase fraction where I_R and I_A represent the peak intensities of the rutile and anatase phase. Anatase fractions of 0.9382, 0.3321, and 0.1209 were obtained for catalysts IP1T800, IP3T800, and IP5T800, respectively. The increase in the rutile fraction is attributed to the formation of $MnTiO_3$. At higher manganese loading, more manganese was available for reaction with TiO_2 to form $MnTiO_3$. This reaction coupled with the high temperature lead to the reconstruction of the anatase phase and promoted the formation of the rutile phase[14].

$$f = \frac{1}{1 + 1.265\frac{I_R}{I_A}} \qquad \text{(Eq. 3.9)}$$

In DPN, neutralization of manganese nitrate precursor solution in sodium hydroxide resulted in the precipitation of Mn^{2+} species which then hydrolyzed to form $Mn(OH)_2$. This can undergo further oxidation in air to produce $Mn(OH)_3$. Aging and drying of these precipitates resulted in the crystallization of Mn_3O_4.

$$Mn^{2+} + OH^- \leftrightarrow Mn(OH)_2 \qquad \text{(Eq. 3.10)}$$

$$4Mn(OH)_2 + O_2 + 2H_2O \rightarrow 4Mn(OH)_3 \qquad \text{(Eq. 3.11)}$$

$$Mn(OH)_2 + Mn(OH)_3 \rightarrow Mn_3O_4 + 4H_2O \qquad \text{(Eq. 3.12)}$$

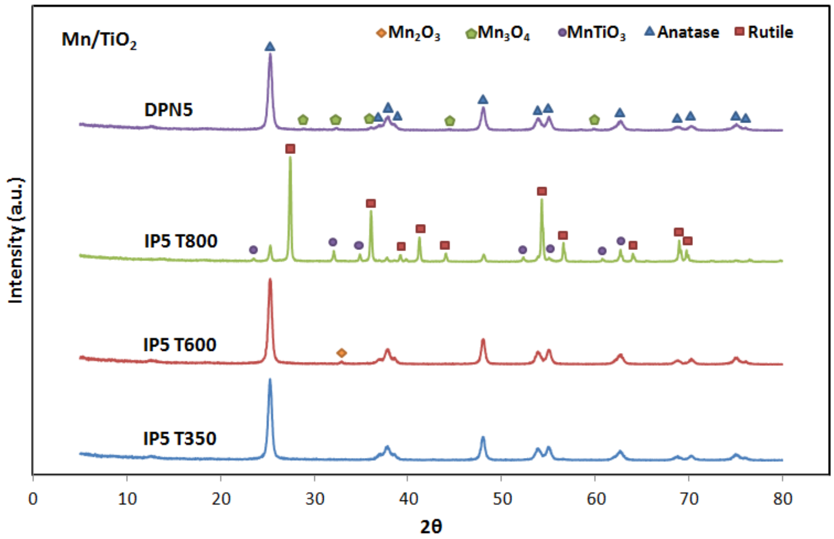

Figure 3.8. XRD diffractograms of 5% Mn/TiO_2 prepared by IP and DPN methods

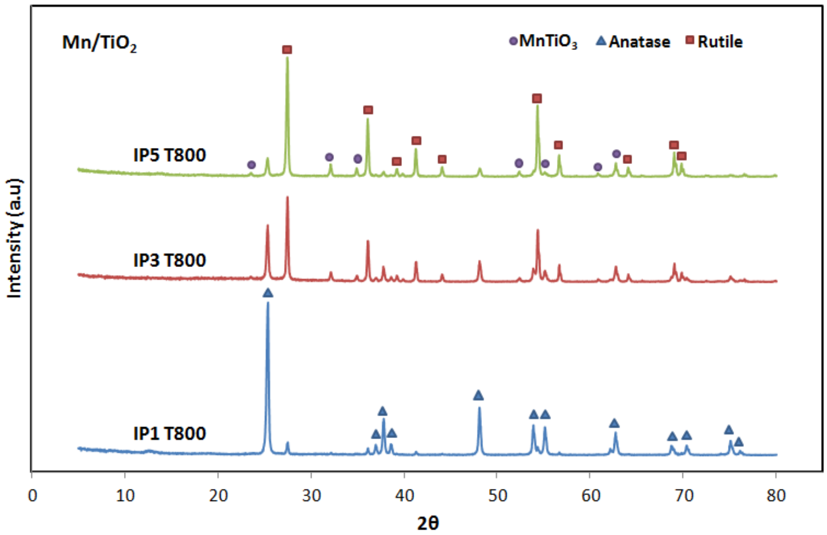

Figure 3.9. XRD diffractograms of Mn/TiO_2 prepared by IP method calcined at T = 800°C.

Crystal size and specific surface area of the Mn/TiO_2 catalysts are summarized in Table 3.5. Anatase crystal size for the prepared catalysts slightly decreased from the base TiO_2 from 20 nm to 18 nm and 19 nm except for those prepared by IP method calcined at 800°C. These catalysts had significantly larger anatase crystal size ranging from 31 nm to 33 nm. As IPT800 catalysts also showed TiO_2 rutile crystal phase, rutile crystal size is also indicated in Table 3.5. Results show that with increasing manganese loading, rutile crystal size decreased from 46 nm in IP1T800 to 31 nm in IP5T800. The changes in both the anatase and rutile crystal size is attributed to the formation of $MnTiO_3$ as part of the bulk structure of the catalyst. The anatase crystal structure is disrupted as TiO_2 reacted with manganese to form $MnTiO_3$. This resulted in the reorganization of the atoms in bulk structure of TiO_2 which also initiated the transition from anatase to rutile under high calcination temperature. With increasing manganese loading, more manganese was available to react and form $MnTiO_3$ which also promoted the transition of the TiO_2 crystal structure from anatase to rutile crystal phase.

Table 3.5. Summary of catalyst structural properties for TiO_2 and prepared Mn/TiO_2 catalysts

Catalyst	Crystal size, nm	Specific surface area, m^2/g
TiO_2	20	64.95
IP1 T350	18	76.49
IP3 T350	18	76.91
IP5 T350	18	72.36
IP1T600	19	71.97
IP3 T600	18	66.12
IP5 T600	19	61.57
IP1 T800	A 31 R 46	51.64
IP3 T800	A 32 R 36	1.54
IP5 T800	A 33 R31	2.04
DPN1	18	74.86
DPN3	18	74.45
DPN5	18	72.95

The specific surface area of the prepared Mn/TiO_2 decreased with increasing manganese loading and calcination temperature. Due to the difference in the surface area of the metal and that of TiO_2, with increasing manganese loading, the surface area decreased as the metal may have covered the pores and the surface of TiO_2. To a larger degree, with increasing calcination temperature, catalyst surface area decreased due to sintering which was prevalent in catalysts calcined at 800°C. The sintering of the catalyst not only caused the pores to either collapse and expand but allowed the reaction of manganese with TiO_2 to form $MnTiO_3$ which changed the bulk structure of the catalyst.

In order to confirm the oxidation states of the Mn/TiO_2 catalysts, specifically for IPT350 which did not show any manganese peaks in the XRD diffractogram, XPS analysis was performed. Similar to the procedure performed on the Ag/TiO_2 catalysts, the Ti 2p, Mn 2p and C 1s core level XPS high-resolution spectra were recorded for the Mn/TiO_2 catalysts. The spectra were decomposed assuming Lorentzian-Gaussian line profiles with a Shirley function for background correction and binding energy shifts were adjusted using the C 1s level at 284.8 eV from adventitious carbon. Figure 3.10 shows the narrow scans of the Ti 2p and Mn 2p peaks for the different catalysts.

Table 3.6 summarizes the results from the peak fitting analysis of the Ti 2p and Mn 2p peak profiles of the prepared catalysts. The Ti 2p spectra was decomposed into Ti^{4+} and Ti^{3+} states corresponding to binding energies of 458.2 eV and 457.4 eV, respectively[7,8]. As expected, bulk chemical species of Ti found in all catalysts are in the Ti^{4+} state indicative of TiO_2 form. For the IP catalysts, significant fractions for the Ti^{3+} state were found. This was mainly due to the calcination step during the preparation of the catalysts which formed impurities and defects on TiO_2 resulting in Ti^{3+} chemical state. DPN catalysts showed only a very small fraction for the Ti^{3+} state.

The Mn 2p spectra was decomposed to fit Mn^0, Mn^{2+}, Mn^{3+}, and Mn^{4+} surface species based on the binding energy ranges of 638.6 to 639.6, 640.3 to 640.9, 641.3 to 642.1, and 642.2 to 643.2, respectively[12,15-17]. A broad shoulder was also present in the Mn $2p_{3/2}$ peak which was assigned to manganese nitrate at a binding energy range of 644.5 to 644.9. Decomposition of the Mn 2p spectra from peak fitting analysis showed multiple peaks indicating multiple oxidations states for manganese on the Mn/TiO_2 catalysts. The largest fraction of chemical species found were Mn^{4+} (MnO_2) for IPT350, Mn^{3+} (Mn_2O_3) for IPT600, Mn^{2+} ($MnTiO_3$) for IPT800, and a mixture of Mn^{2+} and Mn^{3+} (Mn_3O_4) for DPN. This matched with the XRD results for IPT600, IPT800 and DPN catalysts and also confirmed that IPT350 catalysts contained MnO_2.

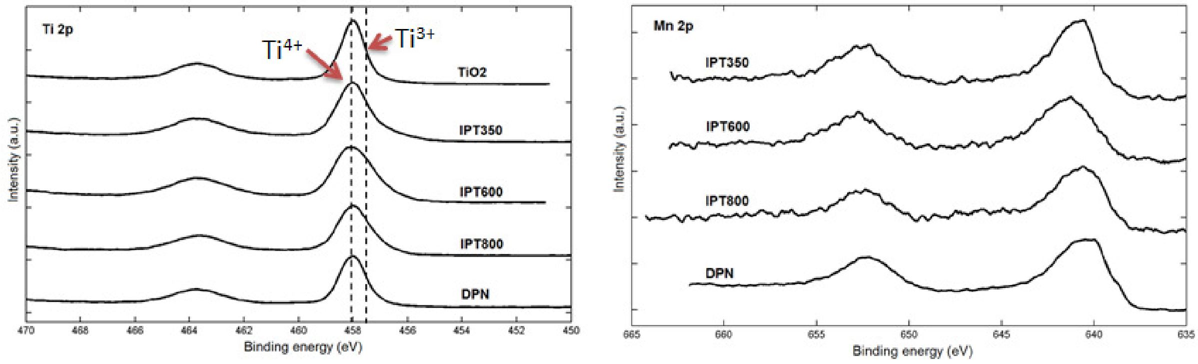

Figure 3.10. XPS high-resolution spectra of the Ti 2p and Mn 2p peak profiles for TiO_2 and Mn/TiO_2 catalysts

Table 3.6. Chemical binding energy properties of TiO_2 and Mn/TiO_2 catalysts determined by XPS

Catalyst	Chemical Species	Position (eV)	FWHM (eV)	Fraction	Chemical Species	Position (eV)	FWHM (eV)	Fraction
TiO_2	Ti^{4+}	458.2	1.13	1.0				
IP T350	Ti^{3+}	457.5	2.09	0.29	Mn^{3+}	641.3	1.14	0.30
	Ti^{4+}	458.3	1.22	0.71	Mn^{4+}	642.2	2.12	0.58
IP T600	Ti^{3+}	457.3	1.49	0.23	Mn^{2+}	640.3	1.58	0.21
	Ti^{4+}	458.3	1.40	0.77	Mn^{3+}	641.2	1.40	0.76
IP T800	Ti^{3+}	457.5	1.49	0.19	Mn^{2+}	640.7	2.27	0.49
	Ti^{4+}	458.3	1.28	0.81	Mn^{3+}	641.9	2.19	0.25
DPN	Ti^{3+}	457.3	1.48	0.07	Mn^{2+}	640.3	2.05	0.41
	Ti^{4+}	458.2	1.12	0.93	Mn^{3+}	641.3	1.97	0.27
					Mn^{4+}	642.6	2.77	0.18

Surface morphologies and active metal dispersion on the Mn/TiO_2 catalyst surface were analyzed by SEM-EDS. Figure 3.11 shows the SEM images of the Mn/TiO_2 prepared by IPT350, IPT600, IPT800, and DPN methods and the manganese metal distribution for the 5% Mn/TiO_2 on Figure 3.12. Small aggregate structures appeared on IPT350 catalysts which became larger in the IPT600 catalysts which could be from the agglomeration of the structures. In the IPT800 catalysts, the catalyst surface lacked the aggregate structures which could indicate that the structures were metal oxides on the catalyst surface as manganese in IPT800 was part of the bulk structure as $MnTiO_3$. DPN catalysts had irregular surface morphology compared to IP catalysts.

Elemental mapping of the catalysts (Fig. 3.12) showed that the highest surface concentration of manganese was found in the DPN catalysts. In DPN, as the metal was precipitated directly on TiO_2 and this would have formed a layer on the TiO_2 surface as compared to IP catalysts where the metal would be located on the surface as well as inside the pores of TiO_2. Among the catalysts, IPT800 showed the lowest metal concentration on the surface as manganese in IPT800 catalysts were part of the bulk structure rather than loaded on TiO_2.

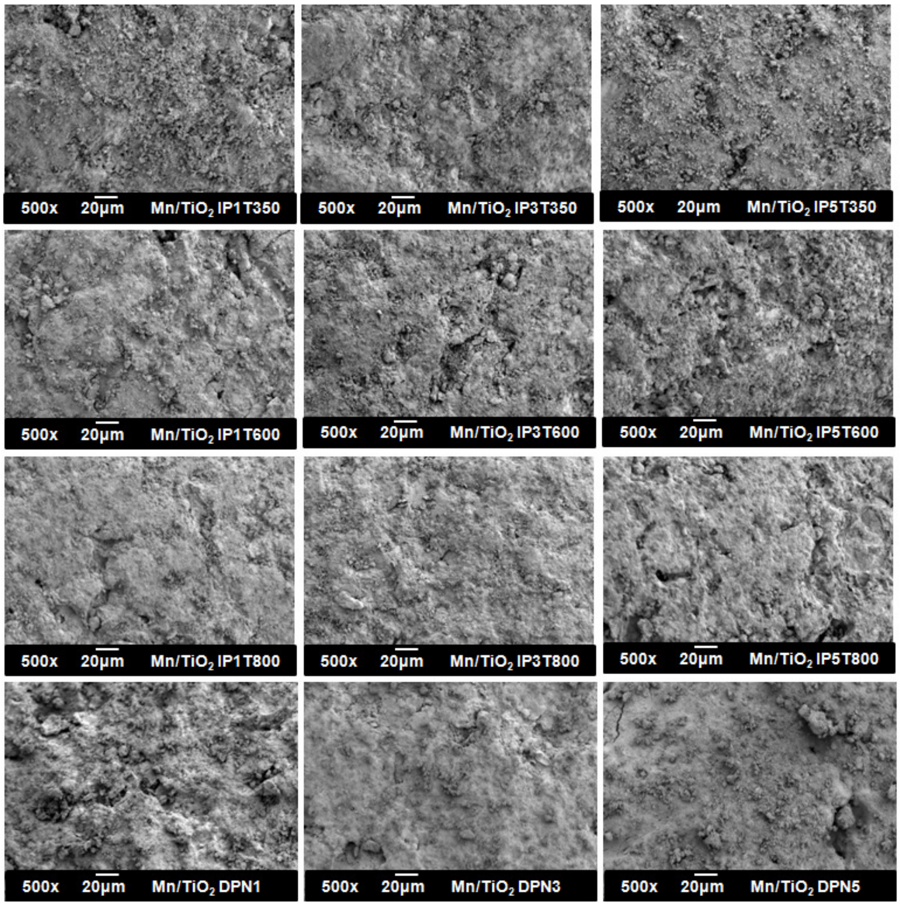

Figure 3.11. SEM images of the prepared Mn/TiO_2 catalysts

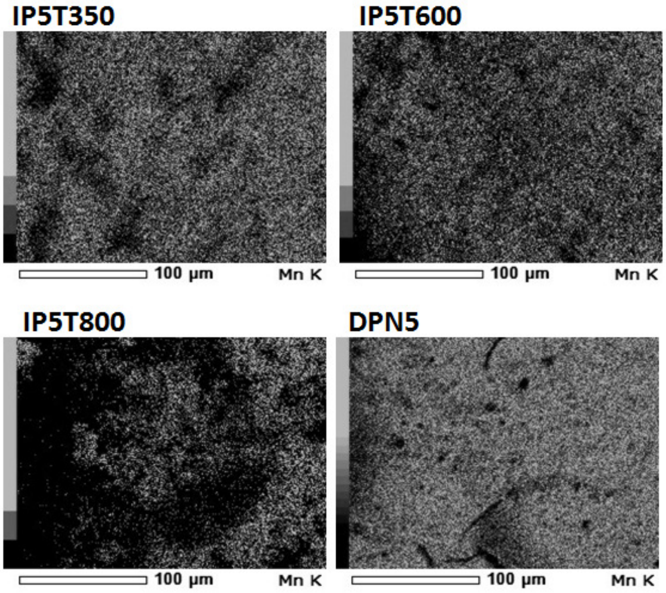

Figure 3.12. SEM-EDS digital mapping of Mn on the prepared 5% Mn/TiO_2 catalysts

3.2.3 Ag-Mn/TiO_2

Bulk crystal structure and size were determined by XRD and the diffractograms for 5% Ag-Mn/TiO_2 catalysts prepared by IP and DPN methods are presented in Figure 3.13. All prepared catalysts retained its anatase crystal structure and small peaks for Ag_2O (PDF# 43-0997) and MnO_2 (PDF# 50-0866) were found in DPN catalysts.

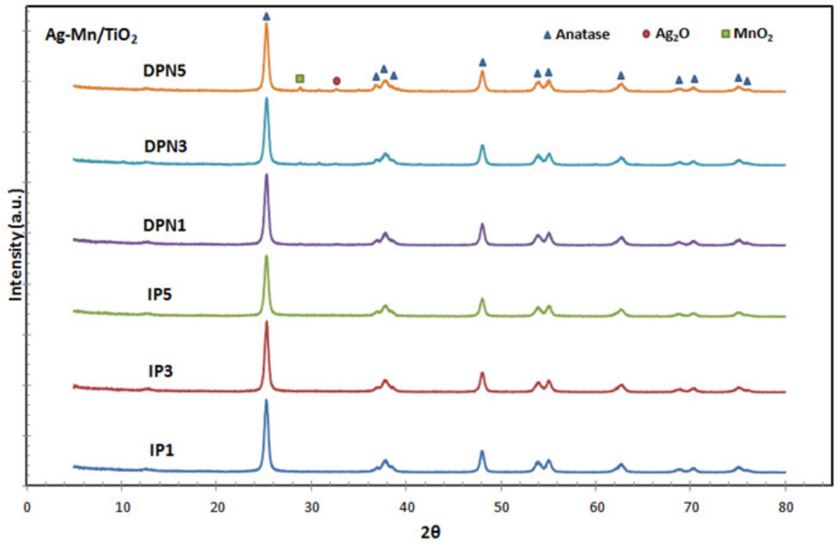

Figure 3.13. XRD diffractograms of Ag-Mn/TiO_2 prepared by IP and DPN method

Table 3.7. Summary of catalyst structural properties for TiO_2 and prepared Ag-Mn/TiO_2 catalysts

Catalyst	Crystal size, nm	Specific surface area, m^2/g
TiO_2	20	64.95
IP1	18	73.30
IP3	18	73.80
IP5	17	72.35
DPN1	17	74.62
DPN3	17	70.23
DPN5	18	67.45

Catalyst crystal size and specific surface area are summarized in Table 3.7. Anatase crystal size for the prepared catalysts ranged from 17 nm to 18 nm as compared to 20 nm in the base TiO_2. The specific surface area of the prepared Ag-Mn/TiO_2 increased from the base TiO_2 of 64.95 m^2/g to 72.35 m^2/g - 73.30 m^2/g in the IP catalysts and to 67.45 m^2/g - 74.62 m^2/g in the DPN catalysts. With increasing metal loading, catalyst surface area slightly decreased for the IP catalysts compared to DPN catalysts.

The chemical binding energy and the chemical state of the Ag-Mg/TiO_2 were investigated by XPS. Similar procedure was used and the Ti 2p, Ag 3d, Mn 2p, and C 1s core level XPS high-resolution spectra were recorded. The spectra were decomposed assuming Lorentzian-Gaussian line profiles with a Shirley function for background correction and binding energy shifts were adjusted using the C 1s level at 284.8 eV from adventitious carbon.

Figure 3.14 shows the narrow scans of the Ti 2p, Ag 3d, and Mn 2p peaks for the different catalysts and Table 3.8 summarizes the results from the peak fitting analysis from the narrow scans of the prepared catalysts. The Ti 2p spectra for all prepared catalysts showed only the peak for Ti^{4+} species at 458.2 eV for TiO_2 and 458.3 eV for IP and DPN catalysts. Analysis of the Ag 3d spectra for the IP catalyst showed one peak at 368.0 eV assigned to Ag^0 and for the DPN catalyst, resolution of the Ag 3d peak showed peaks at 367.6 eV for Ag^{1+} with a fraction of 0.92 and another at 366.5 eV for Ag^{3+} in a much smaller fraction of 0.08. Resolution of the Mn 2p peak spectra for the IP catalyst showed multiple peaks for Mn^{2+} at 640.9 eV, Mn^{3+} at 641.7 eV, and Mn^{4+} at 642.7 eV with fractions of 0.13, 0.30, and 0.37, respectively. Similarly, resolution of the Mn 2p peak for the DPN catalyst showed peaks for Mn^{2+} at 640.9 eV, Mn^{3+} at 641.8 eV, and Mn^{4+} at 642.6 eV with fractions of 0.18, 0.21, and 0.51, respectively.

From these results, it can be inferred that Ag-Mn/TiO_2 catalysts prepared by IP method is composed by metallic Ag and MnO_2 loaded on TiO_2, and for the catalysts prepared by DPN method, Ag_2O and MnO_2 loaded on TiO_2. Results for the DPN catalysts matched with those from XRD analysis and confirmed the oxidation state for the IP catalysts based from the preparation method.

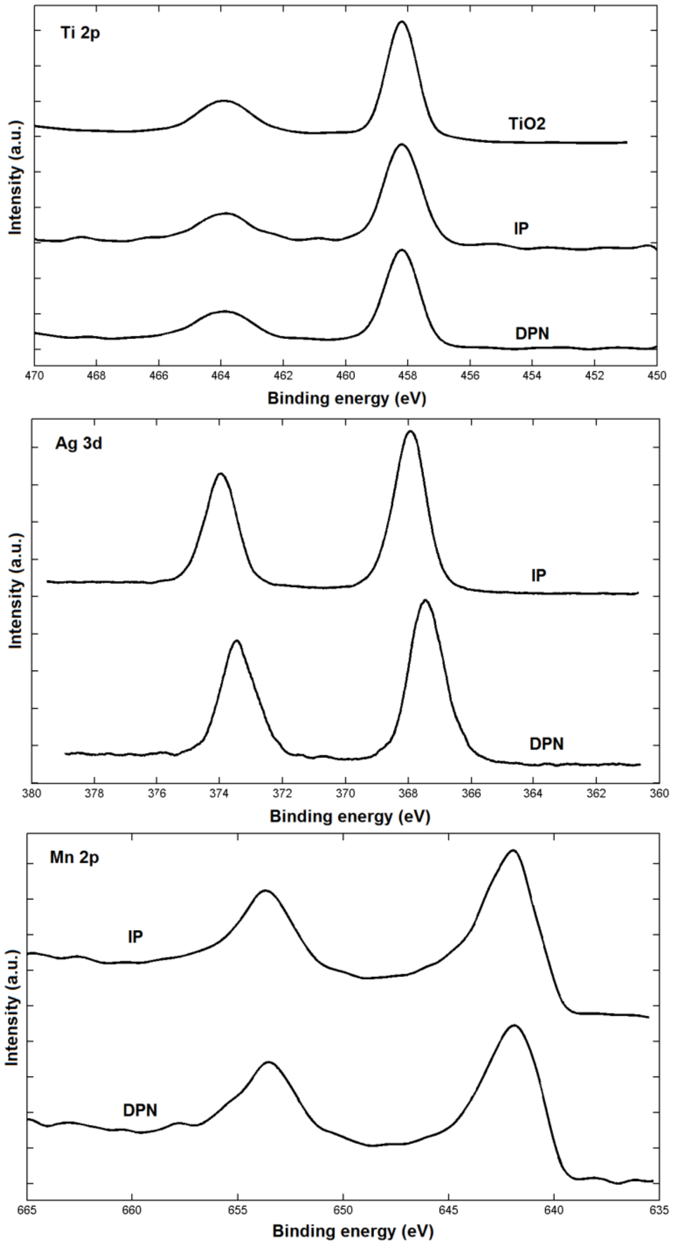

Figure 3.14. XPS high-resolution spectra of Ti 2p, Ag 3d, and Mn 2p peak profiles for TiO_2 and Ag-Mn/TiO_2 catalysts

Table 3.8. Chemical binding energy properties of TiO_2 and Ag-Mn/TiO_2 catalysts determined by XPS

Catalyst	TiO_2			IP			DPN		
Chemical Species	Position (eV)	FWHM (eV)	Fraction	Position (eV)	FWHM (eV)	Fraction	Position (eV)	FWHM (eV)	Fraction
Ti^{4+}	458.2	1.13	1.0	458.3	1.23	1.0	458.3	1.19	1.0
Ag^0	--	--	--	368.0	1.25	1.0	--	--	--
Ag^{1+}	--	--	--	--	--	--	367.6	1.25	0.92
Ag^{3+}	--	--	--	--	--	--	366.5	1.06	0.08
Mn^{2+}	--	--	--	640.9	1.06	0.13	640.9	1.06	0.18
Mn^{3+}	--	--	--	641.7	1.22	0.30	641.8	1.22	0.21
Mn^{4+}	--	--	--	642.7	1.71	0.37	642.6	2.34	0.51

Surface morphologies and active metal dispersion on the Ag-Mn/TiO_2 catalyst surface were analyzed by SEM-EDS. Figure 3.15 shows the SEM images of the catalysts prepared by IP and DPN method. Although the catalysts prepared by both methods showed particle agglomeration, it was found more prevalent in the IP catalyst rather than in the DPN catalysts and with increasing metal loading, particles became larger.

Figure 3.16 shows the elemental mapping of the Ag-Mn/TiO_2 catalysts prepared by IP and DPN method and surface concentration scans are also presented in Figure 3.17. Metal dispersion for Ti, Ag, and Mn as well as the overlay of these three metals are also presented in the figure. Metal dispersion on IP catalysts are relatively uniform throughout the surface of TiO_2. Surface concentration scan showed higher peaks for Ti than Ag and Mn indicating that the exposed surface was mainly Ti. In the DPN catalyst, Ag and Mn showed higher concentration on the surface than Ti. Based from the overlay image, Ag (blue) and Mn (green) mainly covered Ti (red) which can also be seen in the surface concentration scan. These results indicate that the metals in the IP catalyst are located not only on the surface but also inside the pores of the catalyst. The metals in the DPN catalyst, however, are located on the surface as it was precipitated on the TiO_2 surface.

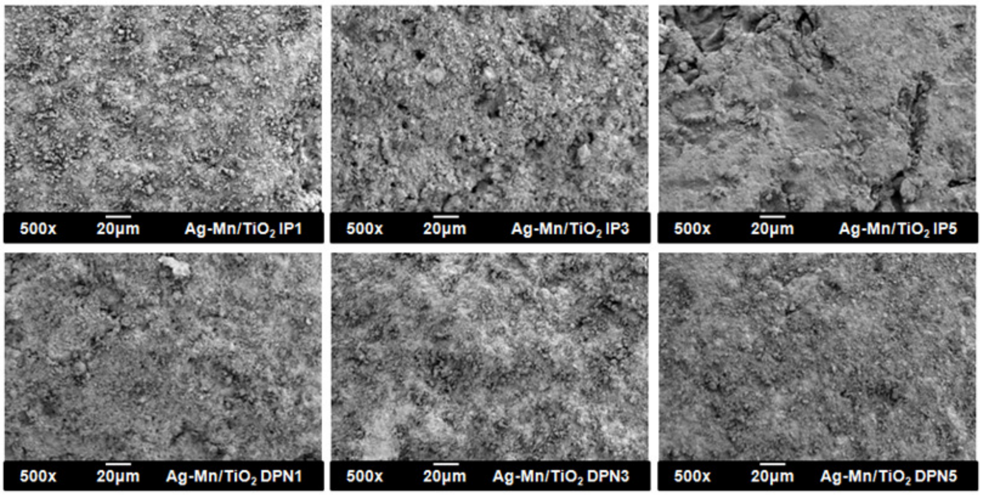

Figure 3.15. SEM images of the prepared Ag-Mn/TiO_2 catalysts

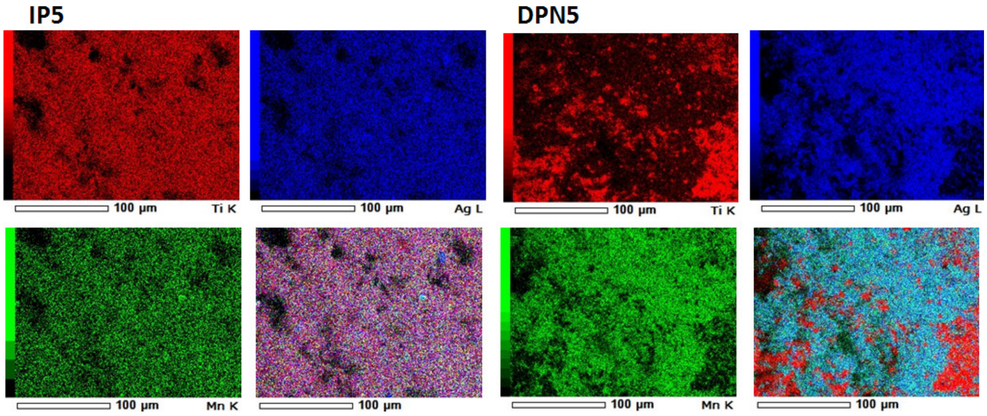

Figure 3.16. SEM-EDS digital mapping of Ti, Ag, Mn, and the metal overlay of the prepared Ag-Mn/TiO_2 catalysts

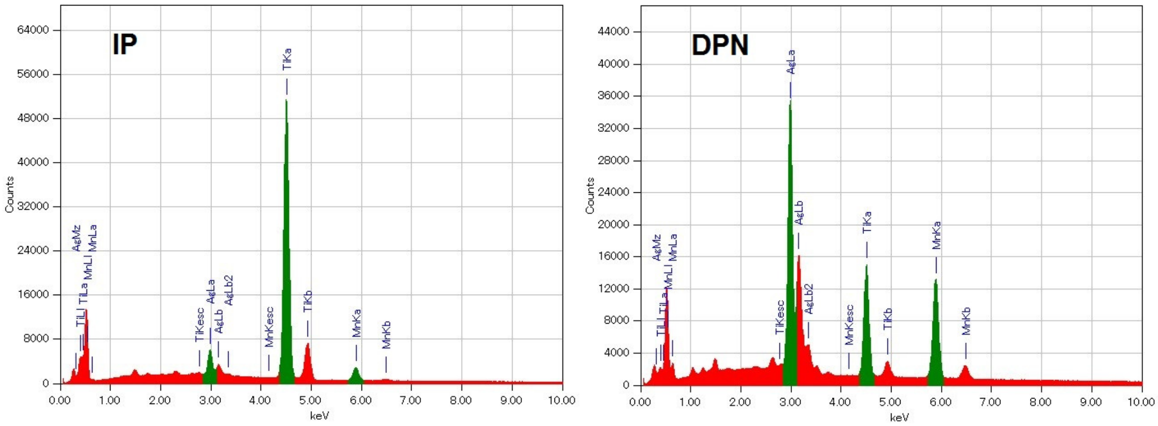

Figure 3.17. SEM-EDS surface concentration scan for Ag-Mn/TiO_2

3.3 Summary of results

The catalysts prepared for this study were Ag/TiO_2, Mn/TiO_2, and $Ag\text{-}Mn/TiO_2$ and were prepared by impregnation method and deposition-precipitation methods. In the impregnation method, electrostatic forces such as capillary action allowed the metal precursor to disperse on the surface and into the pores of the catalyst. In deposition-precipitation methods, the metal was directly precipitated on the support to provide higher metal surface concentration.

Based from catalyst characterization results, the catalyst structural and chemical properties highly depend on their preparation method. The catalysts retained its anatase crystal structure from the base TiO_2 except for Mn/TiO_2 catalysts that were calcined at 800^{o}C where rutile crystal structure was also present. Anatase crystal size also remain relatively similar to the base TiO_2, again, except for Mn/TiO_2 calcined at 800^{o}C where the transition from anatase to rutile phase disrupted the crystal structure and consequently the crystal size.

The catalyst specific surface area decreased with increasing metal loading and calcination temperature. The degree of change in the specific surface area depended on the preparation method. Catalysts prepared by impregnation method showed higher decrease in surface area than those prepared by deposition-precipitation methods. Specifically, Mn/TiO_2 calcined at 800^{o}C showed a large decrease in surface area which was attributed to the formation of $MnTiO_3$ where the metal was not loaded on the TiO_2 support but as part of the bulk structure of the catalyst.

XPS analysis was performed to determine the chemical binding energy of the catalysts and correspondingly, the metal oxidation states of the loaded metals on TiO_2. Various metal oxidation states were obtained for Ag/TiO_2, Mn/TiO_2, and $Ag\text{-}Mn/TiO_2$. A summary for the bulk metal oxidation state and its fraction in the catalyst are presented in Table 3.9.

Surface morphology and metal dispersion analysis by SEM-EDS showed that the prepared catalysts showed small aggregate structures on the catalysts surface. This was more predominantly found in impregnated catalysts as compared to catalysts prepared by deposition-precipitation methods. With increasing metal loading and calcination temperature, particle further agglomerated and increased in size. Metal dispersion was relatively uniform among catalysts prepared by deposition-precipitation methods and to a smaller extent, in the catalysts prepared by impregnation method. Surface metal density was higher in the deposited-precipitated catalysts than in impregnated catalysts as the metals in impregnated catalysts was assumed to be located also within the pores of the support rather than only on the surface. All catalysts except for Mn/TiO_2 calcined at 800^{o}C showed similar surface morphologies and metal dispersion. The differences observed in Mn/TiO_2 IP T800 was attributed to the formation of $MnTiO_3$ which included the metal in the bulk crystal structure rather than being loaded onto the support.

Table 3.9. Summary of metal oxidation states of the prepared catalysts

Catalyst	Preparation Method	Bulk metal oxidation state	Metal state fraction
Ag/TiO_2	IP	Ag/TiO_2	1.0
	DPN	Ag_2O/TiO_2	0.78
	DPH	AgO/TiO_2	0.76
Mn/TiO_2	IP T350	MnO_2/TiO_2	0.58
	IP T600	Mn_2O_3/TiO_2	0.76
	IP T800	$MnTiO_3$	0.49
	DPN	Mn_3O_4/TiO_2	0.68[a]
$Ag\text{-}Mn/TiO_2$	IP	$Ag\text{-}MnO_2/TiO_2$	1.0/0.37[b]
	DPN	$Ag_2O\text{-}MnO_2/TiO_2$	0.92/0.51 [b]

[a] combined fraction for Mn^{2+} and Mn^{3+} species

[b] first fraction is for Ag followed by Mn fraction

Chapter References

[1] **Sandoval, A., Aguilar, A., Louis C., Traverse, A., Zanella, R.** *Bimetallic Au-Ag/TiO_2 catalyst prepared by deposition-precipitation: High activity and stability in CO oxidation.* Journal of Catalysis 281 (2011) 40-49

[2] **Zanella, R., Delannoy, L., Louis, C.** *Mechanism of gold precursors onto TiO_2 during the preparation by cation adsorption and deposition-precipitation with NaOH and urea.* Applied Catalysis A: General 291 (2005) 62-72

[3] **Moon, J., Awano, M., Takagi, H., Fujishiro, Y.** *Synthesis of nanocrystalline manganese oxide powders: Influence of hydrogen peroxide on particle characteristics.* Journals of Materials Research 14 (1999) 4594-4601

[4] **You, X., Chen, F., Zhang, J. Anpo, M.** *A novel deposition precipitation method for preparation of Ag-loaded titanium dioxide.* Catalysis Letters, Vol. 102, Nos. 3-4 (2005)

[5] **Zhang, J., Xiao, L., Cong, Ye.** *Preparation and Characterization of multi-functional titanium dioxide photocatalysts.* Topics in Catalysis Vol. 47, Nos. 3-4 (2008) 122-130

[6] **Stern, K.H.** *High temperature properties and decomposition of inorganic salts. Part 3. Nitrates and nitrites.* Journal of Physical Chemistry Reference Data 1 (1972) 747-772

[7] **Madhu Kumar P., Badrinarayanan S., Sastry M.** *Nanocrystalline TiO_2 studied by optical, FTIR and X-ray photoelectron spectroscopy: correlation to presence of surface states.* Thin Solid Films 358 (2000) 122-130

[8] **Kuo Y.L., Su T.L., Chuang K.J., Chen H.W., Kung F.C.** *Preparation of platinum- and silver-incorporated TiO_2 coatings in thin-film photoreactor for the photocatalytic decomposition of o-cresol.* Environmental Technology 32 (2011) 1799-1806

[9] **Hoflund G.B., Hazos Z.F., Salaita G.N.** *Surface characterization study of Ag, AgO, and Ag_2O using x-ray photoelectron spectroscopy and electron energy-loss spectroscopy.* Physical Review B, 62 (2000) 11126-11133

[10] **Weaver J.F., Hoflund G.B.** *Surface characterization study of the thermal decomposition of AgO.* The Journal of Physical Chemistry 98 (1994) 8519-8524

[11] **Feng N., Wang Q., Zheng A., Zhang Z., Fan J., Liu S.B., Amoereux J.P., Deng F.** *Understanding the high photocatalytic activity of (B, Ag)-codoped TiO_2 under solar-light irradiation with XPS, solid-state NMR, and DFT calculations.* Journal of American Chemical Society 135 (2013) 1607-1616

[12] **Ettireddy, P.R., Ettireddy, N., Mamedov, S., Boolchand, P., and Smirniotis, P.G.** *Surface characterization studies of TiO_2 supported manganese oxide catalysts for low temperature SCR of NO with NH_3.* Applied Catalysis B: Environmental 76 (2007) 123-134.

[13] **Zhou, G.W. and Kang, Y.S.** *Synthesis and structural properties of manganese titanate $MnTiO_3$ nanoparticle.* Materials Science and Engineering *C* 24 (2004) 71-74.

[14] **Hanaor, D.A.H. and Sorell, C.C.** *Review of the anatase to rutile phase transformation.* Journal of Material Science 46 (2011) 855-875.

[15] **Biesinger, M.C., Payne, B.P., Grosvenor, A.P., Lau, L.W.M., Gerson, A.R., and Smart, R.St.C.** *Resolving surface chemical states in XPS analysis of first row transition metals, oxides, and hydroxides: Cr, Mn, Fe, Co and Ni.* Applied Surface Science 257 (2011) 2717-2730.

[16] **Tang, W.X., Liu, H.D., Wu, X.F., and Chen, Y.F.** *Higher oxidation state responsible for ozone decomposition at room temperature over manganese and cobalt oxides: effect of calcination temperature.* Ozone: Science & Engineering 36 (2014) 502-512.

[17] **Wang, M., Zhang, P., Li, J., and Jiang, C.** *The effects of Mn loading on the structure and ozone decomposition activity of MnOx supported on activated carbon.* Chinese Journal of Catalysis 35 (2014) 335-341.

Chapter 4

CHARACTERIZATION OF DIELECTRIC BARRIER DISCHARGE REACTOR

Dielectric barrier discharge is generated between two metallic electrodes with at least one electrode covered by a dielectric barrier. The discharge can be generated by applying AC high voltage across the electrodes and the dielectric barrier limits the discharge current, preventing arc discharge and ensures that a stable non-equilibrium plasma can be generated even under atmospheric pressure. Discharge characteristics depend on various conditions such as power supply, electrode and reactor configuration, dielectric materials, and operating gases. This chapter discusses the effect of reactor length, TiO_2 catalyst loading, and TiO_2 catalyst placement on the discharge characteristics of the dielectric barrier discharge reactor used in this study.

4.1 Dielectric barrier discharge reactor

The non-thermal plasma reactor used for this study was a tubular dielectric barrier discharge (DBD) reactor and is presented in Figure 4.1. The reactor was made of a quartz tube with an inside diameter of 13 nm, length of 200 mm and a thickness of 1 mm. A stainless steel rod with a diameter of 9 mm was fixed along the center of the quartz tube to function as the high-voltage electrode. Silver paint was coated outside the reactor to function as the ground electrode. The length of the coating of the silver paint determined the effective length of the reactor for non-thermal plasma discharge. For the plasma driven catalysis system, catalysts were placed within the quartz tube along the effective length of the reactor.

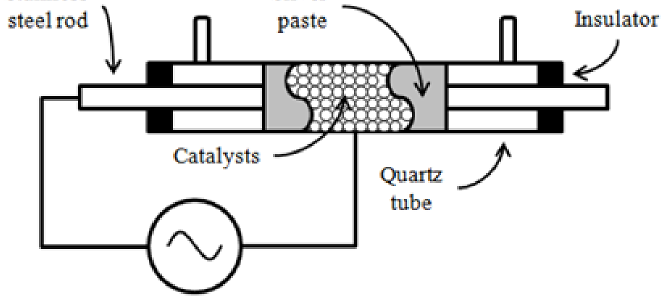

Figure 4.1. Non-thermal plasma dielectric barrier discharge reactor

Non-thermal plasma was generated within the DBD reactor by passing low-current high-voltage across the electrodes of the reactor. The power was supplied by a neon transformer (LECIP

Co., Ltd., 100-A-15HCS) connected to a volt slider and a 50 Hz AC power supply. The applied voltage, V, was measured with a 1000:1 high voltage probe (Agilent Technologies, N2771B) and the charge, Q (time-integrated current), was determined by measuring the voltage across a 100 nF capacitor connected in series with the ground line of the reactor. The signals were recorded by an oscilloscope (GW Instek, GDS-1072A-U) by averaging 64 scans. The input voltage to the reactor was varied by changing the volt slider setting and monitoring the oscilloscope reading.

4.2 Electrical characterization

4.2.1 Energy consumed per cycle and power calculations

The voltage-charge V-Q Lissajous figure method[1,2] was used to determine the average discharge power generated from the DBD reactor. Signals for the Lissajous figure was obtained using an oscilloscope and a high voltage probe. The transported charge was measured by multiplying the voltage along the capacitor connected in series with the reactor by its known capacitance. This charge, Q, and the voltage along the reactor, V, were plotted to obtain the Lissajous figure.

A sample plot of an idealized Lissajous figure is presented in Fig. 4.2. From this figure, the maximum voltage V_{max}, minimum voltage at which ignition occurs V_{min}, the two gradients $dQ/dV = C$ and $dQ/dV = C_d$ which represents the total capacitance of the reactor and the dielectric, respectively, and the electric energy consumed per voltage cycle E_{el} represented by the area enclosed by the diagram could be determined[1].

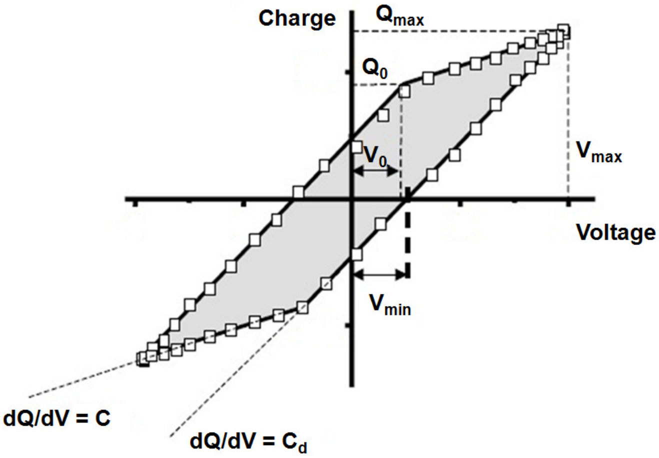

Figure 4.2. Idealized V-Q Lissajous figure

The energy consumed in the DBD reactor per voltage cycle E_{el} is given by Eq. 4.1, where $V(t)$ is the applied voltage, $i(t)$ is the current flowing through the DBD reactor and T is the time period. If

C_m is the capacitance of the measuring capacitor the current flowing through it could be expressed as in Eq. 4.2, where q is the transported charge and V_C is the voltage across the measuring capacitor. Hence, the energy consumed in the DBD reactor per voltage cycle can be measured by Eq. 4.3.

$$E_{el} = 2\int_0^{T/2} V(t)\,i(t)\,dt \qquad \text{(Eq. 4.1)}$$

$$i(t) = \frac{dq}{dt} = \frac{C_m dV_C}{dt} \qquad \text{(Eq. 4.2)}$$

$$E_{el} = 2\int_0^{T/2} V(t)\,dq(t)$$
$$E_{el} = 2\int_0^{T/2} V(t)\,Cdv_C(t) \qquad \text{(Eq. 4.3)}$$

Equation 4.3 shows that the energy consumed in the DBD reactor per voltage cycle can be measured by solving for the area of the Lissajous figure. The power consumed in the DBD reactor P_{dis} then can be easily calculated by multiplying the electrical energy consumed in the reactor by the frequency f of the applied voltage (Eq. 4.4). The specific input energy (SIE) can then calculated by dividing the discharge power with the gas flow rate (Eq. 4.5).

$$P_{dis} = f\,E_{el} \qquad \text{(Eq. 4.4)}$$

$$\text{Specific input energy}\,(J/L) = \frac{\text{discharge power }(W)}{\text{gas flow rate }(L/\text{min})}x60 \qquad \text{(Eq. 4.5)}$$

To minimize signal noise from the oscilloscope, a butterworth filter was applied on the oscilloscope data. The butterworth filter is a type of signal processing filter used to obtain a flat frequency response. The filter reject data points from unwanted frequencies at the same time have uniform sensitivity for the wanted frequencies. After the filter was applied to the data, the area of the enclosed region was solved using the convex hull method. The convex hull method envelops the minimal convex set of points in the Euclidean plane. This could be visualized by stretching a rubber band around all given values in the data set. Both data processing procedures were performed using commercially available software (MATLAB). Figure 4.3 shows a sample of the pre-processed data and the post-processed data as well as the calculated area of the enclosed region.

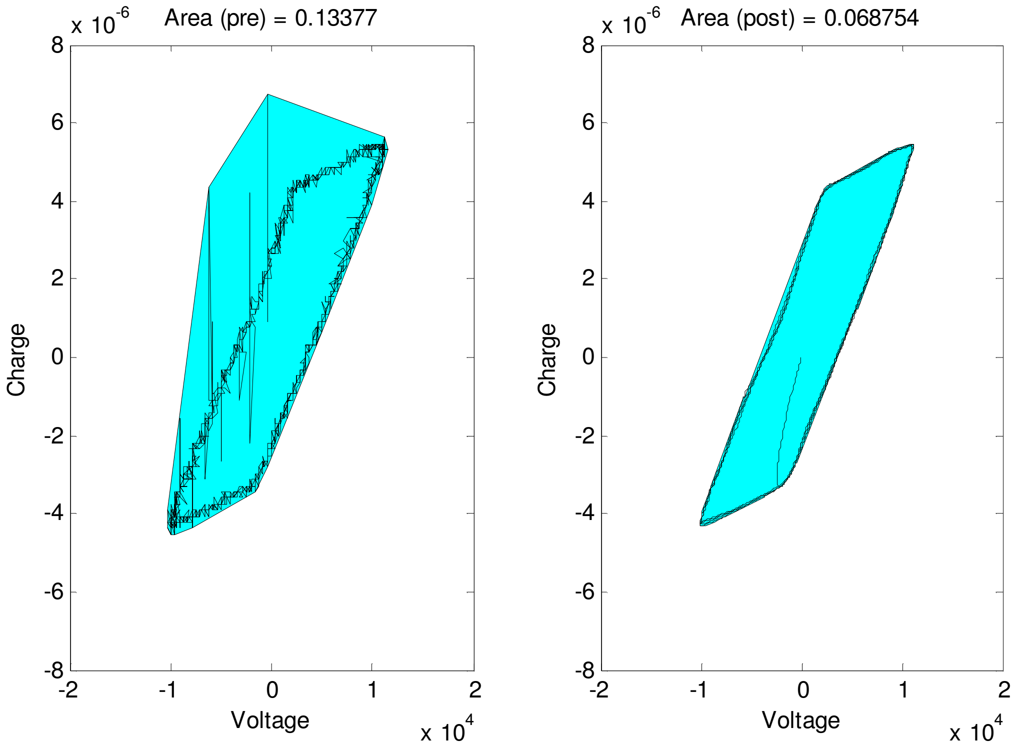

Figure 4.3. Sample *V-Q* diagrams for pre-processed and post-processed data

4.2.2 Electron density and electron temperature calculations

The electron density within the plasma discharge can be calculated from the plasma current density, J (A m^{-2}), and the electron drift velocity, v_{drift} (m s^{-1}), using Eq. 4.6[3,4] where e in this equation is the electron elementary charge (1.6028 x 10^{19} C). The plasma current density (Eq. 4.7) can be calculated by dividing the discharge power, P (W), with the discharge voltage, V_{dis} (V), and the electrode surface area, S (m^2). Since the reactor used is a tubular concentric reactor, the log mean average area of the electrodes were used for the calculation. The discharge voltage (Eq. 4.8) could be calculated by obtaining the minimum voltage required to initiate discharge, V_{min} (V), and the gap capacitance (Eq. 4.9), C_g (F), and the dielectric capacitance, C_d (F), from the *V-Q* diagram. The electron drift velocity was obtained from literature[5] and was dependent on the reduced electric field (Eq. 4.10), E/p (V m N^{-1}), which was calculated by dividing the discharge volume with the discharge gap, g (m), and the working pressure, p (Pa). The electron temperature, T_e (eV), was estimated using Eq. 4.11[3] where m_e is the mass of electron (9.1094 x10^{-31} kg).

$$n_e = \frac{J}{e v_{drift}} \qquad \text{(Eq. 4.6)}$$

$$J = \frac{P}{V_{dis} S} \qquad \text{(Eq. 4.7)}$$

$$V_{dis} = V_{\min} \frac{1}{1 + C_g / C_d} \qquad \text{(Eq. 4.8)}$$

$$\frac{1}{C} = \frac{1}{C_g} + \frac{1}{C_d} \qquad \text{(Eq. 4.9)}$$

$$\frac{E}{p} = \frac{V_{dis}}{g\,p} \qquad \text{(Eq. 4.10)}$$

$$T_e = \frac{1}{2} m_e v_{drift}^2 \qquad \text{(Eq. 4.11)}$$

4.3 Experimental set-up

Figure 4.4 shows experimental set-up used for this part of the study. Synthetic air was fed into the reactor at a flow rate of 550 mL/min at standard atmospheric conditions. Non-thermal plasma was generated by varying the applied voltage supplied to the reactor. At each voltage setting, the voltage readings across the reactor and the capacitor attached in series with the reactor were recorded by the oscilloscope by averaging 64 scans and effluent concentrations of ozone and nitrogen oxides were analyzed using gas detection tube system (Ozone 182SA&B, Nitrogen oxides 175SA&SH, Nitrogen dioxide 117SA&SB; Kitagawa Komyo Rikagaku Kogyo).

Experiments on the effect of reactor length, TiO_2 catalyst loading, and reactor configuration to the discharge characteristics of the DBD reactor were performed. The reactor length was varied by changing the length of the silver paint coated on outside of the quartz tube and reactor configuration by changing the location of the TiO_2 catalyst within the reactor. The TiO_2 catalyst were placed either within the discharge region for a plasma driven catalysis (PDC) system or after the discharge region for a plasma assisted catalysis (PAC) system. Reactor configurations are shown in Figure 4.5 and experiment parameters are summarized in Table 4.1.

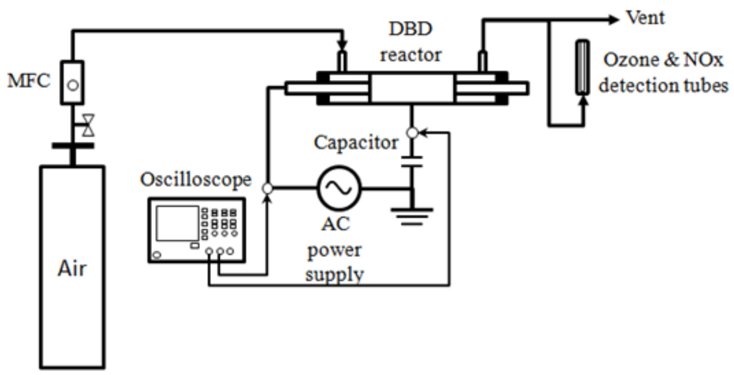

Figure 4.4. Experimental set-up for DBD reactor characterization experiments

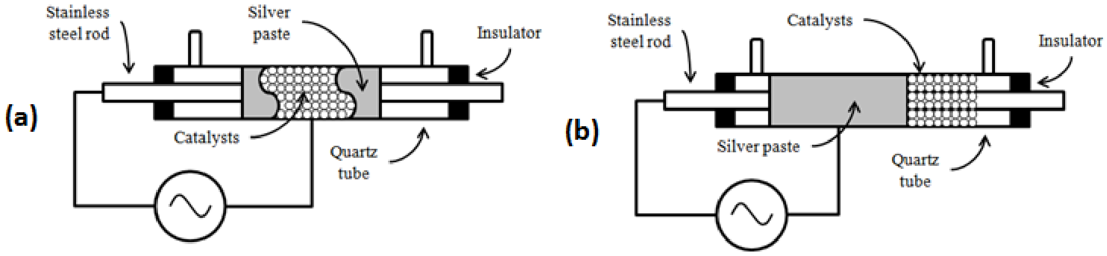

Figure 4.5. Reactor configuration for (a) plasma driven catalysis and (b) plasma assisted catalysis systems

Table 4. 1. Summary of experiment parameters

Parameter	Conditions	Values
Reactor length, L		2.5 cm
		5.0 cm
		7.5 cm
TiO_2 loading, wt	L = 5.0 cm	0.5 g
		1.0 g
		1.5 g
		2.0 g
Reactor configuration	L = 5.0 cm;	PDC
	wt = 1.0 g	PAC

4.4 Influence of reactor parameters to electrical discharge characteristics

4.4.1 Discharge power

Figure 4.6 shows the *V-Q* diagrams for the DBD reactors with effective lengths of 2.5 cm, 5.0 cm, and 7.5 cm at varying applied voltage values. It can be seen from the figures that the magnitude for the accumulated charge increased with increasing reactor length at the same applied voltage values. The larger gradient on the *V-Q* diagram representing the equivalent capacitance of the dielectric barrier also increases. The difference in the capacitances of the reactors is caused by the difference in the amount of accumulated charges due to the change in the area of the electrode caused by the increase in its length.

The effect of the reactor length to the discharge power is presented in Fig. 4.7. The discharge power was calculated by solving the area of the *V-Q* diagram which represented the total electrical energy consumed per voltage cycle and then was multiplied with the frequency of the applied voltage which was 50 Hz. Results showed that with increasing applied voltage, the discharge power increased linearly. Also, the increase in reactor length which effectively increased the discharge volume resulted in higher values for the discharge power.

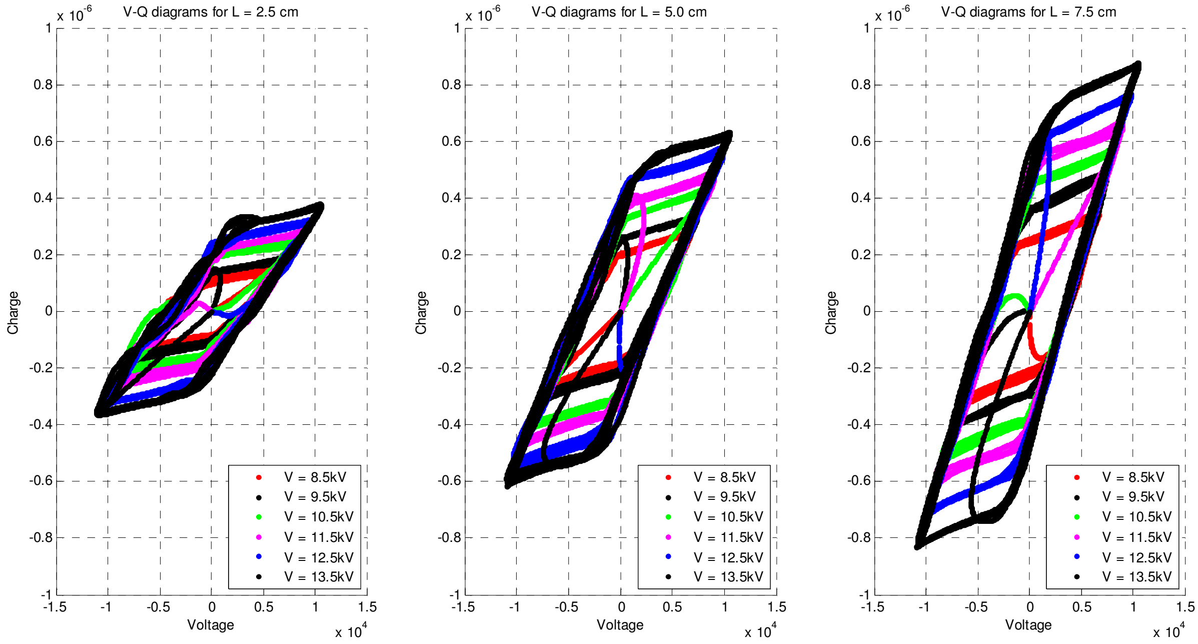

Figure 4.6. *V-Q* diagrams for reactor lengths of 2.5, 5.0, and 7.5 cm

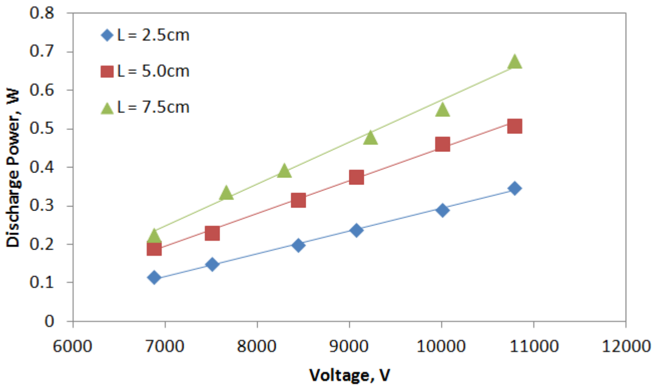

Figure 4.7. Effect of reactor length on the discharge power in the DBD reactor

The effect of TiO_2 loading amount (wt = 0.5 g, 1.0 g, 1.5 g, and 2.0g) on the *V-Q* diagram characteristics are presented in Fig. 4.8. It can be seen from the figure that as the TiO_2 loading amount increased, the shape of the *V-Q* diagram deviates from an ideal parallelogram. The point where the gradients representing the total capacitance of the reactor which included the dielectric and the discharge gap (smaller gradient) and the capacitance of the dielectric (larger gradient) change became rounded rather than having a sharp change as were seen in Fig 4.6 where TiO_2 catalysts were not present in the reactor.

The effect of TiO_2 loading on the discharge power is presented in Fig. 4.9. Results showed that with increasing TiO_2 loading at the same range of applied voltages, the discharge power decreased. The addition of TiO_2 within the reactor reduced the discharge gap between the electrode and dielectric as well as changed the overall capacitance of the reactor and its characteristics in terms of its capability in transporting charge and initiating plasma discharge. Plasma discharge occurs in the reactor when the applied voltage reaches the breakdown value of the reactor which includes the dielectric and the discharge gap. By placing catalysts within the discharge region, this reduced the discharge gap and the voltage required to initiate plasma discharge, thus resulting in lower values for the discharge power. This is also referred to as the packed-bed effect.

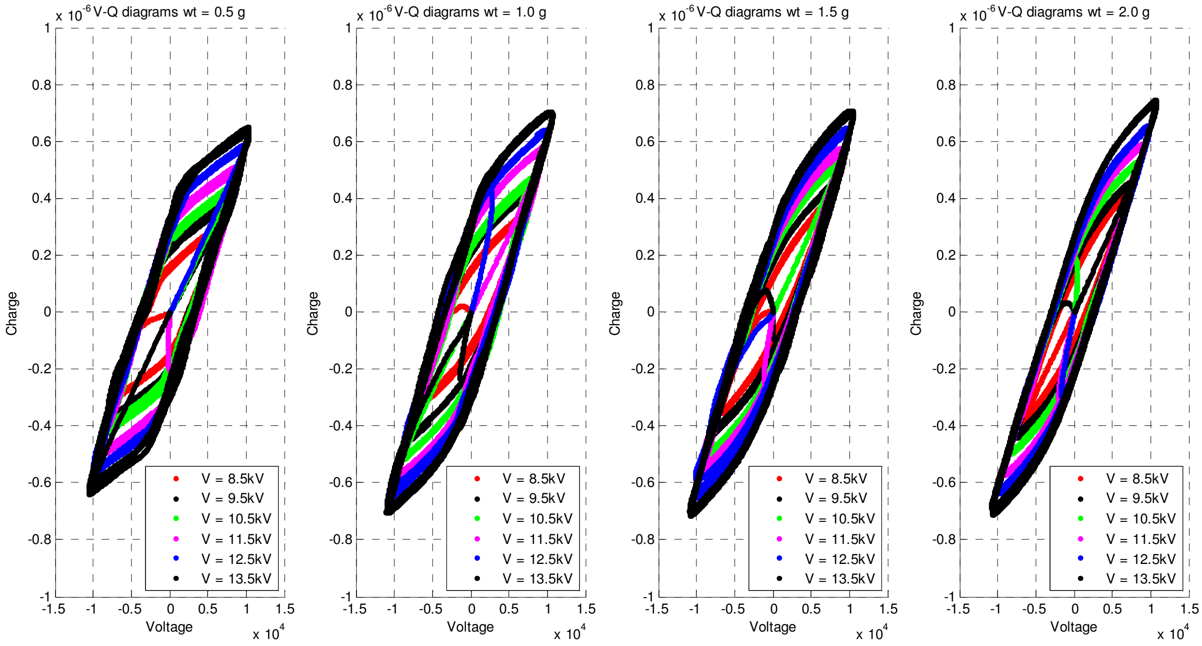

Figure 4.8. ***V-Q*** **diagrams for TiO_2 loadings of 0.5, 1.0, 1.5, 2.0 g at L = 5.0 cm**

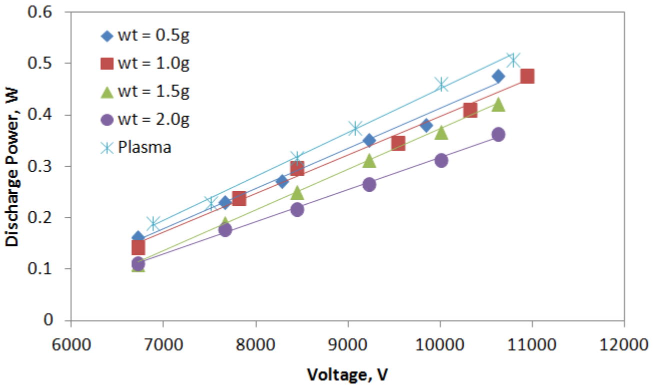

Figure 4.9. Effect of TiO_2 loading on the discharge power in the DBD reactor

The effect of reactor configuration (PDC and PAC) on the *V*-*Q* diagram characteristics are presented in Fig. 4.10. Aside from the rounding of the edges of the *V*-*Q* diagram for the PDC configuration, similar gradients (capacitances) were observed from both configurations. But what is interesting is that the discharge power observed (Fig. 4.11) for the PAC configuration is higher than the discharge power for the reactor without catalysts at higher applied voltages. It was expected that the discharge power for the PAC reactor would be similar to that of a plasma alone system. However, the catalysts were placed just outside of the edge of the effective length of the discharge region and this could have affected the discharge characteristics as discharges could have occurred not only along the discharge region and also concentrated at the edge where catalysts were located as well.

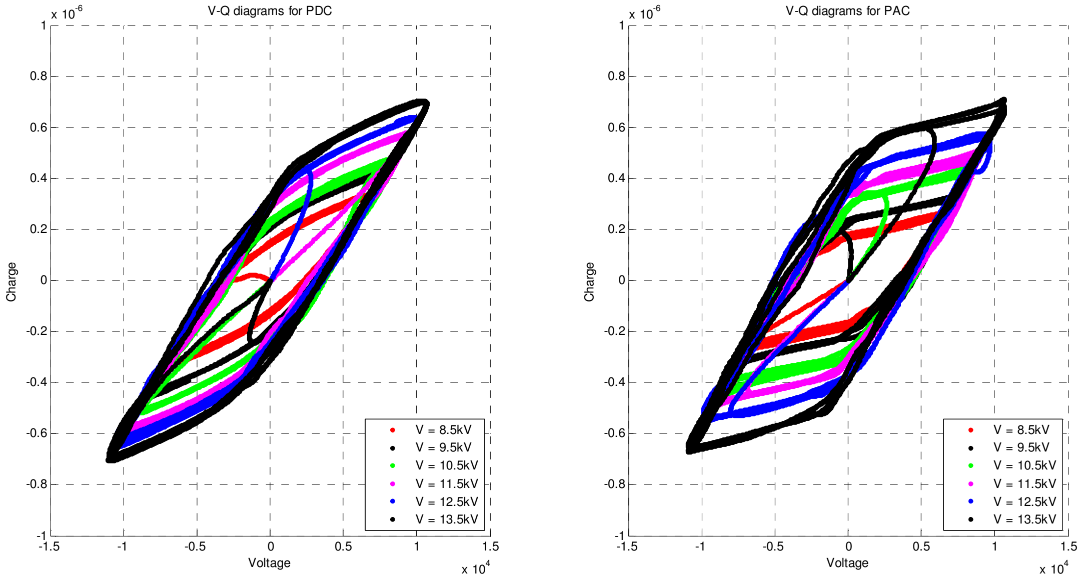

Figure 4.10. *V*-*Q* diagrams for PDC and PAC reactor configurations at L = 5.0 cm and TiO_2 catalyst wt = 1.0 g

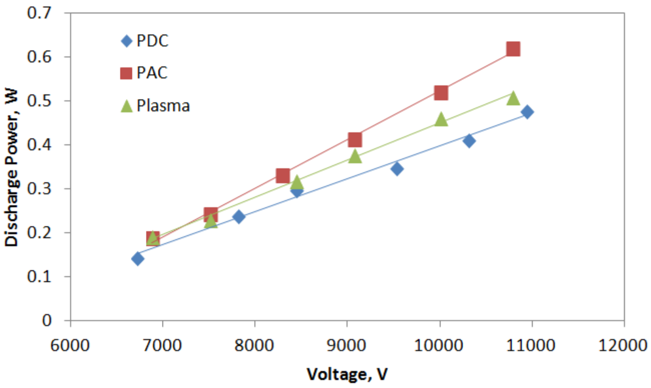

Figure 4.11. Effect of reactor configuration on the discharge power in the DBD reactor

4.4.2 Electron density and electron temperature

The effect of reactor parameters on electron density are presented in Fig. 4.12 for the reactor length, Fig. 4.13 for TiO_2 loading, and on Fig. 4.14 for reactor configuration. Regardless of the reactor condition, electron density increases with applied voltage. When the reactor length was increase from 2.5 cm to 5.0 cm, the electron density increase. However, further increase in reactor length to 7.5cm presented the same values for electron density. There was a significant change between the dielectric capacitances when the reactor length was increased from 2.5 cm (0.6234 F) to 5.0 cm (1.0505 F) and to 7.5 cm (1.4732 F). This resulted in having different values for the minimum voltage required to initiate discharge and consequently, the discharge voltage, reduced electric field, electron drift velocity, and current density which affected the electron density in the gas discharge.

Upon introduction of the TiO_2 catalysts within the discharge region, higher values for electron density were obtained using the same range for applied voltages. By introducing TiO_2 in the discharge region, this changes the gap capacitance which increased with increasing TiO_2 loading. This resulted in higher current densities and lower drift velocities which increased the electron density within the discharge. In terms of reactor configuration, the PAC system showed similar values for electron density with air plasma alone with the PDC system showing higher electron density values because of the presence of TiO_2 within the discharge region.

The effect of reactor parameters on electron temperature are presented on Table 4.2. The electron temperature were estimated based on air electron drift velocity values found in literature[5]. Electron drift velocity is dependent on the reduced electric field which is a function of the minimum voltage required to initiate discharge, and gap and dielectric capacitances. Based from the calculations performed, with increasing reactor length, electron temperature increase and by increasing the catalyst loading, electron temperature decreases. Electron temperature results from electron impact reaction and their respective kinetic energy. By having a larger discharge volume, electron impact reactions could readily occur thus increasing the electron temperature. But by reducing the discharge volume upon introduction of catalysts, this effectively reduces electron temperature.

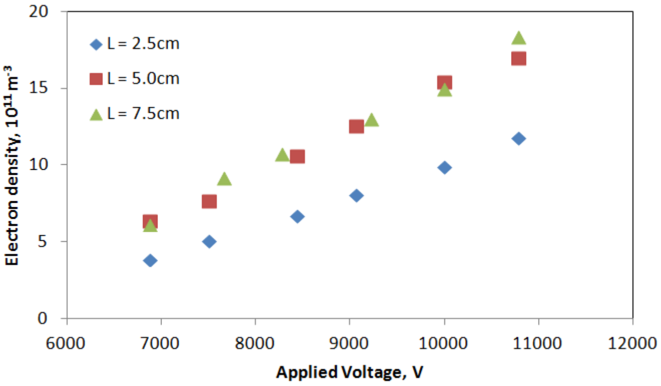

Figure 4.12. Effect of reactor length on electron density

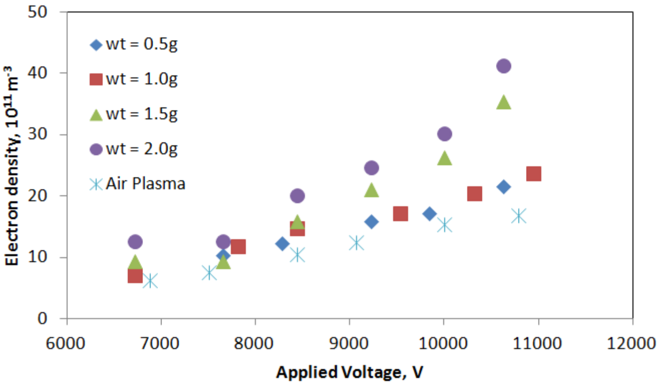

Figure 4.13. Effect of TiO_2 loading on electron density

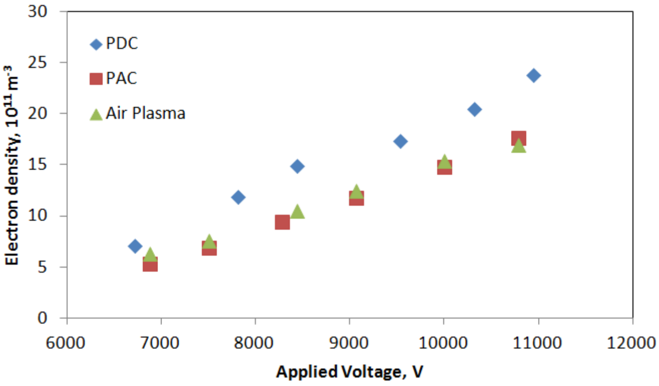

Figure 4.14. Effect of reactor configuration on electron density

Table 4. 2. Effect of reactor conditions on electron temperature

Parameter	Conditions	Values	Applied Voltage, V	T_e, eV
Reactor length, L		2.5 cm	10 781	2.48
		5.0 cm	10 781	2.52
		7.5 cm	10 781	2.98
TiO_2 loading, wt	L = 5.0 cm	0.5 g	10 625	1.95
		1.0 g	10 938	1.81
		1.5 g	10 625	1.16
		2.0 g	10 625	0.89
Reactor configuration	L = 5.0 cm;	PDC	10 938	1.81
	wt = 1.0 g	PAC	10 781	2.87

4.5 Influence of reactor parameters to effluent gas composition

Ozone generation efficiency is usually used as a good indicator in DBD performance. However, the mechanism for ozone generation by electrical discharge in air is rather complicated due to the presence of nitrogen as nitrogen causes ozone destruction processes due to the existence of nitrogen oxides which are also formed. Ozone and nitrogen oxides are formed initially through electron impact dissociation reactions of molecular oxygen and nitrogen. Electrons excite and dissociate molecular oxygen and nitrogen molecules which subsequently reacts to form ozone and nitrogen oxides. Equations 4.12 to 4.16 presents simplified equations relating to ozone and nitrogen oxide formation where M represents any third body in the system[6,7]:

$$O_2 + e^- \rightarrow O + O + e^- \qquad \text{(Eq. 4.12)}$$

$$O + O_2 + M \rightarrow O_3 + M \qquad \text{(Eq. 4.13)}$$

$$N_2 + e^- \rightarrow N + N + e^- \qquad \text{(Eq. 4.14)}$$

$$N + O_2 \rightarrow NO + O \qquad \text{(Eq. 4.15)}$$

$$N + O_3 \rightarrow NO + O_2 \qquad \text{(Eq. 4.16)}$$

Ozone and nitrogen oxides that were generated from the gas discharge were analyzed using gas detection tubes system (182SA&B for O_3, 175SA&SH for $NO+NO_2$ and 117SA&SB for NO_2 Kitagawa Komyo Rikagaku Kogyo) and the effect of reactor parameters to the effluent gas composition are discussed in this section.

The effect of reactor length on ozone and nitrogen oxides generated within the DBD reactor are presented in Figure 4.12. Ozone and nitrogen oxides detection tubes were used but nitrogen dioxides were not detected in the effluent thus all results are presented for just ozone and nitrogen oxide. Results showed that ozone and nitrogen oxide concentration increased linearly with the specific input energy. At the same range of applied voltage values, reactors with longer effective length showed higher values for specific input energy as well as ozone and nitrogen oxide concentrations. As discussed in the previous section, with increasing reactor length, the discharge power also increased and as the specific input energy is directly related to discharge power (Eq. 4.5), it increased as well. And given the same gas flow rate, increasing the effective length of the reactor also increased the residence time of the gas molecules within the discharge region thus giving higher concentrations for ozone and nitrogen oxides.

The effect of TiO_2 loading on ozone and nitrogen oxides generated within the DBD reactor are presented in Figure 4.13. Addition of TiO_2 within the discharge region did not affect the behavior of ozone and nitrogen oxides as they still increased linearly with specific input energy. With increasing TiO_2 loading, the concentrations of ozone and nitrogen oxide reduced. The reduction in concentrations could either be due to the reduction in discharge volume resulting in a smaller amount of excited electrons that can react to form ozone and nitrogen oxide or the self decomposition of ozone and nitrogen oxide on the TiO_2 surface.

The effect of reactor configuration on ozone and nitrogen oxide generated within the DBD reactor are presented in Figure 4.14. Here, TiO_2 is placed within the discharge region (PDC) and just outside of the discharge region (PAC). Results showed that lower concentrations for ozone and nitrogen oxide are observed for PDC as compared to PAC. This indicated that reduction observed in PAC was due to the self decomposition reactions on the TiO_2 surface and the lower concentrations in PDC were due to the combined self decomposition reactions as well as the reduction in discharge volume.

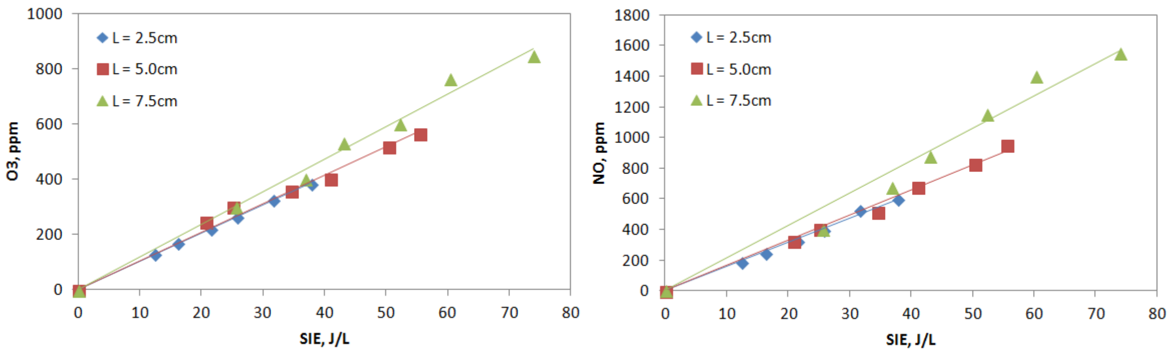

Figure 4.15. Effect of reactor length on ozone and nitrogen oxides concentration in the DBD effluent

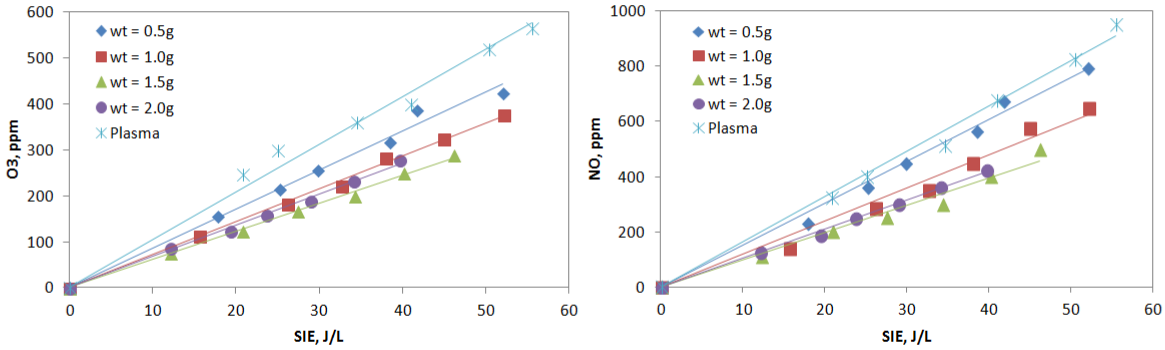

Figure 4.16. Effect of TiO_2 loading on ozone and nitrogen oxides concentration in the DBD effluent (L = 5.0 cm)

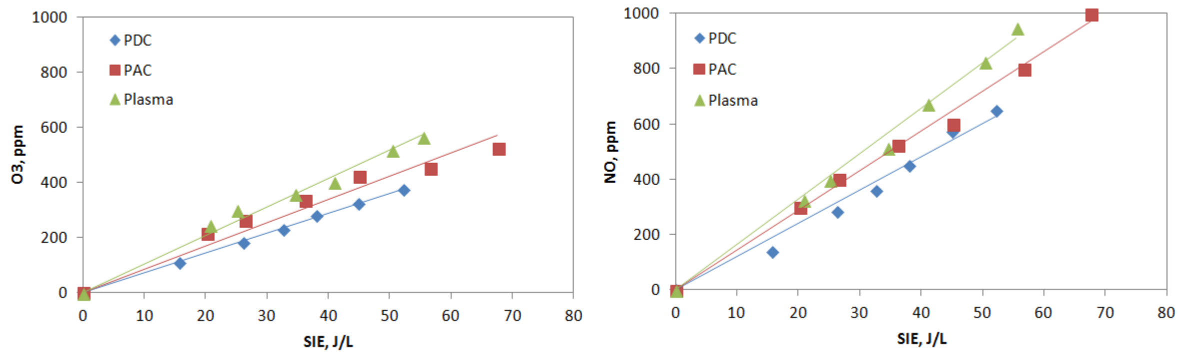

Figure 4.17. Effect of reactor configuration on ozone and nitrogen oxides concentration in the DBD effluent (L = 5.0 cm, wt = 1.0 g)

4.6 Summary of results

This chapter discussed the effect of reactor parameters to the discharge characteristics and effluent composition produced in the dielectric barrier discharge reactor. The effect of reactor length, TiO_2 loading, and reactor configuration was investigated.

The increase in reactor length led to the increase in discharge volume which effectively increased the concentration of ozone and nitrogen oxides produced as well as showed higher values for discharge power at the same range of applied voltages to the DBD reactor. Ozone and nitrogen oxide concentration showed a linear relationship with the specific input energy regardless of reactor length.

By adding TiO_2 within the discharge region, this reduced the discharge volume as well as changed the overall capacitance of the reactor thus also changing its discharge characteristics. This was observed from the shape of the *V-Q* diagram as it deviated from ideal parallelogram and had rounded edges. The reduced discharge gap also resulted a decrease in discharge power as the voltage required to initiate discharge was also reduced. Ozone and nitrogen oxide concentrations showed lower values than those produced by non-thermal plasma alone. The reduction in the concentrations were attributed to self decomposition reactions and the reduction in discharge volume which reduced the amount of excited electrons available for reaction with oxygen and nitrogen to form ozone and nitrogen oxide. With increasing TiO_2 loading, ozone and nitrogen oxide concentration as well as the discharge power decreased.

The effect of reactor configuration was also investigated by having TiO_2 placed directly within the discharge region (plasma driven catalysts, PDC) or just outside of the discharge region (plasma assisted catalysis, PAC). As expected, lower discharge power values were observed for the PDC system as compared to non-thermal plasma alone. Interestingly, higher values for discharge power were observed for the PAC system compared to non-thermal plasma alone. It was suggested that since the catalysts in the PAC system were located just at the edge of the discharge region, this produced a non-uniform discharge where the discharge could have occurred not only along the discharge region but also concentrated along the edge were the catalysts were located as well. Ozone and nitrogen oxide concentrations showed lower values both for the PDC system and the PAC system than non-thermal plasma alone with the PDC system showing lower values than the PAC system. This indicated that for the PAC system, ozone and nitrogen oxide decomposition reactions were promoted on the catalyst surface wherein the PDC system, both the decomposition reactions as well as the reduced discharge volume led to the decrease in ozone and nitrogen oxide concentrations.

The effect of reactor parameters on electron density and electron temperature were estimated from the data obtained in the *V-Q* diagrams. Regardless of the reactor condition, electron density increased with applied voltage. With increasing reactor length and TiO_2 loading, electron density also increased. Electron temperature increased with increasing reactor length but decreased with increasing TiO_2 loading.

Chapter References

[1] **Wagner, H.-E., Brandenburg, R., Kozlov, K.V., Sonnenfeld, A., Michel, P., Behnke, J.F.** *The barrier discharge: basic properties and applications to surface treatment.* Vacuum 71 (2003) 417-436.

[2] **Wang, C., Zhang, G., Wang, X.** *Comparisons of discharge characteristics of a dielectric barrier discharge with different electrode structures.* Vacuum 86 (2012) 960-964.

[3] **Suzuki, S., Sekiguchi, H., Takaki, K.** *The effect of electron density and electron temperature on the partial oxidation of benzene using a micro-plasma reactor.* Journal of Chemical Engineering of Japan 40 (2007) 749-754.

[4] **Bashir, M., Rees, J.M., Bashir, S., Zimmerman, W.B.** *Characterization of atmospheric pressure microplasma produced from argon and a mixture of argon-ethlyenediamine*. Physics Letters A 378 (2014) 2395-2405.

[5] National Physical Library. *Electron mobility*. Retrieved from http://www.kayelaby.npl.co.uk/atomic_and_nuclear_physics/4_4/4_4_2.html, accessed August 5, 2015.

[6] **Lee, M.H., Change, M.B., Wei, T.C.** *Kinetic modelling of ozone generation via dielectric barrier discharges.* Ozone: Science and Engineering 26 (2004) 551-562.

[7] **Pekarek, S.** *Non-thermal plasma ozone generation.* Acta Polytechnica 43 (2003) 47-51.

Chapter 5

EFFECT OF CATALYSTS ON NON-THERMAL PLASMA DISCHARGE

Ozone generation efficiency is usually used as a good indicator in dielectric barrier discharge performance. Ozone is a powerful oxidant and is utilized in the decomposition of volatile organic compounds in non-thermal plasma catalysis systems. Previous studies have also reported that active oxygen species resulting from the decomposition of ozone on catalyst surfaces showed higher activities in decomposing VOCs than ozone. Unfortunately, when working with air plasma in non-thermal plasma catalysis, the formation of nitrogen oxides cannot be avoided and this together with residual ozone are considered as secondary pollutants. This chapter examines the catalytic activity of the prepared catalysts presented in Chapter 3 in limiting ozone and nitrogen oxides generated within the DBD reactor.

5.1 Experimental set-up

Figure 5.1 shows experimental set-up and the dielectric barrier discharge (DBD) reactor used for this part of the study and is similar to that used in Chapter 4. Synthetic air was fed into the DBD reactor at a flow rate of 550 mL/min at standard ambient atmospheric conditions. The DBD reactor used was made of a quartz tube with an inside diameter of 13 mm, length of 200 mm and a thickness of 1 mm. A stainless steel rod with a diameter of 9 mm was fixed along the center of the quartz tube to function as the high-voltage electrode and silver paint was coated outside the reactor at a length of 50 mm to form the effective length of the reactor and to function as the ground electrode. Non-thermal plasma was generated by varying the applied voltage supplied to the reactor. At each voltage setting, the voltage readings across the reactor and the capacitor attached in series with the reactor were recorded by the oscilloscope by averaging 64 scans and effluent concentrations of ozone and nitrogen oxides were analyzed using gas detection tube system (Ozone 182SA&B, Nitrogen oxides 175SA&SH, Nitrogen dioxide 117SA&SB; Kitagawa Komyo Rikagaku Kogyo).

For all the experiments, 2 g of the prepared catalyst were placed within the effective length of the reactor. The corresponding weight hourly space velocity was calculated as 19.53 h^{-1} based on the density of dry air at 25^{o}C which is 1.1839 kg/m^3. And the corresponding gas hourly space velocity using bare TiO_2 was 26,750 h^{-1} and was calculated based on the gas residence time in the void of the catalyst bed which was 0.35. The catalysts used for the experiments were those presented in Chapter 3.

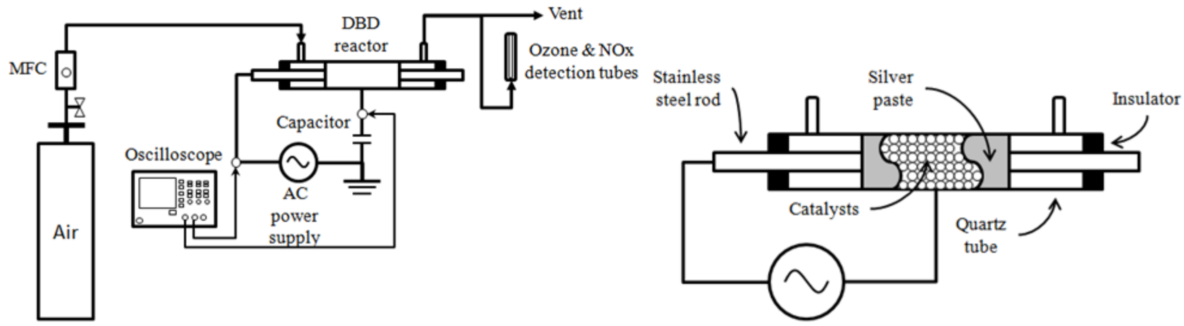

Figure 5.1. Experimental set-up and dielectric barrier discharge reactor used to determine the effect of the prepared catalysts on non-thermal plasma discharge

5.2 Summary of catalyst properties

The catalysts used for this part of the study were Ag/TiO_2, Mn/TiO_2, and $Ag\text{-}Mn/TiO_2$ prepared by impregnation method and by deposition methods with varying metal loading of 1%, 3% and 5% by weight. A summary of the catalyst specific surface area and bulk chemical species discussed in Chapter 3 are presented in Table 5.1.

Table 5. 1. Summary of specific surface area and bulk chemical species of the prepared catalysts

TiO_2	SSA, m^2/g		64.95			
			IP	DPN	DPH	
Ag/TiO_2	SSA, m^2/g	1%	61.64	64.73	65.54	
		3%	53.54	64.60	65.14	
		5%	49.00	63.28	64.94	
	Bulk metal		Ag/TiO_2	Ag_2O/TiO_2	AgO/TiO_2	
	Metal fraction		1.0	0.78	0.76	
			IP T350	IP T600	IP T800	DPN
Mn/TiO_2	SSA, m^2/g	1%	76.49	71.97	51.64	74.86
		3%	76.91	66.12	1.54	74.45
		5%	72.36	61.57	2.04	72.95
	Bulk metal		MnO_2/TiO_2	Mn_2O_3/TiO_2	$MnTiO_3$	Mn_3O_4/TiO_2
	Metal fraction		0.58	0.76	0.49	0.68
			IP	DPN		
$Ag\text{-}Mn/TiO_2$	SSA, m^2/g	1%	73.30	74.62		
		3%	73.80	70.23		
		5%	72.35	67.45		
	Bulk metal		$Ag\text{-}MnO_2/TiO_2$	$Ag_2O\text{-}MnO_2/TiO_2$		
	Metal fraction		1.0/0.37[a]	0.92/0.51[a]		

[a] first fraction is for Ag followed by Mn fraction

Catalysts were prepared by impregnation method (IP), deposition-precipitation method with sodium hydroxide (DPN), and by deposition-precipitation method with hydrogen peroxide (DPH) with metal loadings of 1%, 3%, and 5% by weight. Impregnated catalysts were labelled as either IP*x* for Ag/TiO_2 and $Ag\text{-}Mn/TiO_2$ catalysts, or IP*x*T*y* for the Mn/TiO_2 catalysts; DPN*x* for catalysts prepared by deposition-precipitation method with sodium hydroxide; and DPH*x* for catalysts prepared by deposition-precipitation with hydrogen peroxide. Here, *x* represents the metal loading amount and *y* represents the calcination temperature.

5.3 Effect of catalysts on ozone and nitrogen oxide concentrations

5.3.1 Ag/TiO_2

The effect of Ag/TiO_2 catalysts on ozone and nitrogen oxide concentrations are presented in Fig. 5.2. Similar with just bare TiO_2, ozone and nitrogen oxide concentrations followed a linear relationship with specific input energy. As compared to air plasma alone, the addition of the catalysts decreased the amount of ozone and nitrogen oxide found in the effluent of the DBD reactor.

To compare the effect of the catalysts easily, the ozone and nitrogen oxide generation efficiency was calculated based on the slopes of the linearized data (in ppm/SIE). The generation efficiency ratio was then calculated as the ratio of the generation efficiency with the catalyst divided by that of air plasma. The results are presented in Fig. 5.3. Among the Ag/TiO_2 catalysts that were tested, DPN3 catalyst showed the highest reduction in ozone and nitrogen oxide generation efficiency ratio having a value of 0.13 for ozone and 0.09 for nitrogen oxide. However, there was no clear trend observed between the Ag/TiO_2 catalysts.

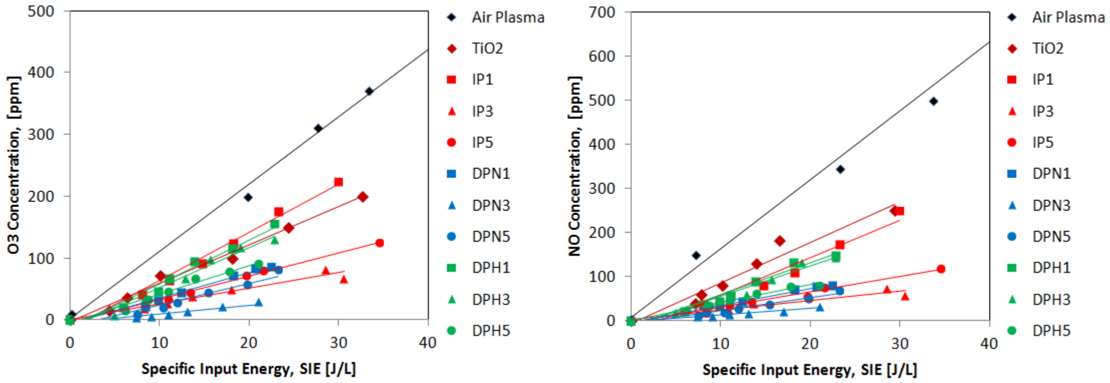

Figure 5.2. Effect of Ag/TiO_2 catalysts on ozone and nitrogen oxides concentrations

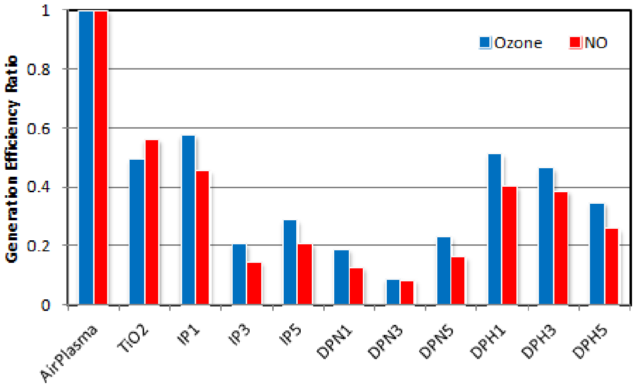

Figure 5.3. Comparison of generation efficiency ratio between the differently prepared Ag/TiO_2 catalysts for limiting ozone and nitrogen oxide concentrations in the DBD effluent

5.3.2 Mn/TiO_2

The effect of Mn/TiO_2 catalyst preparation method on ozone and nitrogen oxide concentrations using 5% Mn/TiO_2 are presented in Fig. 5.4. IP5T350, IP5T600 and DPN5 showed similar results while IP5T800 only showed slightly better results than bare TiO_2. As compared to the other catalysts, IP5T800 were calcined at a significantly high temperature of 800°C which caused sintering on the catalysts resulting in the formation of $MnTiO_3$. Here, Mn was no longer loaded on TiO_2 but rather part of the bulk catalyst structure. Also, the high calcination temperature also significantly reduced its specific surface area which could have led to poor surface interaction of ozone and nitrogen oxide on the catalyst surface.

The effect of Mn loading on ozone and nitrogen oxide concentrations are presented in Fig. 5.5 and 5.6, respectively. With increasing manganese loading, further reductions in ozone and nitrogen oxide concentrations were observed. It was only the catalysts calcined at 800°C, specifically, IP1T800 and IP3T800 which showed poorer results in reducing ozone and nitrogen oxide concentrations than bare TiO_2.

The generation efficiency ratios for ozone and nitrogen oxides were also calculated for Mn/TiO_2 catalysts and the results are presented in Fig. 5.7. Compared to Ag/TiO_2 catalysts, Mn/TiO_2 catalysts showed a clear trend with respect to generation efficiency ratios. With increasing metal loading, the degree of reduction in ozone and nitrogen oxide concentrations increased. And in terms of catalyst preparation method, the degree of reduction is as follows: IP T350 > IP T600 > DPN > and lastly, IP T800.

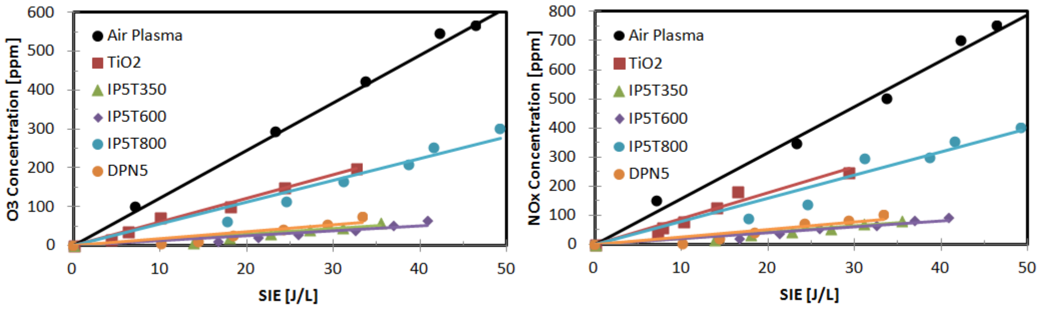

Figure 5.4. Effect of 5% Mn/TiO$_2$ catalyst preparation method on ozone and nitrogen oxides concentrations

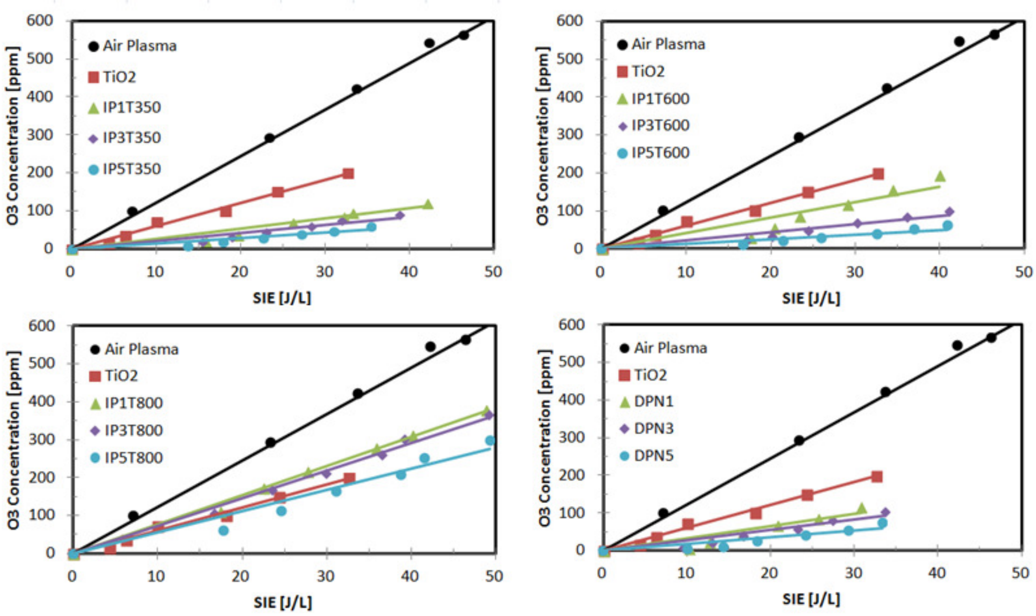

Figure 5.5. Effect of Mn/TiO$_2$ metal loading on ozone concentration

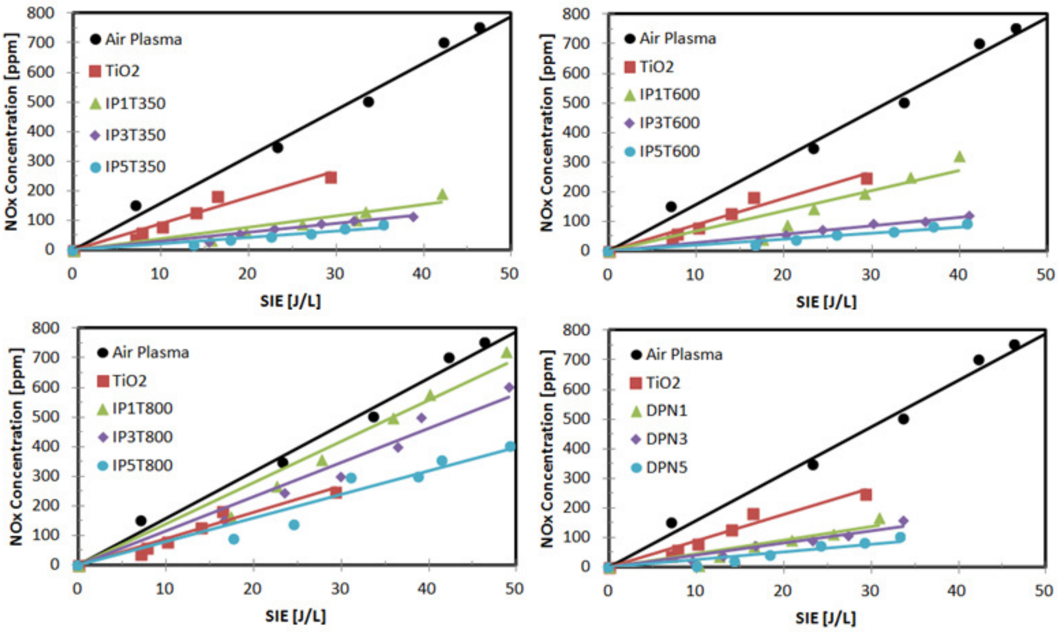

Figure 5.6. Effect of Mn/TiO$_2$ metal loading on nitrogen oxide concentration

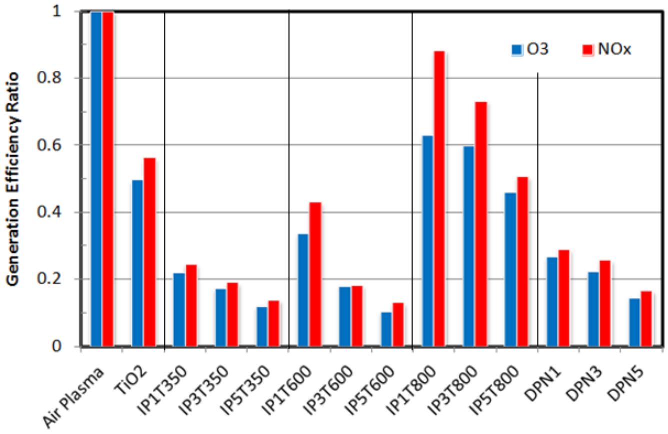

Figure 5.7. Comparison of generation efficiency ratio between the differently prepared Mn/TiO$_2$ catalysts for limiting ozone and nitrogen oxide concentrations in the DBD effluent

5.3.3 Ag-Mn/TiO$_2$

The effect of Ag-Mn/TiO$_2$ catalysts on ozone and nitrogen oxide concentrations are presented in Fig. 5.8 and the corresponding generation efficiency ratios are presented in Fig. 5.9. Results showed that there were not much difference in the performance of IP5 and DPN catalysts even with increasing metal loading and preparation method. For the IP catalysts however, IP3 showed the highest reduction followed by IP1, and then by IP5.

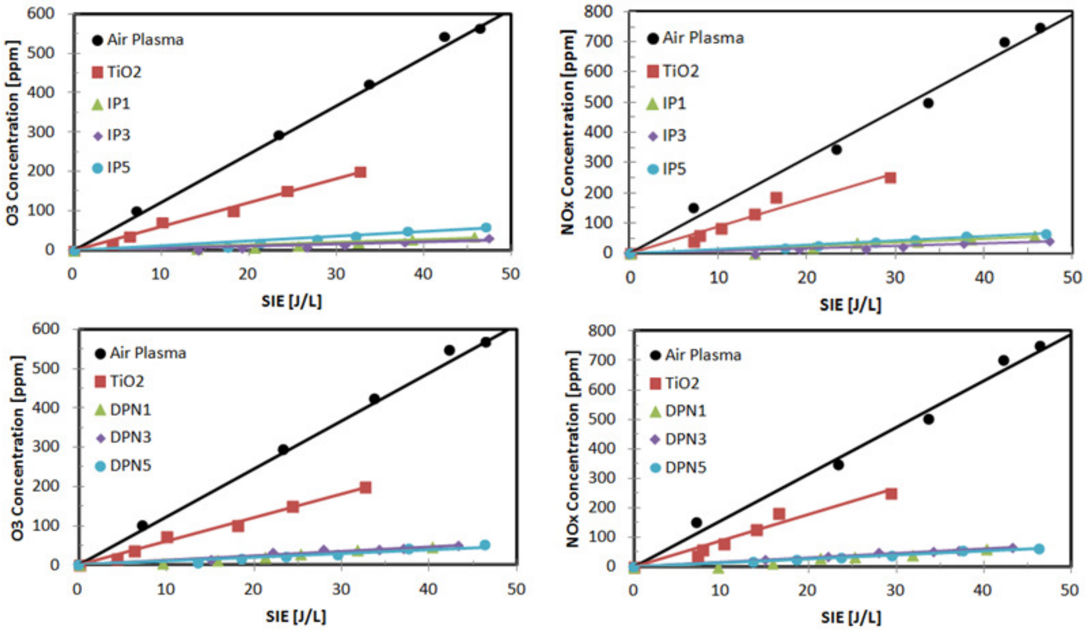

Figure 5.8. Effect of Ag-Mn/TiO$_2$ catalysts on ozone and nitrogen oxides concentrations

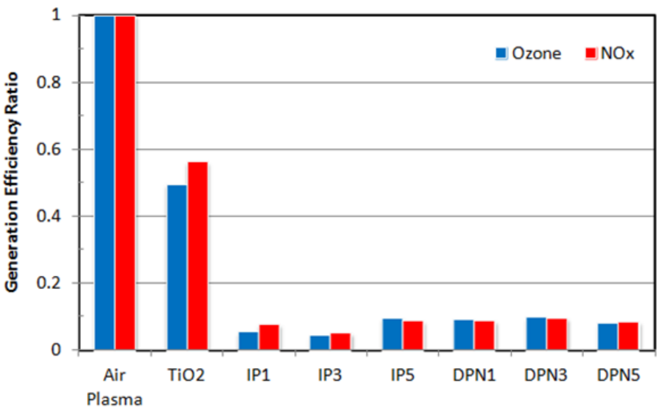

Figure 5.9. Comparison of generation efficiency ratio between the differently prepared Ag/TiO_2 catalysts for limiting ozone and nitrogen oxide concentrations in the DBD effluent

5.4 Effect of catalyst surface area on ozone generation

To determine which among the Ag/TiO_2 and Mn/TiO_2 catalysts characteristics: the specific surface area, metal loading, and the metal oxidation state, played the more dominant role in reducing ozone generation, the specific surface area of the catalyst were plotted against ozone generation efficiency and is presented in Fig. 5.9.

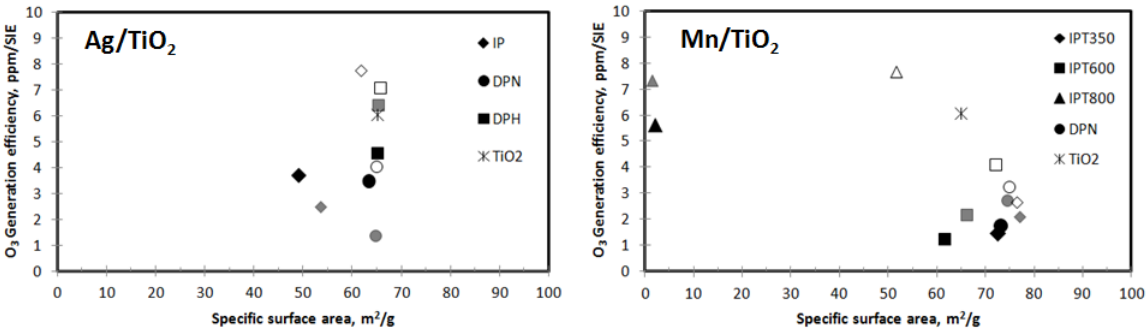

Figure 5.10. Effect of Ag/TiO_2 and Mn/TiO_2 catalyst specific surface area on ozone generation efficiency (open - 1%, grey - 3%, filled - 5% metal loading)

In the Ag/TiO_2 catalysts, there was little change in the specific surface area of the DPN and DPH catalysts but ozone generation decreased with increasing Ag loading. For the IP catalysts, even with decreasing specific surface area, lower ozone generation efficiency were obtained with increasing Ag loading. In the Mn/TiO_2 catalysts, the specific surface area of IPT350, IPT600 and DPN catalysts decreased with increasing Mn loading but higher reductions in ozone generation were observed. For the IPT800 catalysts, the IP3T800 catalysts showed better performance in reducing ozone generation than the IP1T800 catalyst regardless of the large difference in their specific surface area. With IP3T800 and IP5T800, although the surface area of the two catalysts are similar, the increase in Mn loading found in IP5T800 showed higher reduction in ozone generation than the IP3T800 catalyst.

5.5 Summary of results

Based from these results, it can be said that the metal oxidation state which highly depend on the catalyst preparation method, is the prevailing characteristic which controls ozone generation. It was expected that with increasing metal loading, further reductions on ozone generation would be observed as there would be more metal available for surface reactions. However, there were some cases where with increase in metal loading, higher ozone generation were observed compared to catalysts with lower metal loading. This indicated that there must be a balance and an optimum metal loading amount on the TiO_2 to effectively limit ozone generation within the DBD reactor.

The decrease in ozone generation could be explained by the decrease in discharge volume due to the presence of the catalyst which would limit ozone production or the self-decomposition reactions of ozone on the catalyst surface. Based from the results presented, addition of the metals on TiO_2 further reduced the amount of ozone and nitrogen oxides found in the effluent of the DBD reactor. This indicated that addition of the metal on TiO_2 promoted self -decomposition reactions of ozone. An alternative mechanism for ozone decomposition on metal oxides was proposed based on the following reactions[1]:

$$O_3 + \left[M^{n+}\right] \rightarrow O_2 + O^-\left[M^{n+1}\right] \qquad \text{(Eq. 5.1)}$$

$$O_3 + O^-\left[M^{n+1}\right] \rightarrow 2O_2 + \left[M^{n+}\right] \qquad \text{(Eq. 5.2)}$$

$$2O^-\left[M^{n+1}\right] \rightarrow O_2 + \left[M^{n+}\right] \qquad \text{(Eq. 5.3)}$$

Based from these reduction-oxidation reactions, catalytic activity towards ozone decomposition depends on the rate of Eq. 5.1 and since higher metal oxidation states are also good for ozone adsorption and would also lead to the generation of more adsorbed oxygen (O_2^-, O^-, O_2^{2-}) that has partial ionic character and is favorable for ozone decomposition[2]. Catalysts with multiple oxidation states like Ag/TiO_2 by DPN and DPH methods, Mn/TiO_2 by all preparation methods, and $Ag\text{-}Mn/TiO_2$, where aside from having multiple oxidation states also had multiple metal oxides on the catalyst surface, would allow multiple redox reactions occurring simultaneously for the decomposition of ozone.

Chapter References

[1] **Zhihua L., Ma J., He H.** *Decomposition of high-level ozone under high humidity over Mn-Fe catalyst: The influence of iron precursors.* Catalysis Communications 59 (2015) 156-160

[2] **Tang W.X., Liu H.D., Wu X.F., Chen Y.F.** *Higher oxidation state responsible for ozone decomposition at room temperature over manganese and cobalt oxides: effect of calcination temperature.* Ozone: Science and Engineering 36 (2014) 502-512

Chapter 6

DECOMPOSITION OF BENZENE USING PLASMA DRIVEN CATALYSIS

In this chapter, the decomposition of benzene using a plasma driven catalysis system is discussed. Based from the results observed in Chapter 5, ozone and nitrogen oxide generation was limited in varying degrees by increasing the metal loading on the TiO_2 *with the highest reduction observed with the catalysts with higher metal loading. For this part of the study, the catalysts loaded with 5% metal were used. Benzene decomposition, ozone and nitrogen oxide concentrations, carbon balance, carbon dioxide yield were monitored for the activity tests.*

6.1 Experimental set-up

Figure 6.1 shows experimental set-up and the dielectric barrier discharge (DBD) reactor used for this part of the study. Bubbling method was used to set the benzene concentration in the as stream and the concentration was controlled either by the flow rate of air into liquid benzene or by adjusting the temperature of the water bath. The total feed flow rate was controlled by using air as balance gas and was set at 550 mL/min at standard ambient conditions. The resulting gas feed was flowed through a mixing tank before entering into the DBD reactor. For all the experiments, 2 g of the prepared catalyst were placed within the effective length of the reactor. The corresponding weight hourly space velocity was calculated as 19.53 h^{-1} based on the density of dry air at 25°C which is 1.1839 kg/m^3. And the corresponding gas hourly space velocity using bare TiO_2 was 26,750 h^{-1} and was calculated based on the gas residence time in the void of the catalyst bed which was 0.35. The catalysts used for the experiments were those presented in Chapter 3 using 5% metal loading.

The DBD reactor used was made of a quartz tube with an inside diameter of 13 mm, length of 200 mm and a thickness of 1 mm. A stainless steel rod with a diameter of 9 mm was fixed along the center of the quartz tube to function as the high-voltage electrode and silver paint was coated outside the reactor at a length of 50 mm to form the effective length of the reactor and to function as the ground electrode. Non-thermal plasma was generated by varying the applied voltage supplied to the reactor. At each voltage setting, the voltage readings across the reactor and the capacitor attached in series with the reactor were recorded by the oscilloscope by averaging 64 scans. Effluent composition and concentrations for benzene were analyzed by gas chromatograph-mass spectrometer (GCMS-PQ5050A, Shimadzu Corp.) equipped with an PoraBOND Q column (CP7348, Agilent Technologies); carbon dioxide and carbon monoxide concentrations were analyzed by gas chromatograph with a thermal conductivity detector (GC390, GL Sciences); and ozone and nitrogen oxides were analyzed using a gas detection tube system (Ozone 182SA&B, Nitrogen oxides

175SA&SH, Nitrogen dioxide 117SA&SB; Kitagawa Komyo Rikagaku Kogyo). The carbon balance and carbon dioxide yield were calculated using Eqs. 6.1 and 6.2, respectively.

$$\text{Carbon Balance, } \% = \frac{[CO_2]+[CO]+n[\text{by-products}]+6[C_6H_6]}{6[C_6H_6]_0} x100 \qquad \text{(Eq. 6.1)}$$

$$Y_{CO_2}, \% = \frac{[CO_2]}{6\left([C_6H_6]_0-[C_6H_6]\right)} x100 \qquad \text{(Eq. 6.2)}$$

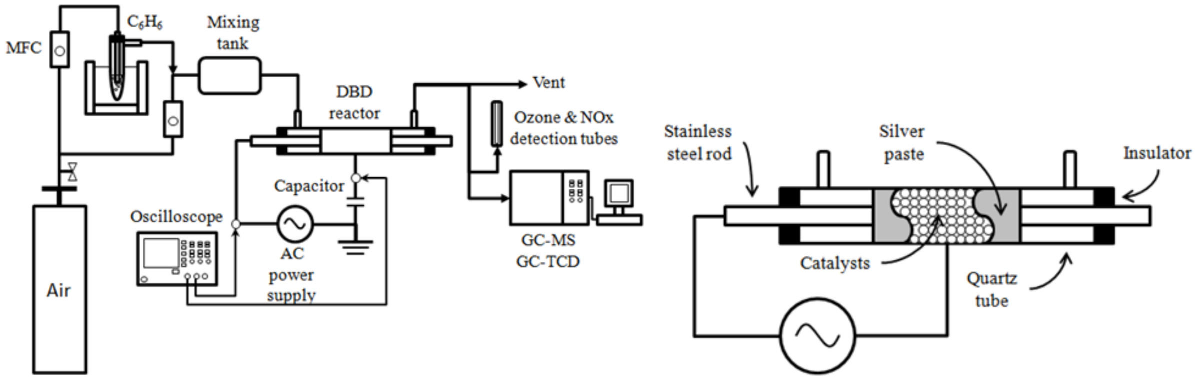

Figure 6.1. Experimental set-up and the dielectric barrier discharge reactor used for the plasma driven catalysis decomposition of benzene

6.2 Non-thermal plasma catalytic decomposition of benzene

Benzene decomposition experiments were performed using non-thermal plasma and a plasma driven catalysis system. Initial benzene concentration was set at 200 ppm and benzene decomposition experiments were performed by varying the voltage applied to the reactor while monitoring effluent composition and concentrations. The effect of plasma on benzene concentration was tested by allowing the pollutant to go through the reactor without the catalysts while the plasma was turned on and testing its concentration afterwards. For the plasma driven catalysis system, the catalysts in the reactor were first saturated with gas-phase benzene until adsorption equilibrium was reached. After adsorption equilibrium, activity tests were performed using the same range of applied voltages to the reactor similar with the plasma alone experiment.

Results for plasma alone treatment and the effect of Ag/TiO_2 catalysts on benzene decomposition are presented in Fig. 6.2. It was found out that plasma alone was able to decompose benzene up to 18% at the highest tested input energy values. Plasma generates accelerated and energetic electrons which collides with bulk gas molecules to initiate excitation, dissociation, and ionization reactions producing short- and long-lived plasma species which are made available to react to decompose benzene.

Using Ag/TiO_2 IP5 catalyst improved benzene decomposition to 28%, however, DPN5 and DPH5 catalysts showed a decrease in benzene decomposition at only 12%. Even though IP5 catalyst had a lower specific surface area (49.00 m^2/g) compared to DPN5 (63.28 m^2/g) and DPH5 (64.94 m^2/g), IP5 catalysts showed better efficiency. In DPN5 and DPH5 catalysts, silver was deposited and formed a layer and covered the TiO_2 surface resulting in higher metal surface concentration than the IP5 catalysts. This could indicate that for Ag/TiO_2 catalysts to work effectively, benzene must be adsorbed and then transferred between the TiO_2 and silver/oxide for decomposition to occur. Having too much silver loaded on TiO_2 surface deterred benzene decomposition and an optimum metal loading should be considered when using Ag/TiO_2 catalysts.

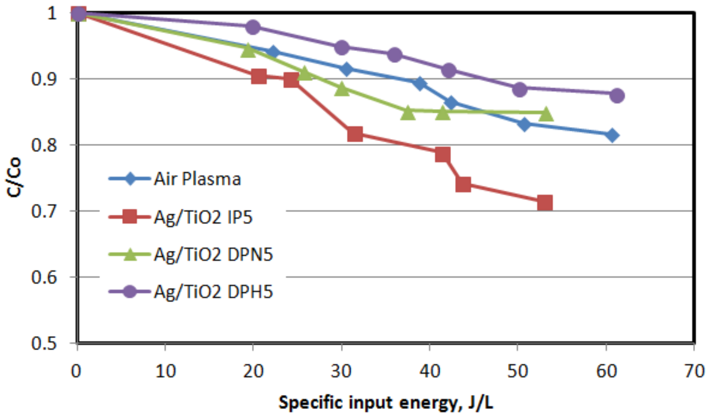

Figure 6.2. Effect of Ag/TiO_2 catalysts on benzene decomposition

Results for plasma alone treatment and the effect of Mn/TiO_2 catalysts on benzene decomposition are presented in Fig. 6.3. The Mn/TiO_2 catalysts showed varying degrees of decomposition efficiency depending on the catalyst preparation method. The IP5T350 catalysts showed the highest decomposition efficiency at 33% followed by DPN5 at 25%, IP5T600 at 19% and lastly by IP5T800, which showed poorer decomposition efficiency compared to air plasma treatment alone at 16%. Even though IP5T350 and DPN5 catalysts had similar specific surface area (72.36 m^2/g and 72.95 m^2/g), IP5T35 showed better performance than DPN5 which could be due to the oxidation state of manganese loaded on TiO_2. In IP5T350, manganese exists mainly in the Mn^{4+} state (MnO_2) where in DPN5 it exists as Mn^{2+} and Mn^{3+} states (Mn_3O_4). For IP5T600, this catalyst had a specific surface area of 61.57 m^2/g and had manganese in the Mn^{3+} state (Mn_2O_3). For the IP5T800 catalysts, there was a large decrease in surface area (2.04 m^2/g) and manganese existed in the Mn^{2+} state in the form of $MnTiO_3$ as part of the bulk structure of the catalyst which was formed because of the high calcination temperature. The location of manganese in the catalyst, interstitial rather than on the surface, the decrease in specific surface area, and the decrease catalyst volume due to sintering, decreased the probability of benzene to react on the catalyst surface thus showing poor decomposition efficiency.

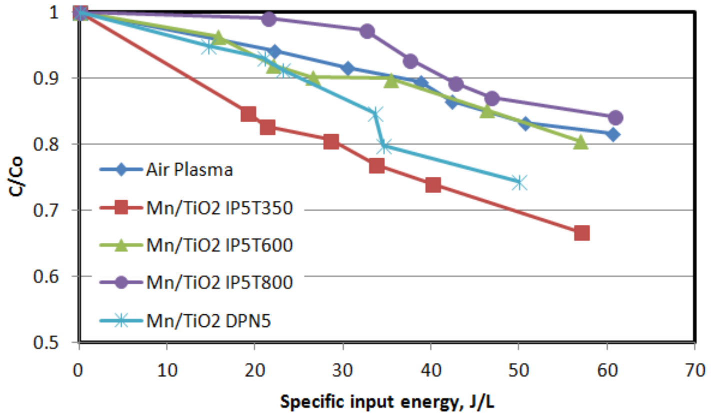

Figure 6.3. Effect of Mn/TiO$_2$ catalysts on benzene decomposition

Results for plasma alone treatment and the effect of Ag-Mn/TiO$_2$ catalysts on benzene decomposition are presented in Fig. 6.4. The Ag-Mn/TiO$_2$ DPN5 catalyst showed the highest decomposition efficiency among the tested catalysts at 33% while the IP5 catalyst was able to decompose benzene at 30%. Even though the DPN5 catalyst had a slightly lower specific surface area (67.45 m^2/g) than the IP5 catalyst (72.35 m^2/g), it showed better performance which could be because of the oxidation state of the metals on the TiO$_2$ - the DPN5 catalysts had Ag$_2$O-MnO$_2$ while the IP5 catalyst had Ag-MnO$_2$ as the metal oxide loaded on TiO$_2$.

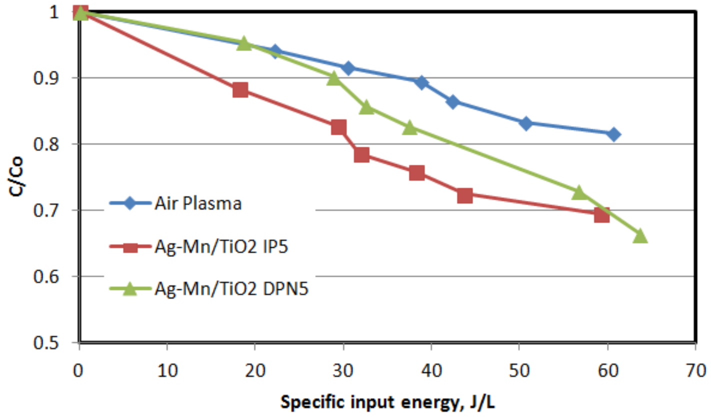

Figure 6.4. Effect of Ag-Mn/TiO$_2$ catalysts on benzene decomposition

Aside from benzene decomposition, effluent analysis during the experiment only showed benzene, carbon dioxide, ozone and nitrogen oxide. A summary and comparison of the results from the activity tests are presented in Table 6.1. The results for the maximum applied voltage setting, discharge power, specific input energy, electron temperature, electron density, ozone and nitrogen oxide concentrations, % decomposition, carbon balance, and carbon dioxide yield were presented. The unaccounted carbon was attributed to adsorbed or deposited carbon on the catalyst surface or to by-products that were not detected by either the GC-MS or GC-TCD. Since the accountable effluent composition only showed benzene, ozone and nitrogen oxide, and carbon dioxide, this indicated that the catalysts presented 100% selectivity towards carbon dioxide formation.

Depending on the catalyst used, results showed varying degree of benzene decomposition, final ozone and nitrogen oxide concentrations, carbon balance and carbon dioxide yield. Air plasma was able to decompose benzene up to 18.39% at an SIE of 60.52 J/L but showed high concentrations for ozone at 300 ppm and nitrogen oxide at 360 ppm. Also, carbon balance was only 82.78% with a carbon dioxide yield of 6.35%. This indicated that there was incomplete mineralization of the pollutant and resulted in the formation of by-products.

For the Ag/TiO_2 catalysts, only the catalyst prepared by IP method showed an improvement in benzene decomposition. But for all Ag/TiO_2 catalysts, there was a reduction in final ozone and nitrogen oxide concentration and a significant improvement in carbon balance and carbon dioxide yield. Among the Ag/TiO_2 catalysts, the one prepared by DPN method showed the highest carbon balance at 97.66% and carbon dioxide yield at 84.47% but only decomposed the benzene at 12.09% which was lower than that by air plasma alone. The DPH5 catalyst, although showed similar efficiency with DPN5 catalysts for benzene decomposition at 12.28%, had relatively lower carbon balance at 96.81% and carbon dioxide yield at 73.98%.

For the Mn/TiO_2 catalysts, the IP5T350 catalyst showed the highest benzene decomposition at 33.20% and also the lowest concentrations for ozone and nitrogen oxide at 25 ppm and 28 ppm, respectively. Carbon balance presented at 91.88% and carbon dioxide yield at 75.56% which also showed an improvement compared to air plasma treatment alone. The DPN5 catalyst showed lower benzene decomposition efficiency at 25.68% but also at a lower SIE value of 49.93 J/L as compared to 56.95 J/L in the IP5T350 catalyst. Ozone and nitrogen oxide concentrations were similar at 25 ppm and 33 ppm, respectively. However, DPN5 catalyst showed higher carbon balance at 96.07% and carbon dioxide yield at 84.71% compared to IP5T350. The IP5T600 catalyst showed poorer performance than both the IP5T350 and DPN catalysts. And lastly, the IP5T800 catalysts showed the poorest performance among the Mn/TiO_2 catalysts with benzene decomposition efficiency of 15.84%, ozone and nitrogen concentrations of 206 ppm and 200 ppm, carbon balance of 86.07% and a very low carbon dioxide yield of 12.09%.

Table 6. 1. Summary of results for benzene decomposition using a plasma driven catalysis system

	Applied Voltage, V	Discharge Power, W	SIE, J/L	T_e, eV	n_e, 10^{11} m^{-3}	O_3, ppm	NO, ppm	% Decomp	% Carbon Balance	% CO_2 Yield
Air Plasma	11 094	0.55	60.51	2.88	15.73	300	4.97	18.39	82.78	6.35
Ag/TiO_2										
IP5	11 100	0.49	52.91	1.82	24.11	133	126	28.53	85.31	48.49
DPN5	11 300	0.49	53.08	1.82	24.22	100	100	15.09	97.66	84.47
DPH5	11 400	0.56	61.01	1.68	30.57	100	100	12.28	96.81	73.98
Mn/TiO_2										
IP5T350	11 875	0.52	56.95	1.66	28.81	25	28	33.20	91.88	75.56
IP5T600	11 719	0.52	56.80	1.78	26.47	32	42	19.41	89.76	47.23
IP5T800	11 719	0.56	60.76	2.92	15.56	206	200	15.84	86.07	12.09
DPN5	11 719	0.46	49.93	1.15	38.77	25	33	25.68	96.07	84.71
Ag-Mn/TiO_2										
IP5	11 563	0.54	59.21	1.36	37.98	40	50	30.49	98.17	94.02
DPN5	11 406	0.58	63.54	1.45	37.71	56	68	33.55	99.28	97.85

For the Ag-Mn/TiO_2 catalysts, both the IP5 catalyst and the DPN5 catalyst showed similar results with DPN5 catalyst performing slightly better than the IP5 catalyst. Among all the tested catalysts, the DPN5 catalyst showed the best performance in all of the tested catalysts in terms of benzene decomposition at 33.55%, carbon balance at 99.28% and carbon dioxide yield at 97.85%.

6.3 Effect of catalysts on discharge characteristics during PDC treatment

6.3.1 Effect of catalysts on electron density during PDC treatment

When catalysts were placed within the discharge region, the discharge gap was shortened causing a change in plasma discharge behavior. The average electric field would be enhanced because of the short distance between adjacent contact points. This would then lead to the plasma energy being consumed by electron-impact reactions which are possible for pollutant decomposition. The catalysts would expand the discharge region as microdischarges are apt to propagate along the catalyst surface. And as the plasma region expands, the concentrations of active species would also increase due to higher collision probability between the accelerated electrons and the gas molecules.

The effect of catalysts on electron density during benzene decomposition are presented in Figs. 6.5 to 6.7. Regardless of whether catalysts were placed within the discharge region, electron density increased with increasing applied voltage to the reactor. For all the catalysts used except for Mn/TiO_2 IP5T800, there was an increase in electron density as compared to only air plasma treatment and the degree of increase in electron density depended on the type of catalysts used.

For Ag/TiO_2 catalysts (Fig. 6.5), IP5 and DPN5 showed a similar trend and DPH5 catalysts showed slightly higher values for electron density. For Mn/TiO_2 catalysts (Fig. 6.6), DPN5 catalysts showed the highest increase in electron density followed by IP5T350, IP5T600, then by IP5T800 which showed similar results with the electron density of air plasma treatment alone. In the IP5T800 catalysts, $MnTiO_3$ was formed there was a large reduction in catalyst volume due to the high calcination temperature where sintering occurred. Here, the manganese was part of the bulk crystal structure rather than being a metal/oxide loaded on the TiO_2 surface. Even though the gap capacitance changed because of the electrical properties of $MnTiO_3$, the discharge voltage showed similar value with that of air plasma thus resulting in similar values for electron density.

For the Ag-Mn/TiO_2 catalysts (Fig. 6.7), similar trend was observed between the IP5 and DPN5 catalysts and showed the highest electron density at 38 x 10^{11} m^{-3}. In this case, the catalysts were loaded with 5% Ag and 5% Mn having a total of 10% loaded metal by weight. The similar results could indicate that there was an optimum metal loading amount that would dictate how the catalyst would affect the discharge characteristics, in this case the electron density, in the discharge region. Regardless of metal distribution and metal oxidation state, the effect would be similar.

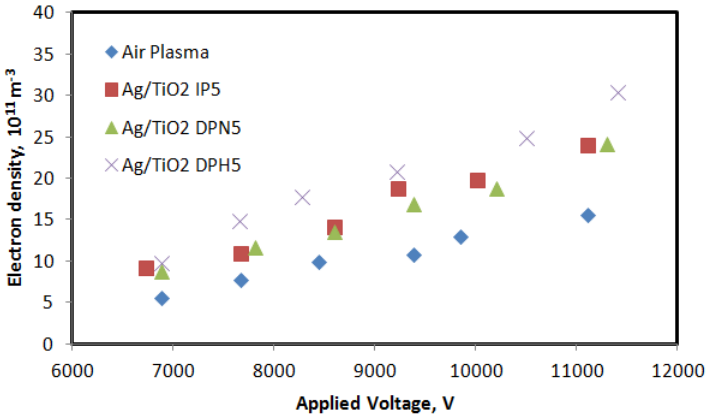

Figure 6.5. Effect of Ag/TiO$_2$ catalysts on electron density during PDC treatment

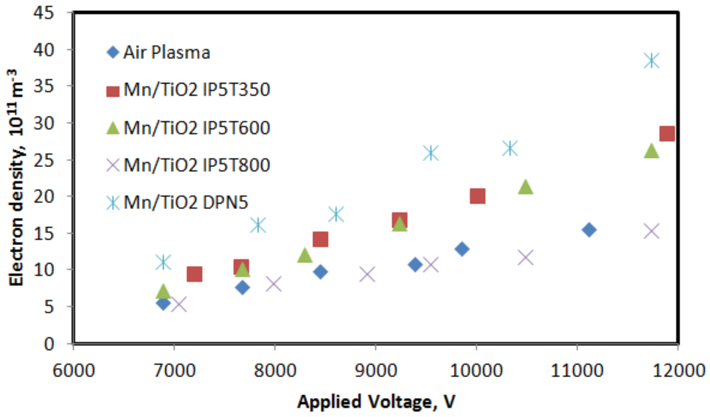

Figure 6.6. Effect of Mn/TiO$_2$ catalysts on electron density during PDC treatment

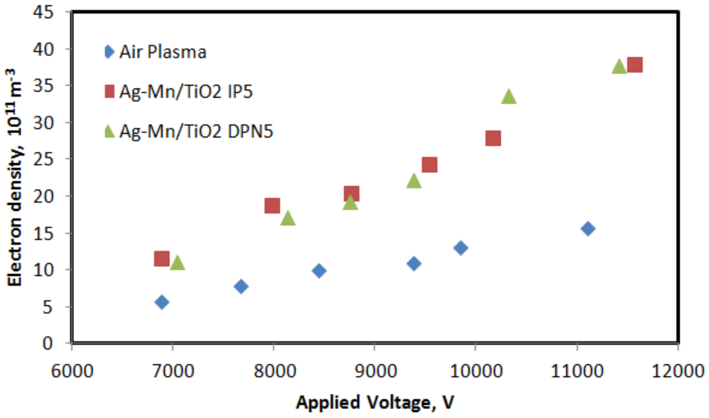

Figure 6.7. Effect of Ag-Mn/TiO$_2$ catalysts on electron density during PDC treatment

The difference in the influence of the catalysts to electron density could be attributed to the differences in their electrical properties, specifically how they affect the gap capacitances within the discharge region. In Ag/TiO_2 and Mn/TiO_2 prepared by deposition-precipitation methods, the metal oxide surface concentration is higher than those prepared by impregnation method. This effectively changed how the catalysts carry charge and increased the current density passing between the electrodes thus increasing electron density. In Ag-Mn/TiO_2 catalysts, regardless of the preparation method, the optimum metal surface concentration was reached showing the maximum increase in electron density that could be enhanced by adding catalysts in the discharge region. Furthermore, microdischarges could be generated within the pores of the catalysts resulting in a larger discharge per volume which increases the electron density leading to a more oxidative plasma discharge.

6.3.2 Effect of electron density on benzene decomposition

The effect of electron density on benzene decomposition are presented below in for Ag/TiO_2 (Fig. 6.8), Mn/TiO_2 (Fig. 6.9), and Ag-Mn/TiO_2 (Fig. 6.10). With increasing electron density, benzene conversion increased and showed an almost linear relationship with electron density regardless of the catalyst used. However, the degree of conversion was dependent on the type of catalyst used.

For Ag/TiO_2 catalysts (Fig. 6.8), it was observed that the trend for IP5 catalysts were similar for air plasma treatment alone but obtained a higher degree of conversion as IP5 catalysts showed higher values for electron density. Even though DPN5 and DPH5 had higher electron density values than during air plasma treatment, lower values for conversion were observed. This indicated that benzene decomposition is not entirely governed by electron density but rather on how the electrons present in the discharge was utilized.

For the Mn/TiO_2 catalysts (Fig. 6.9), again, results show that benzene decomposition does not depend entirely on electron density. DPN5 catalyst showed the highest electron density but IP5T350, even though had a lower electron density at the highest applied voltage, showed the highest decomposition at 33%. At the same electron density, for instance at about 15×10^{11} m^{-3}, varying degrees of decomposition were obtained which depended on the catalyst used.

Similarly for Ag-Mn/TiO_2 catalysts (Fig. 6.10), at the lower value for electron density at around 15×10^{11} m^{-3}, treatment by air plasma alone showed higher decomposition efficiency but upon further increase in electron density IP5 and DPN5 showed superior benzene decomposition at 30% and 33%, respectively.

An increase in electron density was observed when catalysts were placed within the discharge region as this have changed the discharge properties of the plasma. However, an increase in electron density does not necessarily mean that better decomposition efficiency would be achieved. As presented in these results, benzene decomposition still depended on the characteristics of the catalysts itself and not solely on the electron density that is used when characterizing plasma discharge. In this case, it is not just the electrons density which is important but how these electrons are utilized in the decomposition of the pollutant.

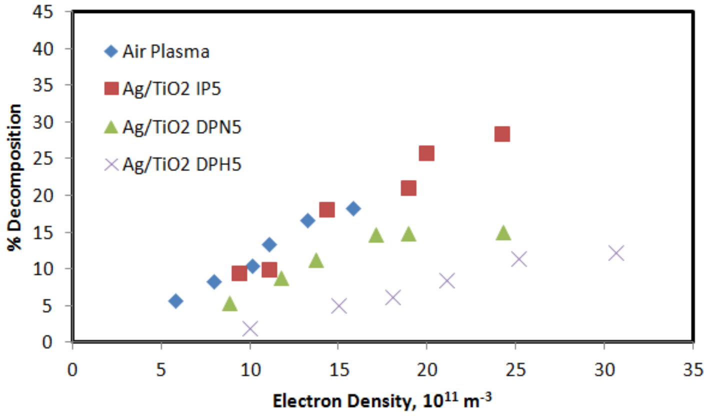

Figure 6.8. Effect of Ag/TiO$_2$ catalysts on electron density to benzene decomposition

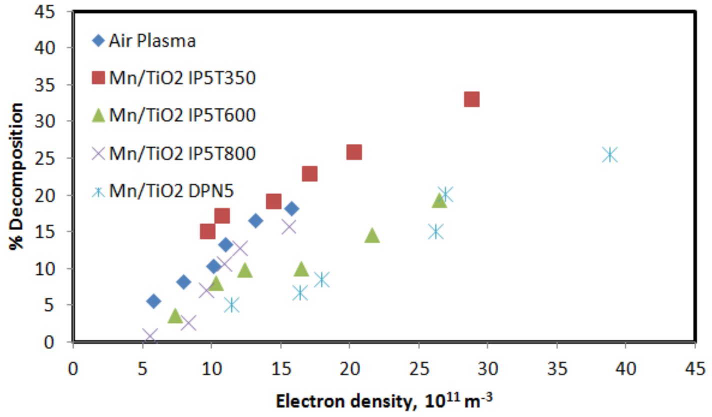

Figure 6.9. Effect of Mn/TiO$_2$ catalysts on electron density to benzene decomposition

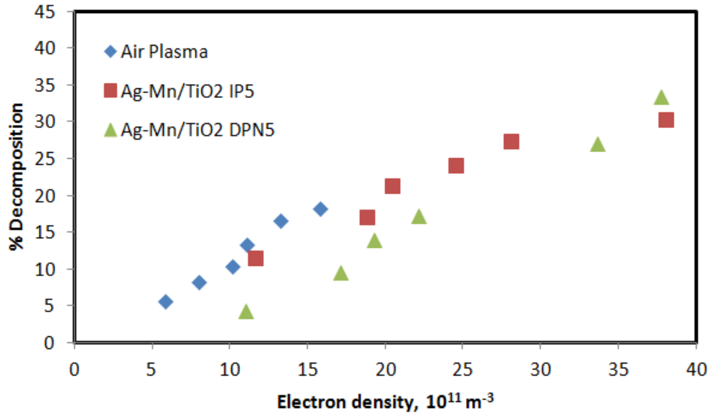

Figure 6.10. Effect of Ag-Mn/TiO$_2$ catalysts on electron density to benzene decomposition

6.4 Effect of catalysts on ozone and nitrogen oxide concentration during PDC treatment

Effluent concentrations for ozone and nitrogen oxide during PDC treatment of benzene were also analyzed and results are presented in Fig. 6.11 for Ag/TiO_2, Fig. 6.12 for Mn/TiO_2, and Fig 6.13 for Ag-Mn/TiO_2. Ozone and nitrogen oxide concentration increase linearly with SIE but showed lower values compared to those that were observed in Chapter 5. This indicates that the ozone and nitrogen oxides that were formed by the discharge were utilized in the decomposition of benzene. Results also showed that similar values for ozone and nitrogen oxides were obtained. This indicated that the composition of nitrogen oxides were controlled by ozone concentration.

For Ag/TiO_2 catalysts (Fig. 6.11), similar trend were observed for all Ag/TiO_2 catalysts except for IP5 where it showed slightly higher concentrations. For Mn/TiO_2 catalysts (Fig. 6.12), similar trend and similar values were also observed regardless of the preparation method except for IP5T800 where there were still high concentrations for ozone and nitrogen oxides in the effluent. Among all the tested catalysts, Mn/TiO_2 catalysts showed the highest reduction in ozone and nitrogen oxides in the effluent. And lastly for the Ag-Mn/TiO_2 (Fig. 6.13), similar values for IP5 and DPN5 were observed with those by DPN5 catalysts having slightly higher values than that of IP5 catalysts.

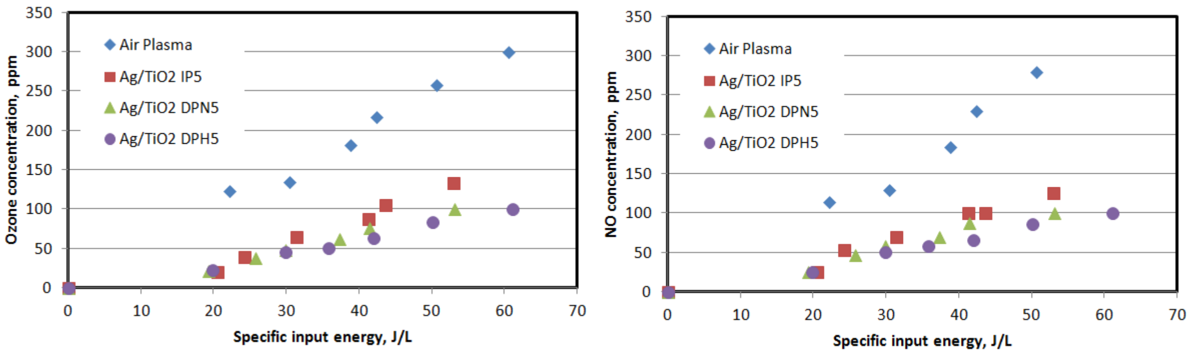

Figure 6.11. Effect of Ag/TiO_2 catalysts on O_3 and NO concentrations during PDC treatment

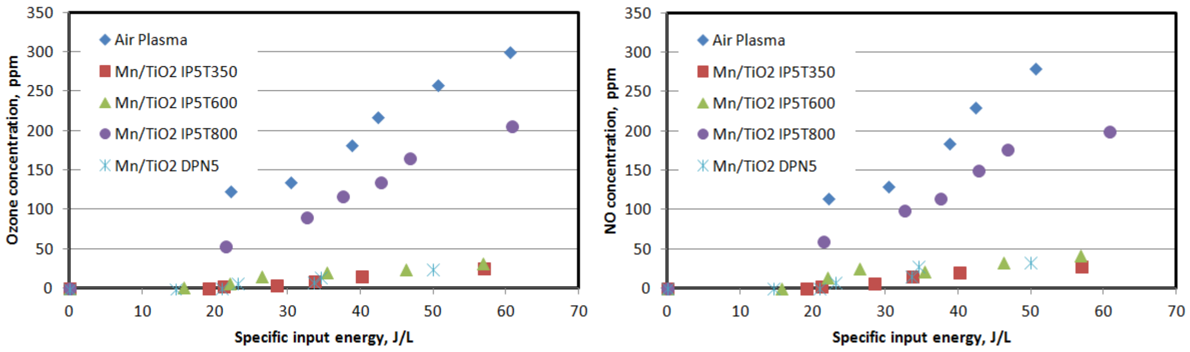

Figure 6.12. Effect of Mn/TiO_2 catalysts on O_3 and NO concentrations during PDC treatment

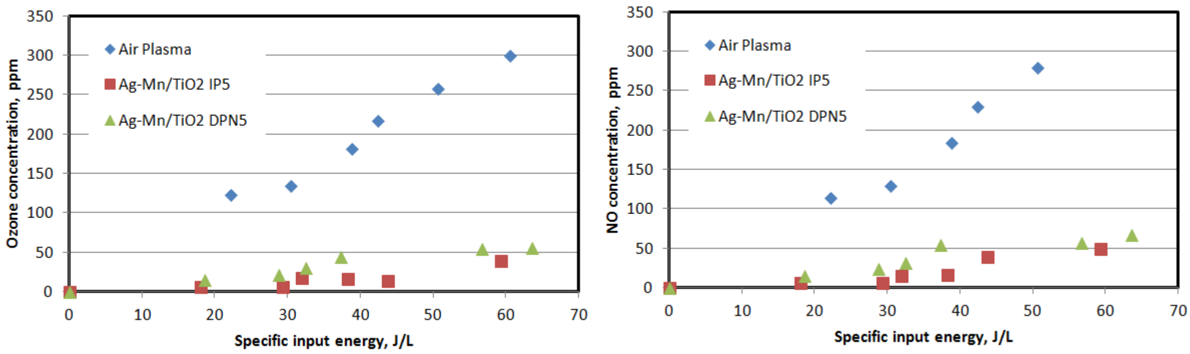

Figure 6.13. Effect of Ag-Mn/TiO$_2$ catalysts on O$_3$ and NO concentrations during PDC treatment

Ozone and nitrogen oxide generation efficiency ratios were also calculated to easily compare the effect of catalysts on ozone and nitrogen oxide concentrations during the PDC treatment of benzene and results are presented in Fig. 6.14. Results showed that by including benzene in the gas stream, ozone and nitrogen oxide generation decreased. This could be brought about by the competitive reaction of benzene, oxygen and nitrogen with the energized electrons from the discharge or it could also indicate that the generated ozone and nitrogen oxide took part in the decomposition of benzene.

Upon addition of the catalysts within the reactor, further reductions in generation efficiency were observed. Again, reductions in ozone and nitrogen oxide generation could be explained by the decrease in discharge volume due to the presence of the catalyst, the self-decomposition of ozone and nitrogen oxide on the catalyst surface, and additionally, their utilization in benzene decomposition. Since the values presented in Fig 6.14 are lower than those observed from Figs. 5.3, 5.7, and 5.9, then it can be said that there was a synergetic effect between the plasma generated species (e.g. ozone and nitrogen oxide) and the catalyst for the decomposition of benzene.

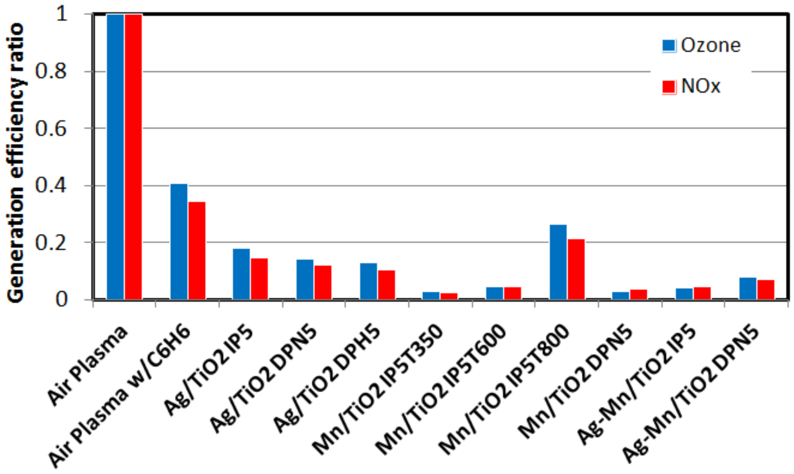

Figure 6.14. Effect of catalysts on O$_3$ and NOx generation efficiency ratio during the non-thermal plasma driven catalysis decomposition of benzene

The active species generated non-thermal plasma which includes ozone promote the decomposition of benzene on the catalyst surface. Active species from the catalytic decomposition of ozone are also considered to be mainly responsible for the promotion effects which include species such as $O(^1D)$, $O(^3P)$, O_2^-, and O_2^{2-} and have shown to have higher activity towards oxidation of hydrocarbons than ozone. The ozone and nitrogen oxide final concentration obtained with the different catalysts were plotted against benzene decomposition in Fig. 6.15. Results show that when the ozone and nitrogen oxide concentrations were low in the effluent stream, higher decomposition efficiencies were obtained. This confirms that when the ozone generated by the non-thermal plasma is decomposed on the catalyst surface - resulting in lower effluent ozone concentrations - the decomposed species on the catalyst surface promote the decomposition of benzene.

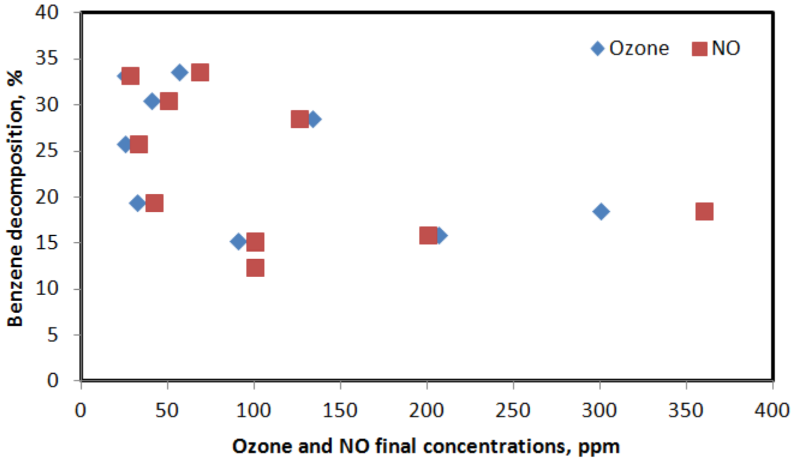

Figure 6.15. Relationship of ozone and nitrogen oxide final concentration to benzene decomposition using Ag/TiO_2, Mn/TiO_2 and Ag-Mn/TiO_2 catalysts

6.5 Decomposition mechanism

The general mechanism for plasma driven catalysis decomposition of volatile organic compounds was presented in Chapter 2 which follows Languir-Hinshelwood type reactions and Eley-Rideal type reactions. In the Langmuir-Hinshelwood model, both reactants need to be adsorbed on the catalyst surface, followed by migration to the active site to induce chemical reactions. In the Eley-Rideal model, only one reactant is adsorbed on the surface and the other exists in the gas phase.

Based from the results that were presented, benzene can be decomposed by the active species generated by the plasma discharge in the gas-phase. Also, addition of metals on TiO_2 catalysts within the discharge region promoted further the decomposition of benzene. This indicates that the direct interaction of the generated active species by the discharge in the gas-phase, as well as the adsorbed active species on the catalyst surface promoted benzene decomposition.

Benzene decomposition by non-thermal plasma discharge was caused by the energetic electrons in plasma that initiated multiple impact-triggered dissociation reactions. Direct electron impact reaction with benzene could produce an unstable benzene radical which could lead to the benzene ring opening producing intermediate by-products. Collisions between the energetic electrons between oxygen and nitrogen molecules produced ozone and nitrogen oxides which were also utilized in oxidation reactions that could possibly form aliphatic carbonyl intermediates that would eventually be oxidized to carbon dioxide. The reaction mechanism upon addition of catalysts within the discharge region is more complicated as there would be even more reactions involved. The influence of the plasma discharge on catalytic processes as well as the influence of the catalysts on discharge properties needs to be considered.

Unfortunately, the exact mechanism for benzene decomposition could not be examined without specialized *in situ* instruments to monitor the actual composition of the gases within the discharge region. Also, the interaction between ozone and nitrogen oxides within the discharge region is rather complicated as it involves multiple reaction pathways to produce not only NO but also NO_2, NO_3, and N_2O_5. And in these reactions, ozone is used up and are competing reactions to benzene decomposition.

In this study, benzene decomposition mechanism depended on the type of metal loaded on TiO_2 and preparation method used. Varying degrees of benzene decomposition, ozone and nitrogen oxide concentrations, and carbon dioxide yield were observed. When the metal loaded on TiO_2 was silver/oxides, this seemed to enhance pollutant mineralization and showed higher values for carbon dioxide yield. When the metal loaded on TiO_2 was manganese oxides, benzene decomposition as well as reducing the concentrations of ozone and nitrogen oxides in the effluent were promoted. Using both silver and manganese on TiO_2 showed a combination of these results as the catalyst showed the highest benzene decomposition and carbon dioxide yield. It seems that benzene decomposition is controlled by ozone and nitrogen oxide decomposition on the catalyst surface as the active species that were generated by self-decomposition reactions enhanced benzene decomposition.

6.6 Summary of results

This chapter discusses the results obtained from the plasma driven catalytic decomposition of benzene using 5% loaded metal catalysts: Ag/TiO_2, Mn/TiO_2, and $Ag\text{-}Mn/TiO_2$ prepared by impregnation method and deposition-precipitation methods. Treatment of benzene by air plasma alone was also performed.

Results showed that benzene could be decomposed by air plasma alone to a certain degree but obtained poor mineralization to carbon dioxide as seen from the carbon balance and carbon dioxide yield. This indicated that even though benzene was decomposed by the generated plasma species, it was not fully mineralized into carbon dioxide and formed by-products that were not detected by GC-MS and GC-TCD analysis. This may pose a problem since decomposition by-products may still be toxic.

During the treatment with catalysts, majority of the catalysts showed improvement in decomposition of benzene. Also, depending on the catalyst used, improvements on ozone and nitrogen oxide decomposition, carbon balance and carbon dioxide yield was observed. An increase in electron density was observed when catalysts were placed within the discharge region However, an increase in electron density did not necessarily improve benzene decomposition efficiency. Benzene decomposition still depended on the characteristics of the catalysts used and not solely on the electron density which indicated that it is not just the electron density that is important but how the electrons were utilized in the decomposition of the pollutant.

Manganese based catalysts showed improvement in utilizing ozone and nitrogen oxide in the decomposition of benzene and showed significant reduction in their concentrations in the effluent. Silver based catalysts showed an improvement in carbon balance and carbon dioxide yield. And using both silver and manganese combined these effects with the Ag-Mn/TiO_2 DPN5 catalyst showed the best performance in all of the tested catalysts in terms of benzene decomposition at 33.55%, carbon balance at 99.28% and carbon dioxide yield at 97.85%.

Chapter 7

CONCLUSIONS AND RECOMMENDATIONS

7.1 Thesis overview

This thesis investigates the use of non-thermal plasma catalysis technology as an alternative method for volatile organic compound decomposition. As this technology is relatively new compared to other established technologies, much is still uncertain about this technology, particularly the reported synergistic effects between non-thermal plasma and catalysis. The mechanisms are rather complex due to the combined interaction of plasma together with heterogeneous catalysis. High input energy systems has shown to be capable in decomposing VOCs at wide range of concentrations and at varying degrees of mineralization. However, a problem present in this system is the formation of secondary pollutants primarily in the form of ozone and nitrogen oxides. Ozone can be easily decomposed thermally and have relatively short half-lives but nitrogen oxides are stable at low temperatures. Thus, aside from looking into the capability of the system to decompose VOCs, special attention must also be placed on effluent composition and concentrations.

For the purpose of this study, this study focused on the use of differently prepared silver and manganese oxides on titanium dioxide and testing its catalytic activity on the decomposition of benzene in a non-thermal plasma driven catalysis system. Each individual chapter of this work focused on addressing the specific objectives outlined in Chapter 1. Conclusions and research findings for each individual chapter are summarized below.

7.2 Catalyst preparation and characterization

In Chapter 3, the catalyst preparation methods and characterization results were discussed. Three types of catalysts: Ag/TiO_2, Mn/TiO_2, and Ag-Mn/TiO_2 and were prepared by impregnation method (IP) and by deposition-precipitation methods with sodium hydroxide (DPN) or hydrogen peroxide (DPH). The prepared catalysts were then characterized to determine their structural and chemical properties. Characterizations were performed using TG-DTA, XRD, N_2 adsorption BET method, XPS and SEM-EDS.

Results showed that catalyst structural and chemical properties highly depended on their preparation method and varying specific surface area, metal oxidation states, metal distribution and metal surface concentrations were obtained. The catalyst specific surface area decreased with increasing calcination temperature and metal loading. Catalysts prepared by deposition-precipitation methods showed better metal dispersion and higher metal surface concentrations on the TiO_2 surface compared to catalysts prepared by impregnation method. The catalyst specific surface area and bulk chemical species were summarized from Chapter 3 and presented in a table taken from Chapter 5.

Table 5. 2. Summary of specific surface area and bulk chemical species of the prepared catalysts

TiO_2	SSA, m^2/g		64.95			
			IP	DPN	DPH	
Ag/TiO_2	SSA, m^2/g	1%	61.64	64.73	65.54	
		3%	53.54	64.60	65.14	
		5%	49.00	63.28	64.94	
	Bulk metal		Ag/TiO_2	Ag_2O/TiO_2	AgO/TiO_2	
	Metal fraction		1.0	0.78	0.76	
			IP T350	IP T600	IP T800	DPN
Mn/TiO_2	SSA, m^2/g	1%	76.49	71.97	51.64	74.86
		3%	76.91	66.12	1.54	74.45
		5%	72.36	61.57	2.04	72.95
	Bulk metal		MnO_2/TiO_2	Mn_2O_3/TiO_2	$MnTiO_3$	Mn_3O_4/TiO_2
	Metal fraction		0.58	0.76	0.49	0.68
			IP	DPN		
$Ag\text{-}Mn/TiO_2$	SSA, m^2/g	1%	73.30	74.62		
		3%	73.80	70.23		
		5%	72.35	67.45		
	Bulk metal		$Ag\text{-}MnO_2/TiO_2$	$Ag_2O\text{-}MnO_2/TiO_2$		
	Metal fraction		1.0/0.37[a]	0.92/0.51[a]		

[a]first fraction is for Ag followed by Mn fraction

7.3 Characterization of dielectric barrier discharge reactor

In Chapter 4, characterization of the dielectric barrier discharge reactor was performed to observe the influence of reactor parameters to ozone and nitrogen oxides formation. Changes were made to the reactor length, TiO_2 loading, and reactor configuration. Results showed that there was a linear relationship between specific input energy and ozone and nitrogen oxide concentration regardless of the changes made to the reactor at the tested applied voltages. With increasing reactor length, higher concentrations of ozone and nitrogen oxide were produced and discharge power also increase due to the increase in the discharge volume of the reactor. By adding TiO_2 catalysts within the discharge region, this effectively reduced the discharge volume and consequently reduced the amount of ozone and nitrogen oxides formed as well as the discharge power from the reactor. The effect of reactor configuration was tested by placing the TiO_2 catalysts within the discharge region (plasma driven catalysis, PDC) or just directly outside of the discharge region (plasma assisted catalysis, PAC). Lower ozone and nitrogen oxide concentrations were observed for the PDC system compared to the PAC system. PAC system showed higher discharge power compared to plasma alone system which was attributed to the non-uniform discharge generated as the catalysts were located just outside the edge of the discharge region. The effect of reactor parameters on electron density and electron temperature were also calculated from the V-Q diagrams. Regardless of reactor configuration, electron density increased with applied voltage, increasing reactor length, and TiO_2 loading. Electron temperature increased with reactor length but decreased with increasing TiO_2 loading.

7.4 Effect of catalyst on non-thermal plasma discharge

In Chapter 5, the prepared catalysts presented in Chapter 3 were tested to examine their effect on ozone and nitrogen oxide concentrations that were generated from the DBD reactor. Based on limiting ozone and nitrogen oxide concentrations, catalytic activity is as follows:

Ag/TiO_2: DPN > IP > DPH

Mn/TiO_2: IPT350 > IPT600 > DPN > IPT800

Ag-Mn/TiO_2: IP > DPN

The reductions in ozone and nitrogen oxide concentrations found were attributed to the reduced discharge volume due to the presence of the catalysts which limited the amount of energetic electrons available for electron-impact reactions to form ozone and nitrogen oxide and the self-decomposition reactions on the catalyst surface. Addition of TiO_2 within the DBD reactor reduced the amount of ozone and nitrogen oxide which was further reduced when metal was placed on TiO_2 which indicated that the metal promoted self-decomposition reactions on the catalyst surface. The degree to which the catalysts reduced ozone and nitrogen oxide concentrations were found to be dependent on metal loading and oxidation state rather than the catalyst specific surface area. Catalysts with multiple and higher metal oxidations states showed better performance in limiting ozone and nitrogen oxide concentrations. Higher metal oxidation states are good for ozone adsorption which lead to the generation of active oxygen species which is also favorable for ozone decomposition. Multiple oxidations states found on the catalyst would also allow for multiple reduction-oxidation reactions simultaneously for ozone decomposition.

7.5 Decomposition of benzene using plasma driven catalysis

In Chapter 6, the 5% loaded metal catalysts were tested on the non-thermal plasma catalytic decomposition of benzene. Air plasma was also tested and showed 18.39% decomposition of benzene with a carbon balance of 82.78% and a carbon dioxide yield of 6.35%. This indicated that air plasma by itself can decompose benzene to a certain degree but showed incomplete mineralization to carbon dioxide. This means that there were intermediates and by-products formed during the process and were not able to be detected by GC-MS and GC-TCD.

Addition of catalysts improved not only benzene decomposition but also showed higher values for carbon balance and carbon dioxide yield. Also, ozone and nitrogen oxide concentrations were significantly reduced. An increase in electron density was observed but did not necessarily improve benzene decomposition. From the catalysts that were used, silver loaded TiO_2 showed an improvement in carbon balance and carbon dioxide yield while manganese loaded TiO_2 showed an improvement in benzene decomposition and reducing concentrations for ozone and nitrogen oxide. Using both silver and manganese on TiO_2 showed a combination of these effects with Ag-Mn/TiO_2 prepared by DPN method showing the highest benzene decomposition efficiency at 33.55%, carbon balance at 99.28% and carbon dioxide yield of 97.85%.

Ozone and nitrogen oxide generation efficiencies were also lower compared than those presented in Chapter 5. This indicated a synergetic effect between the plasma generated species (e.g. ozone and nitrogen oxide) and the catalysts in decomposing benzene.

7.6 Future works

For air plasma alone treatment, incomplete oxidation of benzene and poor carbon balance was observed which indicated the formation of intermediates and unwanted by-products. Unfortunately, these species were not detected during analysis. Knowledge of what these intermediate compounds are can be useful in the selection of an appropriate catalyst for use in plasma catalytic systems.

For the plasma driven catalytic decomposition of benzene, the extent of benzene decomposition was limited by the input energy supplied to the reactor. The trend indicated that by increasing input energy, higher decomposition efficiencies could be obtained. This could be achieved by changing the voltage source or the working frequency of the applied voltage. However, with increase in input energy, effluent concentrations of ozone and nitrogen oxides are also expected to increase. To deal with this problem, manipulating reactor configurations such as using a two-stage reactor could be utilized to treat the remaining ozone and nitrogen oxides in the effluent.

In the field of non-thermal plasma catalysis, varying mechanisms and enhancement effects have been described and proposed in literature but often showed discrepancies depending on each individual system used. Therefore, better understanding of which mechanisms have the most important contribution and which chemical species play a more dominant role in VOC decomposition is still uncertain. Development of well-designed instruments specialized in *in situ* measurements is needed.

Acknowledgments

The author would like to express his sincerest gratitude and deepest thanks to those whose valuable contributions and assistance have helped the realization of this research:

To my adviser, Prof. Hirofumi Hinode, and assistant professor Dr. Winarto Kurniawan, for their continuous support for my research. I will forever be thankful for all the knowledge, motivation, guidance and patience you have given me.

The members of the doctoral examination committee, Prof. Kiyohiko Nakasaki (Dept. of International Development Engineering), Prof. Takayuki Komatsu (Dept. of Chemistry and Materials Science), Prof. Hidetoshi Sekiguchi and Prof. Shinsuke Mori (Dept. of Chemical Engineering), for the time and efforts, their questions and comments which helped improve this thesis.

To the current and past members of Hinode Laboratory, for their warm reception and for all their valuable insights and contributions which helped me during my research, particularly through the discussions throughout the laboratory seminars.

To the Filipino community of Tokyo Institute of Technology, whose support has helped me overcome any problems I have encountered and has kept me sane. I greatly value their friendship and appreciate all the things that they have done for me.

I would like to thank my family for the support they have provided me in my decisions, and endeavors, and for always being there for me.

Lastly, I would like to acknowledge the financial support given by the Japanese Ministry of Education, Culture, Sports, Science and Technology (MEXT) for offering the scholarship without which, I would not be able to pursue my studies.